Ultrafast Laser-induced Magnetisation Dynamics: Gilbert damping of Metal and Half-metal

Xianyang Lu

Doctor of Philosophy

University of York

Physics

April 2018

Abstract

In this thesis, the magnetic damping in different metals and half-metals is studied using an all-optical pump-probe method: the time-resolved magneto-optic Kerr effect (TRMOKE), combined with several advanced characterisation techniques, such as angle-resolved photoemission spectroscopy (APRES) and X-ray magnetic circular dichroism (XMCD).

In Fe/Cr/GaAs heterostructures, the uniaxial magnetic anisotropy (UMA) and the magnetic damping have been studied as a function of the thickness of Cr interlayer. The UMA is attributed to the Fe-GaAs chemical bonding at the interface via increasing the orbit moments of Fe atoms. The Cr interlayer with increasing thickness blocks the Fe-GaAs bonding and the UMA gradually. The magnetic damping shows a dramatic drop when Cr interlayer is deposited, even with only 0.5 ML. The results have indicated that the UMA and the damping originate from different mechanisms although the Fe/GaAs interface plays an important role in both phenomena.

The correlation between magnetic damping and the electronic structures have been investigated in Co_2FeAl Heusler alloy. By varying the growth temperature, both the magnetic damping and the electronic structure have been found affected significantly. It is experimentally demonstrated that the low damping constant originates from a low density of state (DOS) at Fermi level. A "shoulder-like" peak in the vicinity of Fermi level in the energy distribution curve would enhance the DOS and the damping.

A pair of half-met allic Fe_3O_4 films, with and without structural defects, have been compared in order to investigate the effect of defects in magnetic damping. The enhancement of the intrinsic damping $\alpha_0 = 0.063 \pm 0.010$ in defect-free Fe_3O_4 sample is attributed to the emergence of the perpendicular standing spin wave (PSSW), while the magnetic damping in the as-grown sample $\alpha_0 = 0.039 \pm 0.004$ is lower because the defects would scatter the spin wave or magnon and the energy transfer channel from the uniform precession to the PSSW does not exist.

Content List

List of Figures

List of Tables

Acknowledgements

Firstly, I would like to express my sincere gratitude to my supervisors Dr. Jing Wu in Department of Physics and Prof. Yongbing Xu in Department of Electronics. With a sharp mind, Prof. Yongbing Xu always offers me a valuable direction in my research. The door to Dr. Jing Wu office was always open whenever I ran into a trouble spot or had a question about my research or writing. Without their helpful guidance and continuous support, I could not have finish my PhD research.

I would like to thank my TAP and thesis supervisors Prof. Roy Chantrell and Prof. Nigel Woolsey for their helpful advises. I would also thank Dr. Vlado Lazarov and Dr. Balati Kuerbanjiang for supplying the samples and the remarkable TEM images; Dr. Richard Evans and Dr. Lewis Atkinson for useful discussion and supportive simulations.

I also thank Mr. Dave Coultard, Mr. Neil Johnson, Dr. Andrew Vick, Mr. Adam Stroughair, Dr. Iain Will, Mr. Jonathan Creamer and Mr. Charan Panesar for providing professional technical support. Special thanks go to Mr. John Emery for his patience dedicated to maintaining our laser system.

I would like to thank my colleagues and we have shared a wonderful experience and time here. Your names are: Mr. Guanqi Li, Mr. Hua Lin, Dr. Cong Lu, Dr. James Sizeland, Mr. Junlin Wang, Mr. Yichuan Wang, Mr. Lingyu Yan, Mr. Yu Yan, Mr. Kunpeng Zhang, Dr. Shuo Zhao and Mr. Xiangyu Zheng.

I am grateful to the Department of Physics for funding my study at University of York.

Last but not least I would like to thank my parents for their unwavering support and encouragement throughout my PhD study here and my life.

Declaration

I declare that this thesis titled, “Ultrafast laser-induced magnetisation dynamics: Gilbert damping of metal and half-metal”, and the work presented in it are my own. I confirm that:

This work was done wholly or mainly while in candidature for a research degree at University of York and has not been submitted previously for a degree at this or any other university. All sources are acknowledged as references. I am solely responsible for all the research work described in this thesis except for the following collaborations:

In chapter 4, the Fe/Cr/GaAs(100) samples were prepared by Yu Yan and myself. The XMCD measurements were done by Yu Yan.

In chapter 5, the Co_2FeAl samples were prepared by Xiaoqian Zhang and myself. The ARPES measurements were conducted by Xiaoqian Zhang, Huanfeng Xu and myself.

In chapter 6, the Fe_3O_4 samples were supplied by Vlado Lazarov. The TEM images were obtained and analyzed by Balati Kuerbanjiang. After discussion with myself, the numerical simulations were performed by Lewis Atkinsons.

Xianyang Lu

Mach 2018 in York

Publication List

1. **Xianyang Lu**, Lewis J. Atkinson, Balati Kuerbanjiang, Bo Liu, Guanqi Li, *et al.*, "Evidence of coupling between magnon excitation and the Gilbert damping in half-metallic oxides", *submitted to Advanced Functional Materials* (Under review)
2. Xiaoqian Zhang, Huanfeng Xu, Bolin Lai, Qiangsheng Lu, **Xianyang Lu**, Yequan Chen, *et al.*, "Direct observation of high spin polarization in Co2FeAl thin films", *submitted to Scientific Reports* (Accepted)
3. Jing Wu, Tuyuan Cheng, Cong Lu, Xiao Zou, **Xianyang Lu**, Chris Bunce, "Spin-dynamics measurement techniques", *Handbook of Spintronics*, 1-37, Springer Nertherlands (2014)

Chapter 1 Introduction

The history of magnetism can be traced back for thousands of years, with its power being utilised ever since the first natural lodestones such as magnetic magnetite were discovered. One of the earliest great inventions utilising this power was the compass, first invented as a device for navigation as early as the 11th century in China [1]. However, although the compass greatly helped people to explore the world, the application of magnetism seemed to be limited to prior to the 19th century. However, once a modern understanding of magnetic phenomena in condensed matter was successfully developed by Pierre Curie and Pierre Weiss around 1900, studies in magnetism became systematic and its applications became ubiquitous [2]. The present day understanding of magnetism is based on the theory of the motion and interactions of electrons in atoms known as quantum electrodynamics, and this stems from the work and theoretical models of Ernst Ising and Werner Heisenberg [3].

In 1988, Peter Grünberg and Albert Fert independently found the resistance of a multilayer structure to show great dependence on an applied field; this is known as the giant-magnetoresistive (GMR) effect [4]. The required sandwich structure consists of two ferromagnetic (FM) layers that are separated by a thin non-magnetic layer (NM); the magnetoresistance ratio can easily reach ~80% for such a Fe/Cr/Fe multilayer [5, 6]. Grünberg and Fert were awarded the 2007 Nobel Prize in physics jointly, and the discovery of GMR triggered revolutionary development in a new field in magnetism, known as spintronics.

Spintronics, a portmanteau of spin electronics, aims to exploit spin properties instead of, or in addition, to the charge degrees of freedom utilised in solid state physics, and related devices. The most successful application of spintronics is the hard disk drive (HDD), which is based on a GMR read head. By fixing the magnetic orientation in the bottom FM layer with a large coercive field, the magnetoresistance or current flowing through the sandwich can be tuned by the magnetic orientation in the top soft free FM layer by means of a small magnetic field. In these cases, applying only a small magnetic

field means that the spin-polarised current can be turned on or off; thus this structure is named a spin valve. The first use of spin valve sensors in hard disk drive read heads was by IBM in 1997, who offered devices with $16.8\,\mathrm{GB}$ of storage; the recording density was then improved by 100% annually for four years until 2001 [7]. The next key technique in the development of the HDD was perpendicular magnetic recording (PMR) media, which was introduced in 2005, and which boosted the capacity of a single 1.8-inch hard disk platter to 320 gigabits. In 2012, the areal density (AD) reached 620 gigabits per square inch for a 3.5-inch hard drive of three terabytes. Alongside recording density, the reading and writing speed of HDDs is also an important parameter that will be eventually limited by the switching characteristics of the magnetic layers, especially as transfer rates begin to approach the GHs-range. As magnetic precession begins to dominate the switching process, an intimate knowledge of spin dynamics is needed for further improvements.

Another spintronic device is magnetoresistive random-access memory (MRAM) which is a strong candidate for next generation memory. MRAM has exhibited significant advantages as a fast, fairly low-power, high-endurance, radiation-resistant non-volatile memory form that can be integrated with the complementary metal-oxide-semiconductor (CMOS) as a back-end of line (BEOL) process [8]. The read-out process of MRAM bits is reliably performed via a tunnelling magnetoresistance (TMR) effect [9, 10] in magnetic tunnel junctions (MTJs). Similar to GMR devices, MTJs also have a sandwich structure, but the free layer and pinned layer are separated by an insulator such as MgO that acts as a tunnelling barrier, rather than by a non-magnetic metal as in GMR. The value of the TMR effect has been reported to be as anywhere between 138% to 604% [11-14] in CoFeB/MgO/CoFeB pseudo-spin-valve MTJs, which is much larger than the GMR effect. This is why the latest HDD read heads have replaced GMR devices with TMR devices to increase storage performance. In terms of the writing process in MRAM, the latest technology used to switch the magnetisation of the free layer is to use spin-polarised currents via a spin transfer torque (STT) effect [15, 16]. The key parameter in the writing process is thus the threshold current density, J_c, used for switching, which is proportional to the magnetic damping, α [17]. As the

TMR ratio is related to the spin polarisation of the two ferromagnetic layers [18, 19], the simplest way to achieve large TMR ratios relies on the use of so-called "half-metals" that, theoretically, have almost total intrinsic spin polarisation; these include CrO_2, Fe_3O_4, mixed-valence manganite, and some Heusler alloys. Thus, as in the current study, studying the magnetisation dynamics in such half-metals, especially magnetic damping, is important in terms of gaining further understanding and designing better MRAM devices.

In the overall framework of using contemporary spintronics to either seek faster and more capacious magnetic storage or to exploit next-generation high-performance MRAM, detailed investigations of magnetisation dynamics are of great importance. In 1996, the exciting discovery of laser-induced ultrafast demagnetisation in Ni thin film was very timely [20], and combined with a greater availability of femtosecond laser sources at the end of the 20th century, this discovery led to a new field of research: laser-induced magnetisation dynamics. The rest of this chapter will present the basic framework of this field from three aspects: ultrafast demagnetisation, laser-induced magnetisation precession, and all-optical magnetisation switching. This will help to demonstrate the remarkable scientific achievements achieved during the exploration of laser-induced magnetisation dynamics, which have accelerated the development of both older magnetisation and new spintronic devices.

1.1 Ultrafast demagnetisation

Prior to 1996, time-resolved studies of magnetisation dynamics using picosecond laser pulses were not successful because the available laser pulses were of the same duration, or even longer than, the relevant time scales [21, 22]. With such long excitations, the systems, whether spin, lattice, or electron, were always in equilibrium states, and the intrinsic time scales could not be accessed as the systems followed their excitation profiles.

In 1996, Beaurepaire *et al.* successfully measured the transient transmissivity and

the longitudinal MOKE of an Ni thin film [20]. As shown in Fig. 1.1, from the time dependence of hysteresis loops, they deduced that the remanent magnetisation undergoes a rapid decrease within 2 ps after laser pulse excitation. In contrast, the electron thermalisation time was about 260 fs, estimated based on transient reflectivity. However, in pump-probe experiments in Fe thin films [23] carried out by Carpene *et al.* in 2008, the reflectivity response was observed to suffer about a 150 fs delay after the magnetisation response. This even faster demagnetisation, taking place on a time scale < 100 fs, was attributed to the electron-magnon interaction with a time constant of 50 to 75 fs. Ignoring the delay between electron excitation and the quench of magnetisation, the observed dynamic was much faster than the spin-lattice relaxation time, which is generally of a 10 to 100 ps time scales [24]. This femtosecond demagnetisation was also demonstrated using two-photon photoemission [25] and XMCD [26].

The fundamental question for such all-optical pump-probe experiments is what TRMOKE really probes; is it a simple optical excitation or a genuine magnetic excitation? By studying Cu/Ni/Cu wedges [27], Koopmans *et al.* concluded, based on the difference between the Kerr ellipticity and rotation, that the loss of magneto-optical contrast cannot be directly related to an instantaneous demagnetisation; however, other groups reported no or little difference between ellipticity and rotation [28-30]. Nevertheless, a significant demagnetisation was demonstrated at the sub-100 fs time scale in $CoPt_3$ using laser pulses with as short as 20 fs pulse width. This suggests that the existing demagnetisation at ~ 1 ps is not a genuine magnetic response [28]. The theoretical study by Oppeneer and Liebsch also supported a breakdown between magneto-optical response and magnetisation in ultrafast pump-probe experiments [31]. It was shown than the conductivity tensor, and therefore the complex Kerr rotation, could be substantially modified with dichroic bleaching and state-blocking effects such that the Kerr rotation and ellipticity were no longer proportional to the magnetisation. The long-standing dispute was finally resolved theoretically by Zhang *et al.* in 2009 [32]. By construction of a phase-sensitive polarisation versus magnetisation plot through a first-principles investigation of ferromagnetic nickel, a new paradigm for the

magneto-Kerr effect was proposed: the optical response reflects the magnetic signal where the laser pulse is longer than the charge dephasing time.

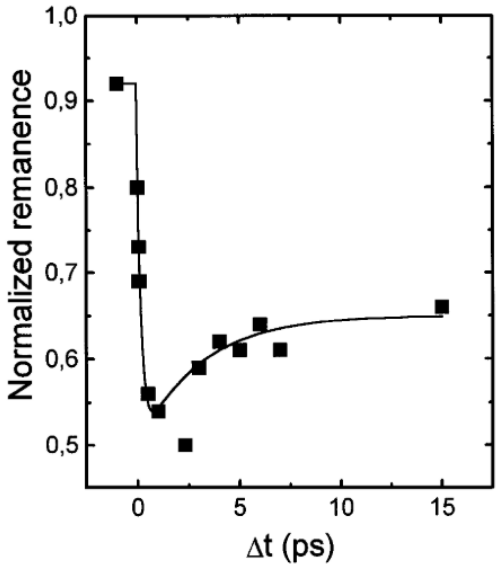

Figure 1.1: Transient remanent longitudinal MOKE signal of a Ni(20 nm)/MgF_2(100 nm) film for $7\ \mathrm{mJ/cm^2}$ pump fluence [20].

Laser-induced ultrafast demagnetisation can be qualitatively described by a phenomenological three-temperature (3TM) model that contains three separate but interacting reservoirs: electrons, lattice, and spins. As shown in Fig. 1.2(a), these three subsystems are connected by interactions of different origins and efficiency. As the electrons are excited by a laser pulse to a high temperature, T_e, the temperatures of the spin, T_s, and lattice, T_l, systems will subsequently be raised via electron-lattice (phonon) and electron-magnon (spin) interactions, respectively. In the meantime, the spin-lattice interaction, usually considered to be of the same order of magnitude as the magnetocrystalline anisotropy, also plays a role, which corresponds to a longer relaxation time, such as the $300\ \mathrm{ps}$ to $400\ \mathrm{ps}$ seen in Ni [25, 33]. As the electron's heat capacity is only one or two orders of magnitude smaller than that of the lattice, the electron temperature may become quite high with in the first tens of fs after laser pulse excitation, while the lattice temperature remains relatively low [34], as shown in Fig. 1.2(b). Here, the spin temperature, T_s, is defined by the equilibrium $M(T)$; thus, $M(T_\mathrm{s}(\Delta t))$ refers to the transient magnetisation at delay time Δt.

In general, ultrafast laser-induced demagnetisation is a very complicated process involving various components with several different underling physics effects. The exact physics of demagnetisation in ferromagnetic metals is still the subject of debate, as are many of the properties of other magnetic materials such as magnetic semiconductors [35], magnetic dielectrics [36], and magnetic half metals [37].

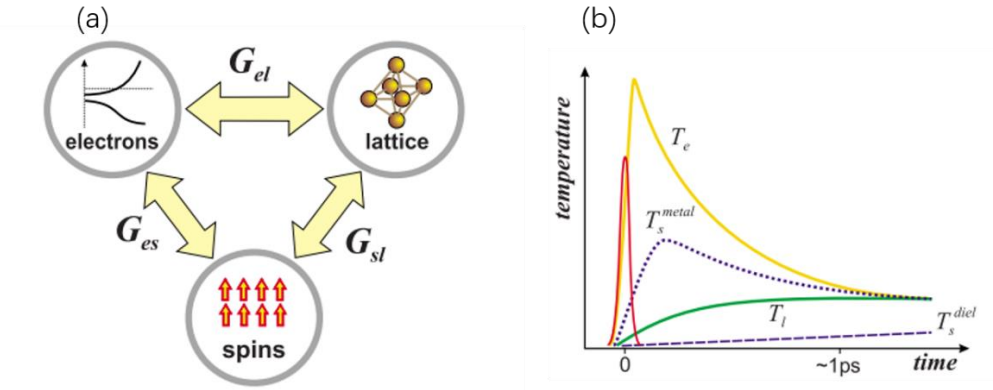

Figure 1.2: (a) a schematic description of the interacting reservoirs (electrons, spins, and lattice) in the three-temperature model. G_{ij} represents the coupling between the ith and jth baths. (b) temperal behavior of the temperature of the three subsystems following excitation with a short laser pulse. Eventually, the electron, lattice, and spin temperatures will equalise by distributing the additional energy via interactions between themselves [38].

1.2 Laser-induced magnetisation precession

Alongside ultrafast demagnetisation, the other important sub-field of spin dynamics is laser-induced magnetisation precession. Before we introduce the all-optical laser-induced magnetisation precession, other pioneering works on the time domain magnetisation measurements should be reviewed. A very early observation of damped magnetisation precession measured in the time domain were first reported in 1961 [39] shown in Fig. 1.3(a). The magnetic sample was excited by a pulsed magnetic field through a strip-line and the precession was monitored inductively using a pick-up loop. Based on this method, the pulsed inductive microwave magnetometry (PIMM) method are developed in 1999 [40] and the experimental scheme is sketched in Fig. 1.3(b). the magnetic samples are placed onto a coplanar waveguide, which generates a pulsed magnetic field to stimulate the precession. The induced voltage response is detected by

the same waveguide and the signals are measured using a high bandwidth oscilloscope. The sample and the waveguide are placed in a Helmholtz coils to provide magnetic field [41-44].

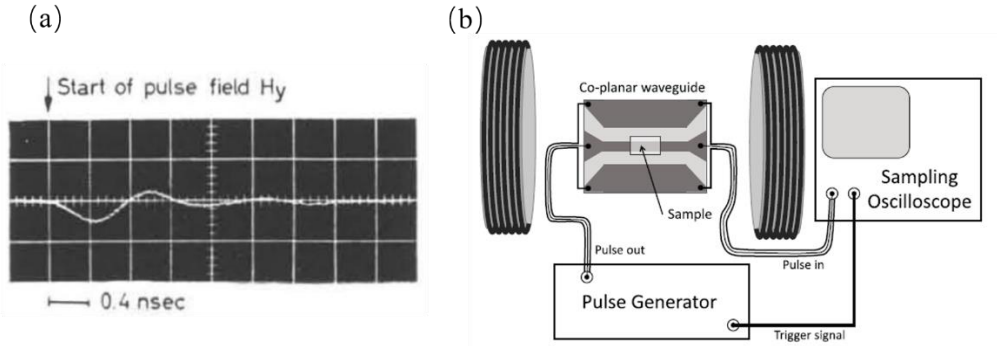

Figure 1.3: (a) Oscillogram of a free oscillation of the magnetization [39]. Schematic illustration of pulsed inductive microwave magnetometry (PIMM) [45].

The time-resolved magneto-optical effect detection is used to directly monitor the magnetisation precession in the early 1990s. Freeman *et al.* applied this technique on the EuS [46], yttrium-iron-garnet (YIG) [47] and permalloy [48] films. As illustrated in Figure 1.4(a), a photoconductive switch structure is designed on the GaAs substrate and this switch is triggered by focusing the pump beam on the open end of the transmission line. The generated current pulse propagates through the transmission line, creating a pulsed magnetic field that excites the magnetization of the sample. Hicken and Wu [49] also used this method to explore the magnetization behaviour as a function of the pulsed field, shown in Fig. 1.4(b). It shows the measured time dependent Kerr rotations in sub-ns time scale.

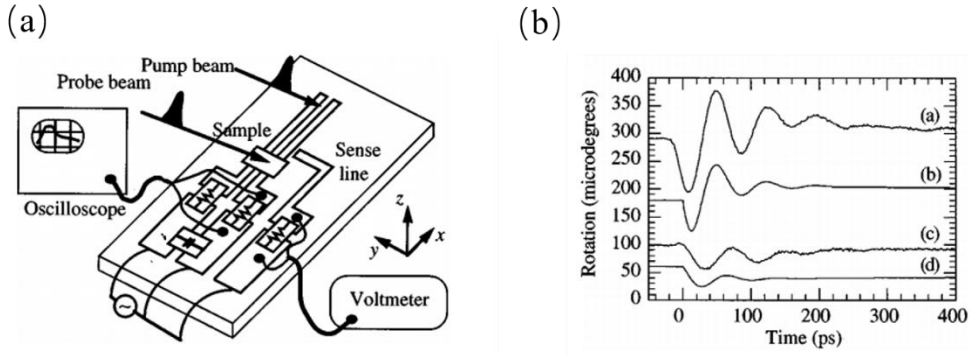

Figure 1.4: (a) A schematic illustration of the photoconductive switch structure. (b) measured time dependent Kerr rotation in sub-ns time scale [49].

Besides the pulsed magnetic field, the magnetization precession can also be directly stimulated by the pump laser pulse. Gaurisco *et al.* studied the thermomagnetic writing and precession processes by excite the magnetization directly using a ps pulse laser [50]. In 1999, Ju and Nurmikko *et al.* observed an damped oscillation in the magnetisation response after fs laser excitation in ferromagnetic/antiferromagnetic exchange coupled bilayer films (NiFe/NiO) [51]. Later, in 2002, van Kampen *et al.* successfully demonstrated coherent magnetic precession using an all-optical pump-probe in thin Ni films [52], as shown in Fig. 1.5(b). Stimulated standing spin waves were also directly observed in the time domain. The frequency of coherent precession was explained by the same method used in traditional ferromagnetic resonance (FMR), and thus this laser-induced magnetisation precession is also known as all-optical FMR. A comparison between the pump-probe method and traditional FMR will thus be presented in Section 3.1.2.

As shown schematically in Fig. 1.5(a), to study the magnetisation precession, an external field is applied in the near-hard-axis or the away-from-easy-axis directions in order to create a noncollinear geometry of the anisotropy, applied, and demagnetisation fields. This precession process was well described, and this process is depicted in Fig. 1.5(c). Without any stimulus, the magnetisation orientation is determined by the effective field, which is comprised of the fields mentioned above. Upon pump pulse excitation, the magnetic response undergoes several distinct processes. Initially, not as well as experiencing ultrafast demagnetisation, the anisotropy of the film changes (known as a quench). This results in a change in the equilibrium orientation, triggering an initial precession of the magnetisation around a new equilibrium orientation. This initial precession is not visible in the TRMOKE response due to its small effect compared to the dominant demagnetisation effect. After heat dissipation, the anisotropy and the original equilibrium angle are restored after about 10 ps for Ni. However, at this point, the magnetisation is not in equilibrium due to its initial displacement. Thus, a magnetisation precession with respect to the equilibrium state begins, which lasts for hundreds of picoseconds.

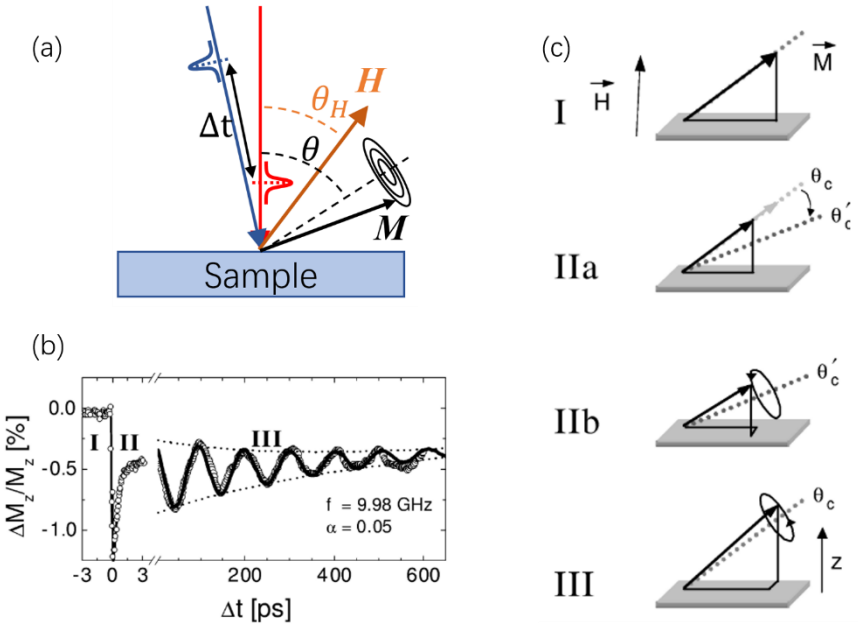

Figure 1.5: (a) Schematic pump-probe TRMOKE setup. (b) Observed magnetisation precession in a Ni thin film. (c) The stages of the precession process [52].

The laser-induced magnetisation precession is not as complicated as demagnetisation, although the electron, spin, and lattice also interact with each other in this case; however, the initial demagnetisation is not a subject of interest. The coherent precession starts when the system is in a quasi-equilibrium state and the temperatures of all three subsystems are equal or very close to. In general, this technique thus provides a convenient way to investigate coherent magnetisation as well as other nonuniform spin waves in the time domain. A great deal of excellent work has been reported [53-60] in this subfield, and this laser-induced magnetisation precession will be the main experimental method used in this thesis. Further theoretical details of the magnetisation precession will thus be presented in Section 2. 2

1.3 Magnetic damping

One of the most important scientific topics in the study of magnetic precession is magnetic damping. As mentioned, the energy consumption (critical current) of the process is strongly affected by the damping constant in MRAM devices. The ultimate

speed of magnetic switching is also affected by this damping [61], and thus, magnetic damping is a key parameter for exploiting next-generation spintronic devices as well as for understanding the underlying physics.

In ferromagnetic systems, the spin dynamics are described by the Landau-Lifshitz-Gilbert (LLG) equation, in which a phenomenological parameter, Gilbert damping constant, defines magnetisation relaxation. There are numerous energy terms defining the total magnetic free-energy, including Zeeman energy, demagnetization energy, exchange energy, anisotropy energy, and magneto-elastic energy. The magnetization behaviour is determined by the energy transformation and dissipation from the magnetic excitation to the lattice of the material [62-66]. This energy transformation and dissipation is described by the magnetic damping. Further details of the LLG equation and the description of the magnetic free-energy will be introduced in next chapter.

In general magnetic damping consists of two parts: intrinsic (Gilbert) and extrinsic contributions [62-64, 66-73]. Although these energy dissipation channel all end in microscopic thermal motion, they can be referred to as ‘fast (direct)’ and ‘slow (indirect)’ processes, respectively [74-77]. Sparks [78] uses spin wave interactions to describe several energy dissipation channels in bulk ferromagnetic systems and the energy would eventually be dissipated to the lattice via the magnon-phonon interaction. In these processes, different energy dissipation channels are described, namely uniform precession (Kittel mode), two magnon scattering and three (thermal) magnon scattering mechanisms. Two magnon scattering involves uniform precession and non-uniform mode while three magnon scattering includes the thermal magnons based on two magnon scattering [45, 79, 80].

The magnetic damping can be extracted from the linewidth determined from an FMR measurement, which will be introduced in detail in next chapter. It is found that the resonance linewidth depends on the orientation of the precessional motion with respect to the magnetic easy-axis. The narrower linewidth (small damping) was found when the applied field was applied perpendicular to the sample plane compared to when it was parallel to the film. As introduced in above, these observations are caused by

intrinsic and extrinsic damping contributions [63, 66-68, 81]. People can obtain the intrinsic damping by subtracting the extrinsic term from the total measured damping. Recently, an ultra-low intrinsic damping (black squares with lines) is observed in CoFe alloy (Fig. 1.6) which is obtained from the measured total damping (red circles with lines) subtracting the spin-pumping damping (grey line) and radiative damping (green line) [82].

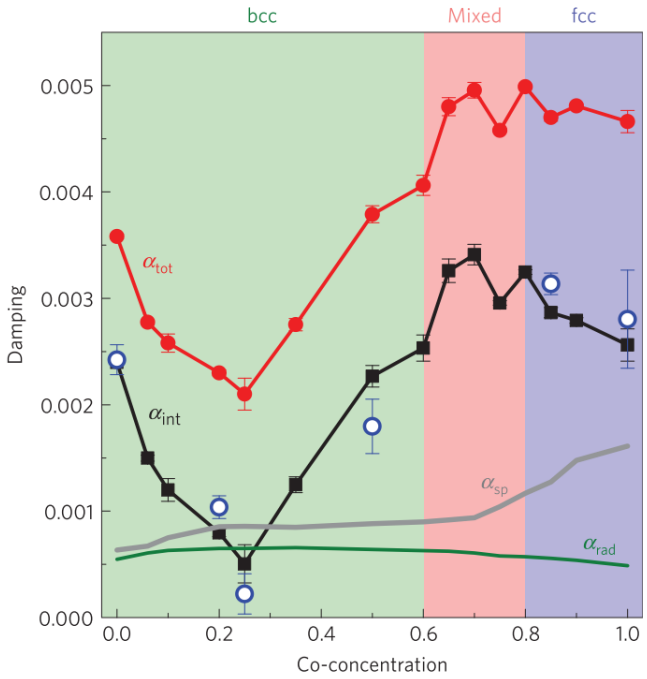

Figure 1.6 ultra-low intrinsic damping (black squares with lines) in CoFe alloy [82].

In a broad sense, the interactions between the magnetisation and the other degrees of freedom, such as the electrons and lattice, allow energy to leak from the magnetic system. Thus, magnetic relaxation processes involving electron scattering with phonons and magnons is the source of an intrinsic contribution to the magnetic damping. Several mechanisms were proposed as responsible for the intrinsic damping, including spin-orbit coupling, the phonon-drag mechanism, and the eddy-current mechanism [83]. The mechanism of magnon relaxation by phonon drag was proposed in 1998 [76]. However, according to the calculations, phonon magnetic damping is estimated to be ~0.001 which is about 32 times smaller than the intrinsic damping constant obtained in Ni. Thus this phonon-magnon relaxation mechanism is experimentally determined to be negligible.

Another realisation mechanism originates from the eddy currents in ferromagnetic materials and is induced by the precession of magnetisation. Eddy current in a ferromagnetic material comes from the magnetization precession. The conduction electrons lead to the electromagnetic microwave field and this contributes to the magnetization relaxation. The energy dissipation in this process is proportional to the conductivity of the material. The calculated eddy current contribution to Gilbert damping is given by

$$\alpha_{\text{eddy}} = \frac{1}{6} M_s \gamma \left(\frac{4\pi}{c}\right)^2 \sigma d^2, \tag{1.1}$$

Where γ is the gyromagnetic ratio, d is the film thickness, and σ is the conductivity. This eddy current contribution to magnetic damping is proportional to the square of film thickness, and thus is significantly reduced for thin films. For nickel, the eddy current damping contribution is particularly small for thicknesses of up to 100 nm [84]. In our experiments, the samples are usually much thinner than this thickness, hence the eddy current damping contribution is not important.

The other leading mechanism of magnetic damping in metals is spin-orbit interaction with itinerant electrons. In 1976, by introducing a spin-orbit coupling Hamiltonian, Kambersky [65] related intrinsic damping in ferromagnetic damping to the incoherent scattering of itinerant conduction electrons by phonons and magnons. During this process, energy and angular momentum was lost from localised d-electrons to the itinerant s-electrons via an exchange interaction. This process was accompanied by the relaxation of the spins of the s-electrons to the lattice through an incoherent spin-flip process arising from spin-orbit coupling. Alongside the s-d exchange relaxation, a so-called Fermi surface breathing model was considered to contribute to the intrinsic damping. As in ferromagnetic metals, the shape of a Fermi surface changes when the magnetisation direction is changed; the Fermi surface becomes periodically distorted due to the magnetisation precession. Thus, a periodical variation of the Fermi surface due to spin-orbit coupling is introduced by uniform precession, which is also known as a breathing Fermi surface [85]. In 2002, Kunes and Kambersky [86] calculated the breathing Fermi surface Gilbert damping in transition metals, and this was

quantitatively in agreement with the experimental data. Later, Ebert *et al.* [87] and Lounis *et al.* [88] suggested that intrinsic damping is proportional to the density of states (DOS) at the Fermi level, $D(E_F)$, in the breathing Fermi surface model in cases of unchanged spin-orbit coupling and small electron-phonon coupling. This correlation between $D(E_F)$ and intrinsic damping has been demonstrated in CoFe alloys [82], Co_2FeAl Heusler [89], and MnGa alloys [54] via comparisons between measured magnetic damping and calculated DOS. No direct experimental observations demonstrating this correlation have been reported, however.

The extrinsic contribution to damping results, in general, from magnetic inhomogeneity. Ideally, in a perfect lattice without any defects or surfaces, these contributions would not exist; this is why these contributions to damping are extrinsic. A two-magnon scattering theory was applied to thin films in 1999 by Arias and Mills [90] in which a uniform precession mode scatters into non-uniform modes (spin waves) due to structural defects. In this process, the uniform precession is dephased by other modes and the relaxation time of the uniform mode is decreased. The magnetic energy in the uniform precession is pumped into other modes, and thus the magnetic damping is enhanced. This two-magnon scattering effect was demonstrated to be attributable to an enhancement of magnetic damping in Cr/Fe/GaAs heterostructures compared to Au/Fe/GaAs due to Cr/Fe surface-induced spatially inhomogeneous exchange biases [91]. Where the external magnetic field is very strong, the effect of magnetic inhomogeneity and two-magnon scattering will be supressed. In such cases, the measured magnetic damping will be close to the intrinsic state. In next chapter, the intrinsic damping, extrinsic damping and the interfacial and spin pumping contributions to intrinsic damping will be discussed in detail.

1.4 Thesis overview

The work presented in this thesis focusses on the study of magnetic damping using the method of time-resolved MOKE in various magnetic materials. In order to explore the underlying mechanism and the physics nature of the magnetic damping, some

advanced characterisation approaches are applied, including angle-resolved photoemission spectroscopy and X-ray magnetic circular dichroism. Particular attention is given to the influence of electronic structure, spin-orbital coupling and the coupling between multiple spin-wave modes. The work provides new physical insight to understanding and controlling the magnetic damping, consequently facilitate designing the next-generation spintronic devices.

In chapter 1, a brief introduction and basic background of the ultrafast spin dynamics have been presented. Three sub-fields have been introduced including ultrafast demagnetisation, laser-induced magnetisation precession and all-optical magnetic switching. The origin of the magnetic damping has also been discussed.

The theoretical background of magnetisation dynamics, particularly with regard to magnetisation precession, will be presented in chapter 2. Two magneto-optical effects, Kerr and Faraday effects, will be explained. The Landau-Lifshitz-Gilbert equation, a phenomenological description of the magnetisation precession, will be introduced and a precession frequency dispersion relationship will be derived from the LLG equation. The energy terms involved in the process will be discussed and the Kittel formula will be derived. Finally, the derivation of the Gilbert damping will be presented and basic concepts of spin waves will be presented.

In chapter 3, details of the experimental techniques used in this thesis will be introduced. Characterisation techniques includes vibrating sample magnetometer (VSM) and Superconducting Quantum Interference Device (SQUID) VSM, TRMOKE and ARPES. As the main approach to study the magnetic damping, TRMOKE will be introduced in details and the comparison between TRMOKE and FMR will also be addressed. Several sample preparation methods will also be briefed such as molecular beam epitaxy (MBE) and pulsed laser deposition (PLD).

Chapter 4 will present the experiments and the results starting with a simple, but of fundamental importance, Fe/GaAs heterostructures. A set of ultrathin Fe/Cr/GaAs samples with a fixed thickness, 10 ML, of Fe layer and various thickness of Cr interlayer, are grown using MBE. Static magnetic properties are characterized using VSM while the magnetic damping is measured using TRMOKE. To explore the relation between

the reported uniaxial anisotropic magnetic damping and the measured uniaxial magnetic anisotropy, XMCD measurements are implemented to obtain the spin and orbital moments of Fe atoms, respectively. It is suggested that these two anisotropic phenomena have different physical mechanisms.

The TRMOKE methods are also applied to investigate the magnetic damping in the Heusler alloy Co_2FeAl, and the results will be presented in chapter 5. Furthermore, the *in-situ* ARPES measurements provides a direct opportunity to study the electronic structure, especially the density of state at Fermi level. By changing the temperature of growth, the Co_2FeAl samples present completely different values of magnetic damping. The difference in magnetic damping is explained by the different electronic structures observed between the samples correspondingly.

The last part of the results, presented in chapter 6, will focus on the magnetisation dynamics in high quality Fe_3O_4. Via an annealing process at high temperature, a high-quality Fe_3O_4 thin film in single crystalline structure without defects is obtained. In comparison, an as-deposited film with structural defects is used. A non-intuitive finding is that the magnetic damping obtained in the post-annealed sample is much higher than the value in the as-deposited one. This enhanced magnetic damping is attributed to the emergence of an additional perpendicular standing spin wave in the post-annealed sample while single uniform precession is observed in the as-deposited film.

In the final chapter, the general conclusions on the thesis will be presented. Also, future works or complementary experiments which could be accomplished in the future are recommended.

Chapter 2 Theory of magnetisation dynamics

In this chapter, the theoretical background of magnetisation dynamics, particularly with regard to magnetisation precession, will be presented. The origins of several magneto-optical effects, including Kerr and Faraday effects, will also be explained, as these are the basis of the experimental techniques employed in this thesis. The equation of motion for the damping magnetisation precession will be derived from the LLG equation, and the frequency dispersion relationship will be derived for uniform precession mode. By introducing various contributions to magnetic free energy, the Kittel formula will be derived and, importantly, the Gilbert damping constant will be derived from the relaxation time and frequency of the precession. Various spin-wave modes will also be introduced.

2.1 Magneto-optical Effects

Magneto-optic effects originate from the interaction of electromagnetic radiations with magnetic materials [92]. The two magneto-optical phenomena concerned in this thesis are: the Kerr effect and the Faraday effect. The Faraday effect causes a rotation of the polarisation plane of light that is linearly proportional to the component of the magnetisation in the direction of propagation after transmission, while the Kerr effect rotates the polarisation plane of reflective light from a sample surface.

2.1.1 Magneto-optical Kerr Effect (MOKE)

When linearly polarised light reflects from a magnetic surface, it becomes elliptically polarised and its polarisation axis is also rotated. This effect is known as the Kerr effect, as it was discovered by John Kerr in 1870. Before discussing the Kerr effect, the thickness that the light can penetrate in terms of interacting with magnetic materials must be considered; this is known as the skin depth, δ [93]. This depth is determined

by the frequency of incident light and the electric properties of the material itself. The expression for skin depth is given by

$$\delta = \sqrt{\frac{2\rho}{\omega\mu_r\mu_0}}, \tag{2.1}$$

where ρ is the resistivity of the material, ω is the angular frequency of the incident light, and μ_r and μ_0 are the relative magnetic permeability of the material and the permeability of free space, respectively. In the case of reflection from bulk material it is only the skin depth region, typically $\sim$10 to 20 nm in most metals, that contributes to the Kerr effect [93].

An experimental geometry for observing the Kerr effect is schematically shown in Fig. 2.1. A beam of light, $\boldsymbol{E_i}$, incident on the surface of a magnetic sample, can be treated as a superposition of a p-polarised light and a s-polarised light. The p-polarised light has an electric field vector, E_{ip}, which is parallel to the plane of incidence, while the s-polarised light has its electric field vector, E_{is}, perpendicular to the plane of incidence. Similarly, E_{rp} and E_{rs} correspond to the p-polarised and s-polarised components in the reflected light, respectively. In such cases, the reflection at the sample surface can be expressed by using the Fresnel reflection matrix R, where

$$\boldsymbol{E_r} = R\boldsymbol{E_i}. \tag{2.2}$$

This can be re-written in the form of p- and s-polarised components:

$$\begin{pmatrix} E_{rs} \\ E_{rp} \end{pmatrix} = \begin{pmatrix} r_{ss} & r_{sp} \\ r_{ps} & r_{pp} \end{pmatrix} \begin{pmatrix} E_{is} \\ E_{ip} \end{pmatrix}. \tag{2.3}$$

where r_{ss}, r_{sp}, r_{ps}, and r_{pp}, are the Fresnel reflection coefficients and the subscripts denote the scattering plane dependence of each element such that r_{ps} represents the ratio between the complex electric field amplitude of p-polarised reflected light and that of s-polarised incident light. Expression of the Fresnel reflection coefficients can be calculated by applying the reflection boundary condition [94]:

$$r_{ss} = \frac{\mu_2 N_1 \cos\theta_1 - \mu_1 N_2 \cos\theta_2}{\mu_2 N_1 \cos\theta_1 + \mu_1 N_2 \cos\theta_2}, \tag{2.4}$$

$$r_{sp} = \frac{i\mu_1\mu_2 N_1 N_2 \cos\theta_1 \, Q(m_x \sin\theta_2 + m_z \cos\theta_2)}{(\mu_1 N_2 \cos\theta_1 + \mu_2 N_1 \cos\theta_2)(\mu_2 N_1 \cos\theta_1 + \mu_1 N_2 \cos\theta_2)\cos\theta_2}, \tag{2.5}$$

$$r_{ps} = \frac{-i\mu_1\mu_2 N_1 N_2 \cos\theta_1 \, Q(m_x \sin\theta_2 - m_z \cos\theta_2)}{(\mu_1 N_2 \cos\theta_1 + \mu_2 N_1 \cos\theta_2)(\mu_2 N_1 \cos\theta_1 + \mu_1 N_2 \cos\theta_2)\cos\theta_2}, \tag{2.6}$$

$$r_{pp} = \frac{\mu_2 N_1 \cos\theta_1 - \mu_2 N_1 \cos\theta_2}{\mu_1 N_2 \cos\theta_1 + \mu_2 N_1 \cos\theta_2} + \frac{2i\mu_1\mu_2 N_1 N_2 \cos\theta_1 \, Q m_y \sin\theta_2}{\mu_1 N_2 \cos\theta_1 + \mu_2 N_1 \cos\theta_2}, \tag{2.7}$$

where μ_1, μ_2 are the permeabilities of media 1 and 2; N_1, N_2 are the complex indices of refraction; θ_1 is the incident angle; θ_2 is the refracted angle; and Q is the complex magneto-optical constant, which is introduced in the permittivity tensor:

$$\varepsilon = \varepsilon_q \begin{bmatrix} 1 & -iQm_z & iQm_y \\ iQm_z & 1 & -iQm_x \\ -iQm_y & iQm_x & 1 \end{bmatrix}, \tag{2.8}$$

where m_x, m_y, m_z are the magnetisation components along the x, y, and z axes, respectively. The Kerr rotation, θ_k, and ellipticity, η_k, for individual s- and p-polarised components are the defined as per equations 2.9 to 2.12, while the total Kerr rotation and ellipticity are superpositions of the two components [94]:

$$\theta_{ks} = \mathrm{Re}(r_{ps}/r_{ss}), \tag{2.9}$$

$$\theta_{kp} = \mathrm{Re}(r_{sp}/r_{pp}), \tag{2.10}$$

$$\eta_{ks} = \mathrm{Im}(r_{ps}/r_{ss})\mathrm{Re}(r_{ps}/r_{ss}), \tag{2.11}$$

$$\eta_{kp} = \mathrm{Im}(r_{sp}/r_{pp})\mathrm{Re}(r_{sp}/r_{pp}). \tag{2.12}$$

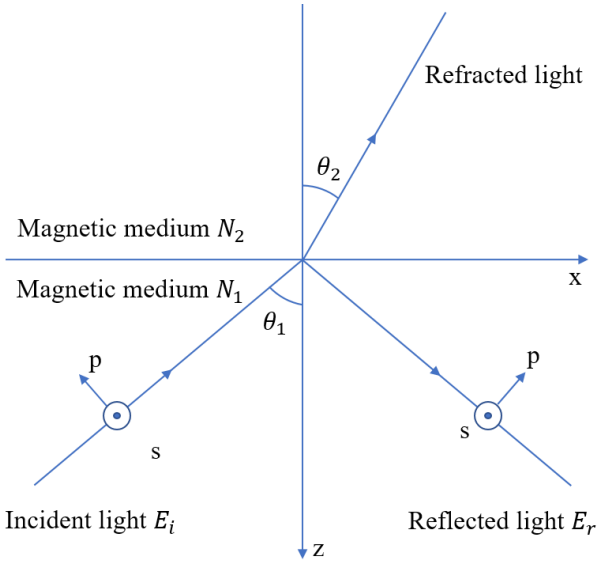

Figure 2.1: Schematic geometry of the Kerr effect. The s- and p-polarised components of the incident and reflected lights are defined. Sample surface is at x-y plane.

From Equations 2.4 to 2.7, given a certain reflection boundary with a fixed incident angle, the Fresnel reflection coefficients are determined by the x-, y-, and s-components of the magnetisation. This means that the Kerr effect is not only affected by the magnitude of the magnetisation but also determined by its orientation. Fig. 2.2 shows the configurations of three different geometries in respect to the three different magnetisation components. The contribution from z- or perpendicular component of the magnetisation is defined as the polar MOKE, while both p- and s-polarised incident lights sense the z-component resulting in an m_z-dependent elliptical polarisation. As the effect decreases with an increasing incident angle, θ_1, normal incidence is sought to achieve maximum of the polar MOKE signal. The longitudinal MOKE is defined as the contribution of the x-component of magnetisation. Similar to polar MOKE geometry, the longitudinal MOKE influences both p- and s-polarised incident lights. However, in contrast to polar MOKE, the longitudinal MOKE effect is proportional to the incident angle, θ_1, favouring a large θ_1 for large longitudinal Kerr rotations. In a transverse MOKE configuration, only the y-component of magnetisation contributes to the Kerr rotation, and unlike polar and longitudinal MOKEs, only the p-polarised incident light can sense the y-component of magnetisation and give rise to transverse MOKE [95].

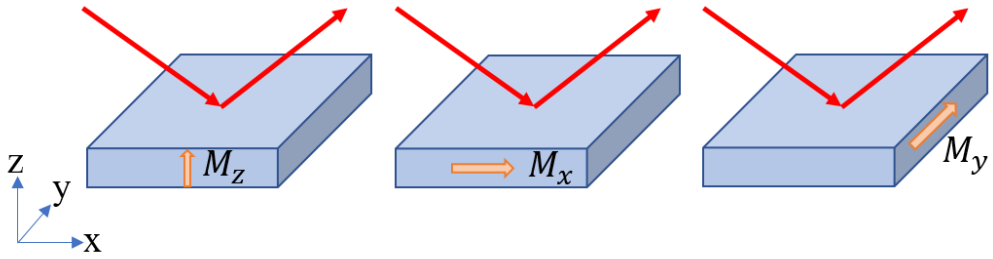

Figure 2.2: schematic illustrations of Polar (left), longitudinal (middle) and transverse (right) MOKE.

It is worth to the note that after reflected from the surface, the magnetic material can not only make a Kerr rotation θ_k, but also make the linear polarization light to an elliptical light η_k, as illustrated in Fig. 2.3. In ultrafast pump-probe measurements, the different dynamics between the Kerr rotation and ellipticity have indeed been observed

in Ni [27] and $CoPt_3$ [28]. As concluded by Bigot *et al.*, the time evolution of the real and imaginary parts of the complex MO response is different only for very short temporal delays after laser pumping ($t \leq 150$ fs). After this short time delay, the profile of both the real (rotation) and imaginary (ellipticity) parts become identical and ascribed to truly magnetic effects. Therefore, in our magnetization precession measurements in the time scale of sub-ns, the time dependent ellipticity change is not needed to be measured in addition to the Kerr rotation.

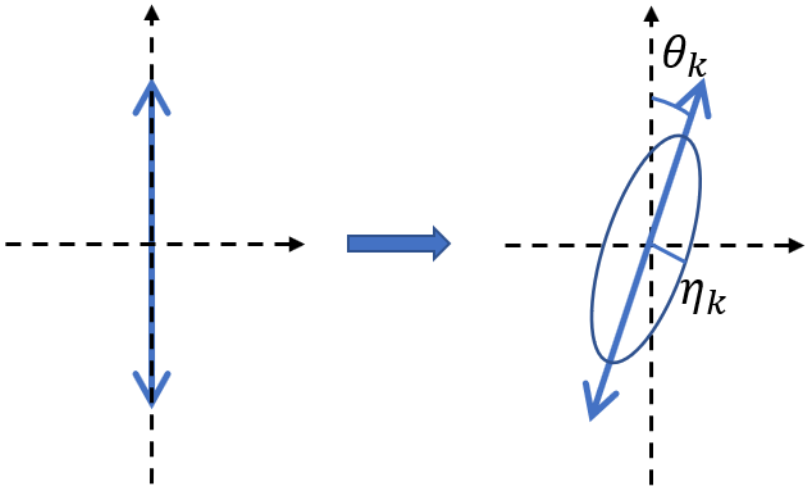

Figure 2.3: schematic illustration of Kerr rotation and Kerr ellipticity change.

2.1.2 Magneto-optical Faraday Effect

In 1845, Faraday discovered the magneto-optic Faraday effect, making the first observation that magnetised material can affect the polarisation of light. The difference between the Faraday and Kerr effects lies in the fact that the magnetised material will change the polarisation of the light; however, the Kerr effect changes the reflected light while the Faraday effect changes the transmitted light. A linearly polarised incident light can be considered to be a superposition of a left-handed circularly polarised (LCP) component and a right-handed circularly polarised (RCP) component. The Faraday effect is thus a phenomenon of circular magnetic birefringence: where different refractive indices exist, the LCP and RCP components have different phase velocities

when passing through a magnetic material, resulting in phase differences between these two components that lead to a rotation of the polarisation plane. In fact, if a magnetic circular dichroism, which refers to the different absorptions of RCP and LCP components in a magnetic material, is considered, the transmitted light will become an elliptical polarisation as well as undergoing rotation of polarisation.

The Faraday rotation of transmitted light can be described by the following equation [96]:

$$\beta = \nu_{\mathrm{V}} B d, \tag{2.13}$$

where β is the rotation of the polarisation plane, B is the magnetic flux density in the direction of propagation of the light, d is the path length of the light in the magnetic medium, and ν_{V} is the Verdet constant of the material. From Equation 2.13, it can be seen that the angle of Faraday rotation is not only determined by the magnetic flux density (magnetisation) but also proportional to the length of path within the magnetic material (thickness).

The magneto-optical Faraday effect as well as MOKE are widely employed in time-resolved magnetisation measurements, similar to the use of time-resolved MOKE. However, as the Faraday effect measures the polarisation change in transmitted light, the sample has to be transparent, which limits its application in time-resolved magnetisation measurements compared to MOKE.

2.2 Magnetisation precession

As mentioned in the previous chapter, a magnetisation precession can be stimulated by application of a laser pulse. This section will present the theoretical description and derivation of the precessional motion, beginning with a quantum mechanical description of the precession of a free electron spin, and deriving the Landau-Lifshitz (LL) equation. When the damping term is introduced into this LL equation, the Landau-Lifshitz-Gilbert equation can be derived. Consequently, the frequency dispersion relationship for the uniform precession (Kittel mode) can be derived from the LLG

equation. By introducing these different contributions to magnetic free energy, the Kittel formula can thus be derived to describe the frequency dispersion relationship in real magnetic samples.

2.2.1 LLG equation

In quantum mechanics, Schrödinger's equation describes the time evolution of an observable physical quantity by its commutator with the Hamiltonian. For a single isolated spin $\langle \boldsymbol{S} \rangle$ (spin operator), the dynamic behaviour is determined by [97]

$$\mathrm{i}\hbar \frac{\mathrm{d}}{\mathrm{dt}} \langle \boldsymbol{S} \rangle(t) = \langle [\boldsymbol{S}, \mathcal{H}(t)] \rangle. \tag{2.14}$$

Assuming the single spin is solely affected by a (time-dependent) external field, $\boldsymbol{H}$, only the Zeeman energy term is thus needed in the Hamiltonian:

$$\mathcal{H} = -\frac{g\mu_B}{\hbar} \boldsymbol{S} \cdot \boldsymbol{B}, \tag{2.15}$$

where $\boldsymbol{B}$ is equal to $\mu_0 \boldsymbol{H}$ in vacuum, μ_B is the Bohr magneton, and g is the gyromagnetic factor. Taking the x-component in Equation 2.14 into consideration, for instance, yields

$$\begin{aligned} [S_x, \mathcal{H}(t)] &= -\frac{g\mu_B}{\hbar} \left[S_x, S_x B_x(t) + S_y B_y(t) + S_z B_z(t) \right] \\ &= -\frac{g\mu_B}{\hbar} \left(B_y(t) \left[S_x, S_y \right] + B_z(t) [S_x, S_z] \right). \end{aligned} \tag{2.16}$$

Substituting by commutation rules for the commutators $\left[S_x, S_y \right]$ and $[S_x, S_z]$

$$\begin{aligned} \left[S_x, S_y \right] &= \mathrm{i}\hbar S_z, \\ \left[S_y, S_z \right] &= \mathrm{i}\hbar S_x, \\ [S_z, S_x] &= \mathrm{i}\hbar S_y, \end{aligned} \tag{2.17}$$

Equation 2.16 becomes

$$[S_x, \mathcal{H}(t)] = -\frac{g\mu_B}{\hbar} \mathrm{i}\hbar \left(B_y(t) S_z - B_z(t) S_y \right). \tag{2.18}$$

The other two components of the spin can also be derived correspondingly, allowing the time evolution of the mean value of the spin operator to be obtained:

$$\frac{\mathrm{d}}{\mathrm{dt}} \langle \boldsymbol{S} \rangle(t) = \frac{g\mu_B}{\hbar} \left(\langle \boldsymbol{S} \rangle(t) \times \boldsymbol{B}(t) \right). \tag{2.19}$$

The geometric relationship between the magnetisation, $\boldsymbol{M}$, and the spin operator $\langle \boldsymbol{S} \rangle$ is given by

$$\boldsymbol{M} = \gamma \langle \boldsymbol{S} \rangle, \tag{2.20}$$

where γ is the gyromagnetic ratio, which is equal to $\frac{g\mu_B}{\hbar}$. In the SI system, γ_0 is usually defined as

$$\gamma_0 = \mu_0 \frac{g|\mu_B|}{\hbar} = -\mu_0 \gamma. \tag{2.21}$$

Thus, Equation 2.19 can be re-written in the form that governs magnetisation motion

$$\frac{\mathrm{d}}{\mathrm{dt}} \boldsymbol{M}(t) = -\gamma_0 [\boldsymbol{M}(t) \times \boldsymbol{H}(t)]. \tag{2.22}$$

Equation 2.22 is then known as the Landau-Lifshitz (LL) equation [98], and it is used to describe the spin motion.

If the applied field is time independent, two specific properties are derived from Equation 2.22 by multiplying successively by $\boldsymbol{M}$ and $\boldsymbol{H}$:

$$\frac{\mathrm{d}}{\mathrm{dt}} [\boldsymbol{M}(t)]^2 = 0, \quad \frac{\mathrm{d}}{\mathrm{dt}} [\boldsymbol{M}(t) \cdot \boldsymbol{H}] = 0. \tag{2.23}$$

The first equation states that he modulus of the magnetisation is not changed as a function of time, while the second equation implies that the angle between the field and the magnetisation also remains unchanged during the spin motion. Thus, the precessional motion of magnetisation around the applied field is described by the LL equation, as shown in Fig. 2.4(a). The angular frequency of the precession is a linear function of the applied field $\omega = \gamma_0 H$, which is also known as the Larmor frequency.

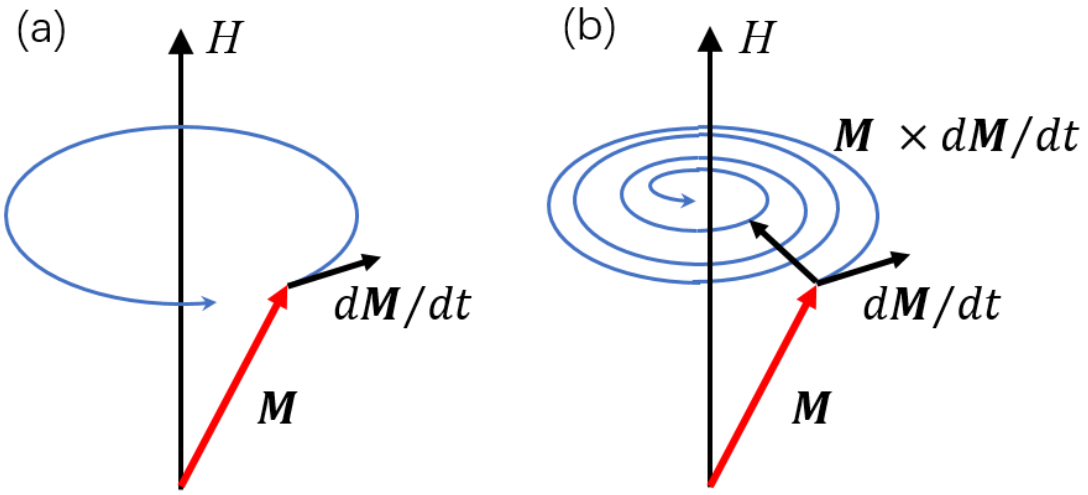

Figure 2.4: magnetisation precession without (a) and with damping term (b).

The main limitation of the LL equation is that once the magnetisation is taken out of the equilibrium state, the precession around the external field is predicted to last for an infinitely long period. This is in conflict with the experimental fact that the magnetisation will be aligned with the field in a given time. Hence, a dissipative term is required, which means that the LL equation requires the addition of a damping term that allows the precession process to stop after a finite time to allow the magnetisation to become aligned with the field. Gilbert [62, 99] applied a thermodynamical approach that allowed the introduction of a dissipative term into the LL equation in the following form:

$$\frac{\alpha}{M_s}\left(\boldsymbol{M}\times\frac{\mathrm{d}}{\mathrm{dt}}\boldsymbol{M}\right), \tag{2.24}$$

where α is the dimensionless Gilbert damping constant and M_s is the saturation magnetisation. With the help of this term, the magnetisation precession eventually stop whick makes the magnetisation aligned. Thus, the equation to describe the motion of magnetisation is given by the now-well-known Landau-Lifshitz-Gilbert (LLG) equation:

$$\frac{\mathrm{d}\boldsymbol{M}}{\mathrm{dt}} = -\gamma_0(\boldsymbol{M}\times\boldsymbol{H}) + \frac{\alpha}{M_s}\left(\boldsymbol{M}\times\frac{\mathrm{d}}{\mathrm{dt}}\boldsymbol{M}\right). \tag{2.25}$$

2.2.2 Frequency dispersion relationship

In magnetic materials, the magnetisation precession frequency cannot be treated as equivalent to the Larmor frequency due to the various contributions of free magnetic energy. Furthermore, alongside the uniform precession mode, other different precession modes can exist experimentally, especially in pump-probe experiments. Nevertheless, the frequency dispersion for the uniform precession mode, which is also called the Kittel mode ($k = 0$), must be derived. This mode is the basic but dominant mode that is homogeneous throughout the entire sample in the presence of an external magnetic field. As the uniform precession frequency is not affected by the Gilbert damping term (the second term in Equation 2.25) but only determined by the term $(\boldsymbol{M} \times \boldsymbol{H}_{\mathbf{eff}})$, only the LL equation is needed for this derivation:

$$\frac{\mathrm{d}\boldsymbol{M}}{\mathrm{dt}} = -\gamma_0 \boldsymbol{M} \times \boldsymbol{H}_{\mathbf{eff}}. \tag{2.26}$$

Note that, unlike in the case of a single spin, the effective field $\boldsymbol{H}_{\mathbf{eff}}$ consists not only of the external magnetic field but also other contributions, such as the Zeeman energy, anisotropy energy, and demagnetisation energy. In general, $\boldsymbol{H}_{\mathbf{eff}}$ can be deduced from the total free magnetic energy, F, using the following the expression [100]

$$\boldsymbol{H}_{\mathbf{eff}} = -\frac{1}{\mu_0 M_s}\frac{\partial F}{\partial \boldsymbol{m}}, \tag{2.27}$$

where $\boldsymbol{m}$ is the unit vector of the magnetisation $\boldsymbol{M}$.

Compared to Cartesian coordinates, spherical coordinates, as schematically shown in Fig. 2.5, are more convenient and common to use in the derivation of magnetisation precessions. In spherical coordinates, the left side term in the LL equation (Equation 2.26) can be expressed as

$$\frac{\mathrm{d}\boldsymbol{M}}{\mathrm{dt}} = M_s \frac{d\theta}{dt}\boldsymbol{e}_{\boldsymbol{\theta}} + M_s \sin\theta \frac{d\varphi}{dt}\boldsymbol{e}_{\boldsymbol{\varphi}}. \tag{2.28}$$

Substituting Equation 2.27 into Equation 2.26 and re-writing the left side term in Equation 2.26 in spherical coordinates gives

$$\boldsymbol{M} \times \boldsymbol{H}_{\mathbf{eff}} = \frac{1}{\mu_0 \sin\theta}\frac{\partial F}{\partial \varphi}\boldsymbol{e}_{\boldsymbol{\theta}} - \frac{1}{\mu_0}\frac{\partial F}{\partial \theta}\boldsymbol{e}_{\boldsymbol{\varphi}}. \tag{2.29}$$

Therefore, the LL equation can be re-written as

$$\frac{d\theta}{dt} = -\frac{\gamma}{M_s \sin\theta}\frac{\partial F}{\partial \varphi}$$
$$\frac{d\varphi}{dt} = \frac{\gamma}{M_s \sin\theta}\frac{\partial F}{\partial \theta}. \quad (2.30)$$

The $\boldsymbol{e_r}$ component is ignored, as the modulus of $\boldsymbol{M}$ is assumed to be a constant of the value M_s.

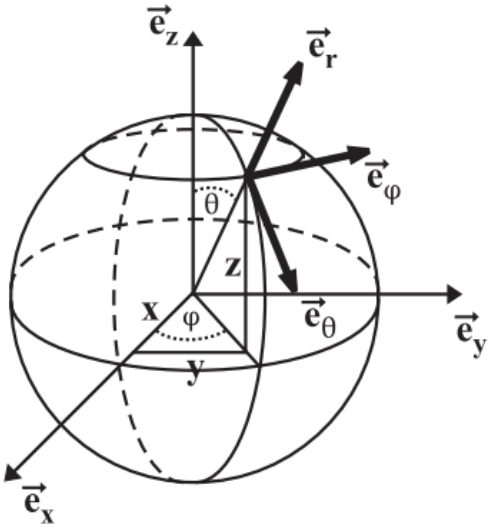

Figure 2.5: Schematic illustration of the spherical coordinate system [100].

The free magnetic energy, F, can be converted into a Taylor series for small variations around the equilibrium position; the first-order approximation is expressed as

$$F = F_0 + \frac{1}{2}\left(F_{\theta\theta}\theta^2 + 2F_{\theta\varphi}\theta\varphi + F_{\varphi\varphi}\varphi^2\right). \quad (2.31)$$

Consequently, Equation 2.30 becomes:

$$\frac{d\theta}{dt} = -\frac{\gamma}{M_s \sin\theta}\left(F_{\theta\varphi}\theta + F_{\varphi\varphi}\varphi\right)$$
$$\frac{d\varphi}{dt} = \frac{\gamma}{M_s \sin\theta}\left(F_{\theta\theta}\theta + F_{\theta\varphi}\varphi\right). \quad (2.32)$$

As per previous discussion, θ and φ must follow harmonic oscillations with the same angular frequency ω, around their equilibrium values θ_0 and φ_0:

$$\theta - \theta_0 = \theta_A \exp(-i\omega t)$$
$$\varphi - \varphi_0 = \varphi_A \exp(-i\omega t), \quad (2.33)$$

where θ_A and φ_A are the amplitudes of these angles in the precession. Thus, a set of

differential equations can be derived from Equation 2.32:

$$\left(\frac{\gamma F_{\theta\varphi}}{M_s \sin\theta} - \mathrm{i}\omega\right)\theta + \frac{\gamma F_{\theta\theta}}{M_s \sin\theta}\varphi = 0$$
$$\frac{\gamma F_{\theta\theta}}{M_s \sin\theta}\theta + \left(\frac{\gamma F_{\theta\varphi}}{M_s \sin\theta} + \mathrm{i}\omega\right)\varphi = 0. \quad (2.34)$$

A non-trivial solution for these equations exists only when the following condition is satisfied:

$$\omega = \frac{\gamma}{M_s \sin\theta}\sqrt{\frac{\partial^2 F}{\partial\theta^2}\cdot\frac{\partial^2 F}{\partial\varphi^2} - \left(\frac{\partial^2 F}{\partial\varphi\partial\theta}\right)^2}. \quad (2.35)$$

Thus, the uniform precession frequency is deduced by means of the partial derivatives of the free magnetic energy in terms of spherical coordinates. This frequency dispersion relationship is the theoretical basis for studying magnetic precessional motions in FMR and TRMOKE.

2.2.3 Energies of a ferromagnet

From Equation 2.35, the free magnetic energy is the key parameter in magnetisation precessional behavior in ferromagnets because it determines the effective magnetic field. The equilibrium position, where the magnetisation is oriented, is thus preferable, as this minimises the free energy. As mentioned in last section, this free magnetic energy is composed of several different contributions, and four of the most important energies will be presented in this section; these are Zeeman energy, exchange energy, static demagnetisation energy, and anisotropy energy.

2.2.3.1 Zeeman energy

Zeeman energy, also called external field energy, originates from the interactions between the magnetisation and the external field, which are considered as part of the single spin precession. Zeeman energy is expressed as [101]

$$E_Z = -\mu_0 \int_V \boldsymbol{M} \cdot \boldsymbol{H} d^3\boldsymbol{r} \,. \tag{2.36}$$

Zeeman energy is the only energy term directly determined by the external field.

2.2.3.2 Exchange energy

Arising from the Pauli exclusion principle, spin-dependent energy can be modelled as a spin-spin interaction in a vector model [102]:

$$H_{\text{Heis}} = -2 \sum_{i<j} \mathcal{J}_{ij} \boldsymbol{S_i} \cdot \boldsymbol{S_j} \,. \tag{2.37}$$

This expression is the well-known Heisenberg Hamiltonian where $\mathcal{J}_{ij}$ is the exchange integral and $\boldsymbol{S_i}$ are the spin operators. This makes it clear that the parallel alignment of the spins (ferromagnet) is energetically favourable where $\mathcal{J}_{ij} > 0$, while the antiparallel spins configuration (antiferromagnet) is favourable where $\mathcal{J}_{ij} < 0$. Because of the small spatial nature of atomic wavefunctions, the value of $\mathcal{J}_{ij}$ decreases rapidly with any increase in the distance between the atoms; thus, it is safe to consider only the nearest-neighbour pair in the Heisenberg Hamiltonian and assume the exchange interaction J is the same for each nearest-neighbour pair:

$$E_{\text{ex}} = -2 \sum_{i<j}^{nn} J \boldsymbol{S_i} \cdot \boldsymbol{S_j} \,, \tag{2.38}$$

where the exchange integral is replaced by an exchange constant, J, and the superscript nn denotes the nearest-neighbour pair.

The Hamiltonian in Equation 2.38 remains tricky to deal with, however. Considering a particular atom, i, interacting with its nearest neighbours gives

$$E_{\text{ex}}^i = -2J \boldsymbol{S_i} \cdot \sum_j \boldsymbol{S_j} \,, \tag{2.39}$$

while the Hamiltonian for the entire material is

$$E_{\text{ex}} = -\frac{1}{2} \sum_i E_{\text{ex}}^i \,. \tag{2.40}$$

Analogous to the Zeeman energy, the form of E_{ex}^{i} in Equation 2.39 can be related to the energy of a magnetic moment, μ_m, that is proportional to S_i, in an effective field, H_{eff}, which is in turn proportional to $\sum_j S_j$. Assuming the magnetic moment $\mu_m^i = g\mu_B S_i$ at site i interacts with a molecular field H_{eff} generated by the nearest-neighbour spins,

$$E_{\text{ex}}^{i} = -\mu_0 \mu_m^i \cdot H_{\text{eff}} = \mu_0 g \mu_B S_i H_{\text{eff}}, \tag{2.41}$$

where S_i is the eigenvalue of the spin operator. Comparing Equations 2.39 and 2.41, the effective field H_{eff} is derived as

$$H_{\text{eff}} = \frac{2J}{\mu_0 g \mu_B} \sum_j S_j \cong \frac{2zJ}{\mu_0 g \mu_B} \langle S_j \rangle, \tag{2.42}$$

where the sum over the neighbouring spins is replaced by z, the nearest-neighbour number, times the average spin value $\langle S_j \rangle$. Substituting the relationship $M = N_v g \mu_B \langle S_j \rangle$ into Equation 2.42 gives

$$H_{\text{eff}} = \frac{2zJ}{\mu_0 N_v g^2 {\mu_B}^2} M, \tag{2.43}$$

where N_v is the number of nearest-neighbour moments per unit volume. As with Weiss molecular field theory, the relationship between the Curie temperature, T_C, and the exchange constant, J, is thus derived as

$$J = \frac{3k_B T_C}{2zs(s+1)}, \tag{2.44}$$

where k_B is the Boltzmann constant and s is the total spin number. As T_C is proportional to J for certain values of z and s, the Curie temperature can thus be used to quantitatively represent the strength of the exchange interaction. Finally, the exchange interaction is spatially isotropic, which means that only the relative angle between spins, rather than the angle of spins with respect to a fixed direction, is of determinative importance.

2.2.3.3 Magnetostatic energy

Magnetostatic energy is also known as stray field energy, demagnetisation field

energy, or shape anisotropy energy. This energy term results from the dipole energy of the magnetised sample, that is, the energy required to assemble the atomic dipoles in the magnetised sample such that it can be treated as a macroscopic magnetic dipole. It can thus be easily understood that aligning the dipole magnets head to tail (low energy configuration) is much easier than aligning them parallel to each other (high energy configuration).

To derive this magnetostatic energy, all fields at the boundary of a sample must be considered. Assuming that the magnetisation at the end of a sample is always perpendicular to the sample surface, without any external fields applied, according to Maxwell's equations, very close to the boundary, the field inside the sample is $H_\mathrm{i} = -M_\mathrm{i}/2$, and the field outside the sample is $H_\mathrm{o} = M_\mathrm{i}/2$. Therefore, the flux densities are $B_\mathrm{i} = \mu_0(H_\mathrm{i} + M_\mathrm{i}) = \mu_0 M_\mathrm{i}/2$ inside the sample and $B_\mathrm{o} = \mu_0(H_\mathrm{o} + M_\mathrm{o}) = \mu_0 M_\mathrm{i}/2$, with $M_\mathrm{o} = 0$ outside the sample. Where the value of the flux densities B are the same, this shows continuity at the surface boundary. When an external field is applied, the existing fields at the boundary of a sample are [102]

$$H_\mathrm{o} = H_\mathrm{appl} + M_\mathrm{i}/2$$
$$H_\mathrm{i} = H_\mathrm{appl} - M_\mathrm{i}/2\,. \tag{2.45}$$

Thus, the field inside the magnetic sample becomes equal to the applied field reduced by the field generated by magnetisation inside the sample; this is called the demagnetising field H_d. In general, the demagnetising field originates from the poles at the sample surface opposing the magnetising field; thus, the internal field that the magnetisation responds to is reduced. In such cases, the demagnetising field is also known as the surface pole field or dipole field. The internal field in the sample can be simply treated as

$$H_\mathrm{i} = H_\mathrm{appl} + H_\mathrm{d}. \tag{2.46}$$

If the sample is a very thin film, the demagnetising field in Equation 2.45 must be modified to include contributions from both top and bottom surfaces. The assumption that the magnetisation is normal to the surface is not always valid, however, so a more general expression of the demagnetising field is given as $H_\mathrm{d} = -\boldsymbol{M}\cdot\boldsymbol{n}$, where $\boldsymbol{n}$ is

the surface normal. For a sample with an arbitrary shape, the demagnetising field is thus approximated as

$$H_{\mathrm{d}} = -N_{\mathrm{d}} M, \tag{2.47}$$

while the magnetisation orientation is given relative to the sample axes. The constant N_{d} is the demagnetisation factor, which can be measured or estimated fairly well for most shapes of sample; for magnetic thin films, $N_{\mathrm{d}} = 1$.

Therefore, the magnetostatic energy can be derived as

$$E_{\mathrm{dem}} = -\frac{\mu_0}{2} \boldsymbol{M} \cdot \boldsymbol{H}_{\mathbf{d}}. \tag{2.48}$$

The magnetostatic energy can be understood as the work done in assembling a given state of magnetisation in a sample; the factor of $1/2$ is introduced because dipole pair interactions must not be counted twice.

2.2.3.4 Magnetic anisotropy energy

In a magnetic material, if the magnetic properties are a function of the direction of the magnetisation with respect to the structural axes, this is known as direction-dependence magnetic anisotropy. Typically, the anisotropic magnetic properties can be easily deducted from the hysteresis loops measured along various directions of a sample. This is of considerable practical interest because anisotropy can be, and has been, exploited in the design of many magnetic materials of commercial importance. There are several different types of anisotropy, all of which can contribute to the free magnetic energy; these include magnetocrystalline anisotropy, shape anisotropy, magnetoelastic anisotropy, and surface anisotropy. Shape anisotropy, originating from the demagnetising field and demagnetisation energy, was presented in the previous section. Magnetoelastic anisotropy relies on the stresses applied on a sample, which is out of scope in the current experiments. Surface anisotropy is a general concept that includes all the anisotropies from a surface, despite the differences in their mechanisms. A typical surface anisotropy in Fe ultrathin films will, however, be presented in chapter 4. Magnetocrystalline anisotropy is the most common type of anisotropy, and it is the only

intrinsic anisotropy determined by the microscopic structure of the sample; by implication, this means that all other types of anisotropies are extrinsic or induced. Thus, the attention of this work focused on magnetocrystalline anisotropy [101].

The underling physical origin of magnetocrystalline anisotropy is for the coupling between the magnetic moment and the lattice. The succinct version of this is that the magnetocrystalline anisotropy is attributed to spin-orbit coupling as well as the crystalline electric field. In atomic physics, the coupling between the electron spin and the electronic orbital shape is known as spin-orbit coupling. It supplies a direct channel between the spin and the lattice as an electron orbits around the atomic nucleus with a given angular momentum. Meanwhile, if the crystalline electric field that results from the chemical bonding of the orbitals on a given atom with their local environment is of low symmetry, molecular orbitals or bonding electron charge distributions will be energetically preferred in certain orientations. Thus, the anisotropic crystalline electric field drives the orbital moments in a certain orientation and consequently determines the orientation of the spin via spin-orbit coupling.

Following the microscopic interpretation of magnetic anisotropy, two main specific types of anisotropy will be presented. The most common anisotropy effect is connected to the existence of a single easy direction, and this is referred to as uniaxial anisotropy. The anisotropy free energy density is expressed as [102]

$$E_{\mathrm{u}} = K_{\mathrm{u0}} + K_{\mathrm{u1}} \sin^2 \theta + K_{\mathrm{u2}} \sin^4 \theta + \cdots \tag{2.49}$$

where θ is the orientation of magnetisation with respect to the easy axis, and K_{u0}, K_{u1}, K_{u2},…, are the anisotropy constants.

Another case of magnetic anisotropy is cubic anisotropy, where the anisotropy energy density has cubic symmetry. There are three orthogonal privileged directions (easy axes) and the expression of the free energy is thus

$$E_{\mathrm{a}} = K_0 + K_1(\alpha_1^2\alpha_2^2 + \alpha_2^2\alpha_3^2 + \alpha_3^2\alpha_1^2) + K_2(\alpha_1^2\alpha_2^2\alpha_3^2), \tag{2.50}$$

where the α is the direction of the cosines of the magnetisation along the three coordinate axes. In a thin film such as Fe thin film, cubic anisotropy will be presented as in-plane four-folder symmetry with two orthogonal in-plane easy axis.

2.2.4 Kittel formula

As presented in Section 1.2, in all-optical pump-probe measurements, although the magnetisation precession is induced by an ultrafast change of the anisotropy and the magnetisation, the precession frequency is determined by the effective magnetic field, as in ferromagnetic resonance. According to Equation 2.35, given the free magnetic energy, the precession frequency will thus be determined in a specific geometry. Conversely, if the precession frequency is obtained experimentally as a function of the applied field amplitude/orientation, the magnetic parameters can be determined or estimated by fitting the dispersion relationship. Starting with the simplest case, only considering the Zeeman energy and the demagnetisation field energy to represent the free energy; the frequency of the uniform precession can then be derived specifically.

In the spherical coordinates shown in Figure 2.4, if the angle φ of the magnetisation is fixed along with the applied field, the geometry will be simplified, as in the case shown in Figure 1.3(a). An external field is applied with an angle θ_H with respect to surface normal, which determines the equilibrium orientation of the magnetisation θ. Considering only the Zeeman energy and the demagnetisation field energy, the free magnetic energy F can thus be expressed in cgs units as

$$F = 2\pi M_s^2 \cos^2\theta - M_s H[\sin\theta_H \sin\theta + \cos(\theta_H - \theta)]. \tag{2.51}$$

The equilibrium orientation of the magnetisation can be derived by using [103]

$$\frac{\partial F}{\partial \theta} = 0. \tag{2.52}$$

Using Equation 2.51, θ is determined by solving the following equation numerically:

$$\sin(2\theta) = (2H/4\pi M_s)\sin(\theta - \theta_H). \tag{2.53}$$

By deducing the partial derivatives which contribute to the precession frequency in Equation 2.35, the following set of equations is obtained [103, 104]:

$$\left(\frac{\omega}{\gamma}\right)^2 = H_1 \cdot H_2, \tag{2.54}$$

$$H_1 = H\cos(\theta_H - \theta) - 4\pi M_s \cos^2\theta, \tag{2.55}$$

$$H_2 = H\cos(\theta_H - \theta) - 4\pi M_s \cos 2\theta. \tag{2.56}$$

The frequency dispersion relationship in the uniform precession within the entire

sample is given by Equation 2.54, which is known as the Kittel formula. This is the simplest case, and does not consider any contribution from anisotropy energy terms. The anisotropy energy can, however, be added into the free magnetic energy and Equations 2.53 to 2.56 can be re-calculated correspondingly if required. Experimentally, the frequency dispersion relation can be fitted by systematically varying the applied field amplitude or orientation to obtain the value of the anisotropy constants.

2.3 Derivation of Gilbert damping

In magnetisation precession, as well as defining the frequency dispersion relationship, another important parameter needed to be determined is the dimensionless Gilbert damping constant, α. In FMR, as the resonance amplitude is measured in the frequency domain, the Gilbert damping can be obtained from the linewidth of the FMR spectra. In time-resolved measurements, however, the signature of the Gilbert damping is directly in the precession decay time, τ. The relationship between the damping parameter α and the precession decay time τ can be derived from the linearized LLG equation, given a corresponding effective magnetic field H_{eff}.

Assuming that the magnetisation is aligned along the x-direction and a very small perturbation is applied to trigger the magnetisation precession, during the precession $M_{\mathrm{y}}, M_{\mathrm{z}} \ll M_{\mathrm{x}} \cong M_{\mathrm{s}}$. In this case, the LLG equation, Equation 2.25, can be re-written as three components [97, 100]:

$$\begin{aligned} \dot{M}_{\mathrm{x}} &= 0, \\ \dot{M}_{\mathrm{y}} &= -\gamma_0\left(M_{\mathrm{z}}H_{\mathrm{eff,x}} - M_{\mathrm{s}}H_{\mathrm{eff,z}}\right) - \alpha\dot{M}_{\mathrm{z}}, \\ \dot{M}_{\mathrm{z}} &= -\gamma_0\left(M_{\mathrm{s}}H_{\mathrm{eff,y}} - M_{\mathrm{y}}H_{\mathrm{eff,x}}\right) + \alpha\dot{M}_{\mathrm{y}}. \end{aligned} \tag{2.57}$$

where $H_{\mathrm{eff,i}}$ donates the i-component of the effective magnetic field H_{eff}, and the x-component of the magnetisation, M_{x}, is treated as a constant of the saturation magnetisation M_{s}. To solve these partial derivative equations, the effective field must be explicitly known. This can be derived from the free magnetic energy F by means

of the equation

$$\boldsymbol{H}_{\text{eff}} = -\frac{1}{\mu_0 M_{\text{s}}}\frac{\partial F}{\partial \boldsymbol{m}}, \tag{2.58}$$

where $\boldsymbol{m} = (\boldsymbol{m_{\text{x}}},\ \boldsymbol{m_{\text{y}}},\ \boldsymbol{m_{\text{z}}})$, the magnetisation unit vector, and the magnetisation $\boldsymbol{M}$ is equal to $M_{\text{x}}\boldsymbol{m_{\text{x}}} + M_{\text{y}}\boldsymbol{m_{\text{y}}} + M_{\text{s}}\boldsymbol{m_{\text{z}}}$. Re-writing the expression for the free magnetic energy in Equation 2.51 in Cartesian coordinates gives (SI units)

$$F = -\mu_0\left(H_{\text{x}}M_{\text{x}} + H_{\text{y}}M_{\text{y}} + H_z M_{\text{z}}\right) + \frac{1}{2}\mu_0 M_{\text{z}}^2, \tag{2.59}$$

where H_{i} denotes the i-component of the external field. Combining Equation 2.58 and Equation 2.59, the effective field can be derived:

$$\boldsymbol{H}_{\text{eff}} = H_{\text{x}}\boldsymbol{m_{\text{x}}} + H_{\text{y}}\boldsymbol{m_{\text{y}}} + (H_z - M_{\text{z}})\boldsymbol{m_{\text{z}}}. \tag{2.60}$$

Substituting the effective field into Equation 2.57, the equations of motion for M_{y} and M_{z} are derived:

$$\dot{M}_{\text{y}} = \gamma_0 M_{\text{s}} H_{\text{z}} - \gamma_0 (H_{\text{x}} + M_{\text{s}}) M_{\text{z}} - \alpha \dot{M}_{\text{z}}, \tag{2.61}$$

$$\dot{M}_{\text{z}} = \gamma_0 H_{\text{x}} M_{\text{y}} + \alpha \dot{M}_{\text{y}}. \tag{2.62}$$

These coupled linear differential equations must be solved for continuous functions, derivatives of higher orders, and a solution for one of the variables. The higher order derivatives of Equations 2.61 and 2.62 are calculated as

$$\ddot{M}_{\text{y}} = -\gamma_0 (H_{\text{x}} + M_{\text{s}}) \dot{M}_{\text{z}} - \alpha \ddot{M}_{\text{z}}, \tag{2.63}$$

$$\ddot{M}_{\text{z}} = \gamma_0 H_{\text{x}} \dot{M}_{\text{y}} + \alpha \ddot{M}_{\text{y}}. \tag{2.64}$$

Combining Equations 2.61 to 2.64, with only the equation of motion for the y-component considered, gives

$$(1 + \alpha^2)\ddot{M}_{\text{y}} + \alpha\gamma_0 (2H_{\text{x}} + M_{\text{s}})\dot{M}_{\text{y}} + \gamma_0^2 (H_{\text{x}} + M_{\text{s}}) H_{\text{x}} M_{\text{y}} = 0. \tag{2.65}$$

The assumed solution for this equation is thus given by

$$M_{\text{y}} = M_{\text{y}}^0 \exp(-i\omega t) e^{-t/\tau}, \tag{2.66}$$

where ω is the angular frequency of the magnetisation precession and τ is the exponential decay time, as mentioned. The imaginary part of the left hand side of Equation 2.66 must to be zero and the relationship is thus

$$(\alpha^2 + 1)\frac{2i\omega}{\tau} - i\omega\alpha\gamma_0(2H_x + M_s) = 0. \quad (2.67)$$

From the quadratic Equation 2.67, the solution for the damping constant can thus be derived:

$$\alpha = \frac{1}{2}\left(\frac{\tau\gamma_0(2H_x + M_s)}{2} \pm \sqrt{\left(\frac{\tau\gamma_0(2H_x + M_s)}{2}\right)^2 - 4}\right). \quad (2.68)$$

The solution with a plus sign is impossible, as α would be much larger than 1 in such a case, indicating an overdamped precession, which is not the observed case in most magnetic materials. Thus, the only solution is the one with the minus sign, and as $\left(\frac{\tau\gamma_0(2H_x+M_s)}{2}\right)^2$ is much larger than 4, the damping parameter can be determined by

$$\alpha = [\tau\gamma_0(H_x + M_s/2)]^{-1}. \quad (2.69)$$

At the limit of high external fields, $H_x \gg M_s/2$, the precession frequency will be the same as the Larmor frequency, $\omega = \gamma_0 H$, and the damping parameter is thus simply inversely dependent on the product of the decay time and the precession frequency

$$\alpha = (\tau\omega)^{-1}. \quad (2.70)$$

In fact, the derivation of the damping parameter must include the anisotropy energy's contribution to the free magnetic energy. Nevertheless, Equation 2.70 is always valid in high field limits, and this is why a large enough external field is of importance in experimental work.

2.4 Theoretical descriptions of damping

As introduced in chapter 1, the magnetic damping has the intrinsic and extrinsic contributions. In this section, theoretical descriptions of these contributions will be presented [45].

2.4.1 Intrinsic damping

The essential mechanism of the intrinsic damping is the spin-orbit coupling (SOC) causing spin-mixing, which means the single spin will no longer stay at the static eigenstates of spin up or spin down [71]. This coupling between the electron spin- and the orbital- angular momenta provides a the link between the precessing electrons and the lattice, which means without SOC the uniform precession would not be damped and the LLG equation will replaced by the LL equation [71, 78, 80, 105].

Theoretically, Kambersky made some significant works on modelling the intrinsic damping in ferromagnetic materials [65, 86, 106]. He used a torque, arising from the SOC, to derive the Hamiltonian of a single electron. Because the main intrinsic energy dissipation to the lattice is via SOC and electron-hole recombination, Kambersky's works focus on the variation at the Fermi energy level. The damping arising from the changes to the Fermi level have two contributions. One is the addition of many small effects across the whole Fermi level, and the other is the larger contributions from the so-called 'special regions' [64]. This 'special regions' is also called 'hot regions' in k-space where pairs of eigenstates with energies close to the Fermi surface occur, arising from degenerate band-crossing at the Fermi level which is modified by the spin-orbit coupling [73].

This Kambersky model is similar to that of Sparks [78], involving the annihilation of uniform mode magnons, in the microscopic view of the electronic interactions. Electron-hole pairs, generated during the annihilation process, scatter to dissipate the energy from these excited states to the lattice [62, 68, 73, 107]. The damping is determined by transitions into states close to the Fermi level because the total angular momentum is not conserved due to non-spin-flip collisions. There are two types of electronic transitions accounting to the damping: magnon annihilation or electron-hole pairs generation can occupy the same band (intraband) of different bands (interband). The damping associated with the these transitions was described as 'conductivity-like' or 'resistivity-like' [108, 109] by analogy with the temperature dependence of the electronic transition phenomena. The damping form intraband term decreases with

increasing temperature and hence is termed ‘conductivity-like’ while the ‘resistivity-like’ damping from interband term increases with increasing temperature [65, 73, 106, 110, 111]. Therefore, the intrinsic damping is correlated with the density of states (DOS) and the spin-orbit coupling in both intraband and interband processes plays a key role.

2.4.2 Interfacial and spin pumping contributions to intrinsic damping

In multi-layered systems, the presence of sharp interfaces could result in an increase in the localization of the interaction between magnons and the conduction electrons [67], which may enhance the damping because of the different momentum between the spin-up and spin-down states at the Fermi surface. The spin-flip process allows electrons to cross the momentum gap as the interface acts as a momentum source, which modify the Gilbert damping in magnetic multilayer system [67, 72]. To conserve the angular momentum, each magnon creation or annihilation event has to be combined with a conduction electron spin-flip event [110, 112]. The enhancement of the Gilbert damping in epitaxial Fe thin films are successfully explained by this theoretical approach [70]. The total Gilbert damping constant is given by

$$\alpha = \frac{D_{\mathrm{t}} B_{\uparrow\downarrow}\, \hbar/8}{\tau_{\mathrm{sf}} B_{\uparrow\downarrow}\, n_{\mathrm{m}}/2 + 1}. \tag{2.71}$$

Where $B_{\uparrow\downarrow}$ is the surface electron-magnon coupling parameter which describes the interfacial spin-flip rate, D_{t} is the total conduction electron DOS, and τ_{sf} is the spin relaxation time. n_{m} is the number of magnons in the ferromagnetic layer, which is given by

$$n_{\mathrm{m}} = S_2 n_2 (1 - \cos\theta), \tag{2.72}$$

where n_2 is the number of the localized magnetic spin S_2 in the ferromagnetic layer and θ is the precession cone angle.

Besides the direct modification of damping at the interface, another mechanism for relaxation is the spin-pumping, which propagate and dissipate the spin current through the interface from the FM layer to the NM layer [112]. A d.c. current crossing the

interface, stimulating spin wave emission was introduced earlier by Berger [72]. The spin-pumping effect pumps the spin angular momentum adiabatically form the FM into the NM metal, leading to an enhancement of the damping. The reflectivity and transmissivity of interface will determine the flow of spin as well as the efficacy of spin pumping process. Therefore, the electronic structure at the interface is crucial for the spin pumping. Electrons in the conduction band coupled with the exchange split d-band allows the spin transport from the FM to NM layer through the interface [112]. the transferred spin current is then dissipated via SOC or spin-flip as described in the intrinsic mechanism. The spin-orbit and spin-flip mechanisms in the NM layer, which is defined as the spin sink, determines the diffusion of the pumped spin-current into the NM layer. If the spin-current is not dissipated fully the spin will be accumulated in the NM layer of return to the FM layer via some spin-current [72, 112]. The spin diffusion length (λ_{sf}) and the interface atomic intermixing between the adjacent layers through the effective spin-mixing conductance ($g_{eff}^{\uparrow\downarrow}$) determine the spin-current and the spin diffusion. The enhancement of the Gilbert damping is also related to the atomic number of the NM material and the spin-relaxation rate [73, 112, 113].

2.4.3 Extrinsic damping

The extrinsic damping contributions are associated with the magnetic inhomogeneities in a ferromagnetic system. Many factors, i.e. impurities, non-uniformity of the sample surface, lattice mismatches-induced strain, and sample thickness can result in the microscopic crystalline variations such as point- and line-defects [74, 79]. The magnetic properties may be linked to the local variations of the structural effects, such as magnetization and anisotropies. When the inhomogeneities is small, the magnetization tends to precess almost uniformly, but prefer to precess in a number of local resonant modes when the density of inhomogeneities is higher [79, 80, 114].

The interaction between the uniform precession and non-uniform resonance modes

is the so-called 'two-magnon scattering'. The local magnetic property variations induced by the magnetic inhomogeneities in ferromagnetic system will enhance the magnetic damping and thereby broaden the measured ferromagnetic resonance response [68, 77, 80]. The exchange interaction will force magnetic moments to align parallel on short length-scales while the moments will interact via the dipole interaction over longer distances. Coupled with anisotropy term, the combination of these mechanisms will format uniformly magnetized domains, separated by domain walls. Within a single domain, the magnetization always precesses uniformly and the energy loss is intrinsic. In multiple magnetic domains, however, the precession is affected by each domains and additional magnon modes are excited, leading to the extrinsic two magnon scattering.

To describe the two-magnon scattering, a theoretical Bloch-Bloembergen (BB) equation [115, 116] is given by

$$\frac{\partial \boldsymbol{M}}{\partial \mathrm{t}} = -\gamma(\boldsymbol{M} \times \boldsymbol{H}_{\mathrm{eff}}) - \frac{M_x}{T_2}\hat{e}_x - \frac{M_y}{T_2}\hat{e}_y - \frac{M_x - M}{T_1}\hat{e}_z, \tag{2.73}$$

based on two energy dissipation channels to the thermal bath of the lattice. Here $\hat{e}_{x,y,z}$ are unit vectors, T_1 the longitudinal (spin-lattice in NMR) relaxation time via the uniform mode and T_2 the transverse (spin-spin) relaxation time via the non-uniform mode. Now we can compare the linewidth derived from the LLG equation with that from the BB equation. For the LLG equation, the linewidth only comes from the intrinsic damping which is given by [68, 117, 118]

$$\Delta H_{\mathrm{LLG}}(\omega) = \frac{2}{\sqrt{3}}\frac{G}{\gamma^2 M}\frac{\omega}{\cos\beta}, \tag{2.74}$$

where β is the angle between the equilibrium magnetization vector and the applied field. The linewidth given by the BB equation due to the transvers relaxation, corresponding to the extrinsic damping from the effect of two-magnon scattering, is [68, 119]

$$\Delta H_{\mathrm{BB}}(\omega) = \frac{\partial H_{\mathrm{Res}}}{\partial \omega_0}\frac{1}{T_2}, \tag{2.75}$$

Where H_{Res} is the applied magnetic field at resonance, and $\partial H_{\mathrm{Res}}/\partial\omega_0$ may be obtained from the suitable version of the Kittel formula.

The underling mechanism of the two-magnon process is quite complicated due to its correlation with structural defects and inhomogeneities. Therefore, the measured linewidth in FMR has to be interpreted in relation to the linewidth broadening and the potential energy dissipation channels in the system. It is generally believed that intrinsic and extrinsic damping contributions may be distinguished by various means. However, it is suggested that the inhomogeneities increase both two-magnon scattering effects and coupling between magnetization and the lattice vibration, which means both the intrinsic and extrinsic damping are increased by the inhomogeneities [79]. Also a theoretical work on multilayer and bilayer thin films shows that the interaction between the spin waves and the itinerant electrons can be increased by interface. Both intrinsic and extrinsic damping can be enhanced because the interaction is not limited to the uniform mode but also applies to the non-uniform magnon modes [72, 113].

2.5 Spin waves

Thus far, only uniform magnetisation precession has been discussed. All the spins throughout the sample are treated as macrospin and they are uniformly stimulated to precess under the action of a uniform effective field. In such cases, the LLG equation used to describe the spin dynamics acts only as a function of time, and no spatial distribution of the spins is considered. However, if the effective field is no longer uniform through the sample but has a distribution, the LLG equation will exist in a non-local form:

$$\frac{\mathrm{d}\boldsymbol{M}(\boldsymbol{r},t)}{\mathrm{dt}} = -\gamma_0\big(\boldsymbol{M}(\boldsymbol{r},t)\times\boldsymbol{H}_{\mathrm{eff}}(\boldsymbol{r})\big) + \frac{\alpha}{M_s}\left(\boldsymbol{M}(\boldsymbol{r},t)\times\frac{\mathrm{d}\boldsymbol{M}(\boldsymbol{r},t)}{\mathrm{dt}}\right). \tag{2.76}$$

Experimentally, if a local perturbation is applied to the magnetisation, a propagating magnetic excitation will be generated in the non-uniform spin system, and this is called a spin wave. In a simplified one-dimensional spin system as shown in Fig. 2.6, it can be seen that the motion of the individual spins is in phase during the uniform precession (Fig. 2.6(a)) and out-phase in a spin wave, although the precession frequency of each

spin remains the same (Fig. 2.6(b)). Spin waves can also be stimulated by a uniform perturbation if there is an implicit phase difference from the start. A dispersion in many factors such as the effective magnetic fields, sample morphology, magnetic domain structure, and magnetic anisotropy, can also introduce a non-uniform initial orientation of the spins. Finally, if the precession frequency varies in space due to, for example, magnon scattering, then the spins will diphase after a finite time, even if a uniform precession exists initially [120].

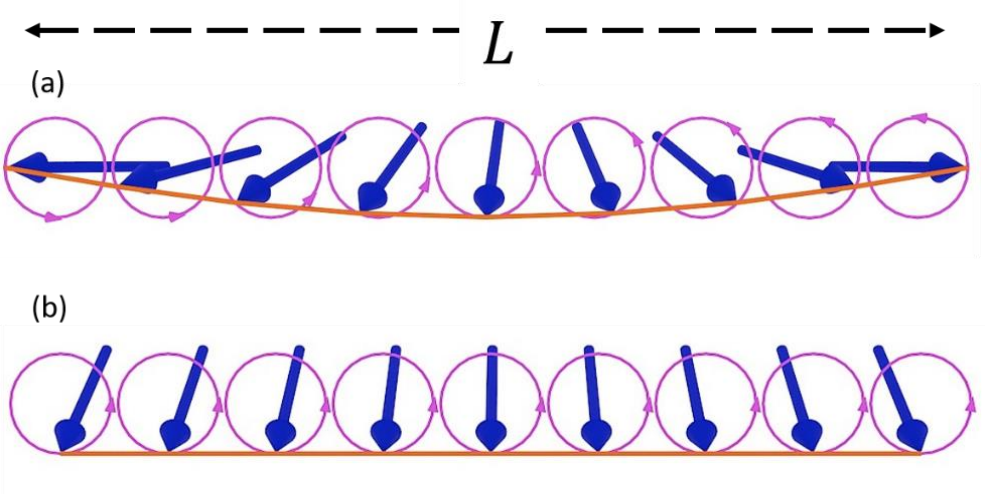

Figure 2.6: Schematic illustration of (a) a perpendicular standing spin wave ($\boldsymbol{k} \neq 0$) and (b) the uniform precession mode ($\boldsymbol{k} = 0$). L is the thickness of the film.

The spin wave can be represented by a plane wave of $\exp\left(-i(\omega t - \boldsymbol{k} \cdot \boldsymbol{r})\right)$ at position $\boldsymbol{r}$ with the wave vector $\boldsymbol{k}$. When the wave vector $\boldsymbol{k} = 0$, the plane wave will be only time-dependent, and this corresponds to the uniform precession mode. Different combinations of the directions of the wave vector and the magnetisation determine the different types of spin waves, which include Damon-Eschback mode [121], magnetostatic backward volume mode , and magnetostatic forward volume mode [97]. A spin wave traveling perpendicular to the sample surface, which is called the perpendicular standing spin wave, plays an important role in all-optical pump-probe experiments. As the penetration depth of light in metals has a range of only 10 to 20 nm, magnetisation in a thin film sample with a thickness larger than the penetration depth will be non-uniformly perturbed with respect to the z-direction.

Additional laser intensity is absorbed in the region closest to the surface, and this absorption decays as the light penetrates further. In such cases, a dispersion in the initial perturbation is realised in the z-direction, resulting in a perpendicular standing spin wave. The thickness of the sample is the key to defining the perpendicular standing spin wave, as in a very thin (sub-nanometre) sample, it is very difficult to realise a phase difference between the spins along the z-direction. On the other hand, according to the expression of the frequency of the first-order (k=π/L, where L is the thickness), the standing spin wave $\omega_1 = \omega_0 + D(\pi/L)^2$, where ω_0 is the frequency of the uniform mode and D is the exchange stiffness constant [52], and the frequency difference between the spin wave and uniform mode will be too small to distinguish for greater thicknesses. Therefore, establishing a proper thickness for the sample is the key to observing the perpendicular standing spin wave. As in the pump-probe measurements shown in Fig. 2.7, the observed transient Kerr signal may look chaotic at first glance if a perpendicular standing spin wave exists. However, this time-resolved signal is a superposition of the uniform mode and the spin wave mode, and these can be separately recognised by fitting a combination of two damped sinusoid functions. It is noting that this first order mode cannot be detected using microwave FMR, as a nonzero net change of the magnetic moment over the entire volume of the sample is necessary for FMR measurements.

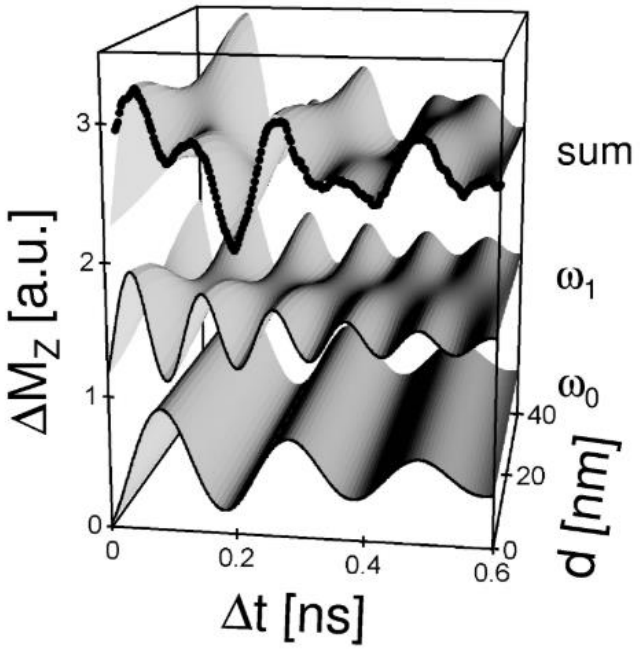

Figure 2.7: Observation of the uniform precession mode (ω_0) and the first-order perpendicular standing spin wave (ω_1). The sum curve is the measured transient magnetisation change as seen using a pump-probe technique [52].

Chapter 3 Experimental Techniques

3.1 Introduction

Development over the past few decades in experimental methods to explore both static and dynamic magnetic properties have led to a rich range of experimental techniques. To measure the static magnetic properties of a sample in external magnetic fields, several sensitive techniques are available, including the Superconducting Quantum Interference Device (SQUID), Vibrating Sample Magnetometer (VSM), and the Alternating Gradient Force Magnetometer (AGFM). Static MOKE, either Polar or Longitudinal MOKE, is also a very powerful method used to measure the hysteresis loop of a magnetic sample. A simple MOKE setup only requires a few optics and a photodiode detector, making it possible to implement *in-situ* measurements in certain cases [122]. Furthermore, it has been demonstrated that the sensitivity of MOKE is very high, allowing measurement of the magnetisation of practically monolayer iron [123].

Nevertheless, traditional methods, especially SQUID and VSM, are still very powerful, particularly in terms of obtaining accurate values for the magnetic parameters, such as saturation magnetisation, saturation field, and coercive field. Before implementing advanced experiments on a magnetic sample, it is always necessary to measure static hysteresis loops, and thus a brief introduction to SQUID and VSM will be given in section 3.1.1 of this chapter.

Many other methods help with the study of local magnetic properties of materials on the microscopic/nanoscopic scales. These techniques are usually used to map the magnetic domains of sub-micrometre size and to detect magnetic domain walls and their movements driven by spin-polarised currents or magnetic fields. These techniques include magneto-optic (Kerr or Faraday) microscopy, magnetic force microscopy (MFM), scanning Hall microscopy, and Lorentz transmission electron microscopy (TEM). Even using a home-made wide field magnetic Kerr microscope, the magnetic domain structure and its motion can be clearly observed, as shown in Fig. 3.1, for example:

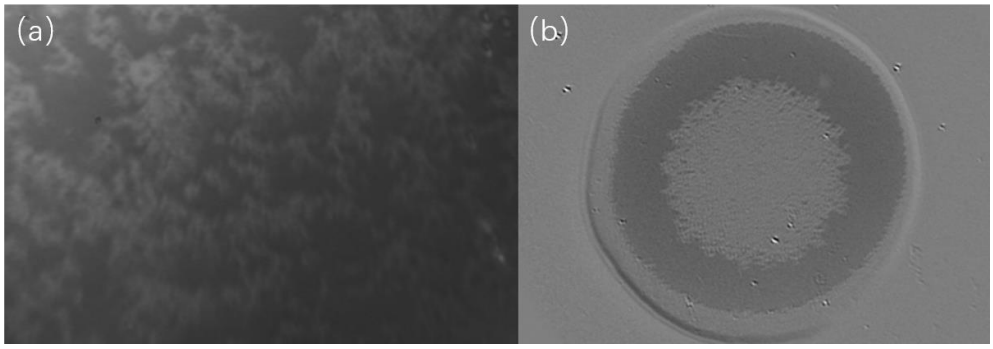

Figure 3.1: magnetic domain structures in TbFeCo thin film (a) and TbFeCo dot (b) obtained by wide field magnetic Kerr microscope. The diameter of the TbFeCo dot is 300 μm. The length scale in (a) can refer to (b).

In terms of probing magnetisation dynamics, there are groups of techniques. One group is working in frequency domains such as ferromagnetic resonance (FMR) and Brillouin light scattering (BLS). The other working in time domains employing pump-probe technique such as TRMOKE, which is the central experimental technique used in this thesis. The two groups of methods are complementary, and in this thesis methods

used in spectroscopic measurements, particularly FMR, were adopted in order to analyse the TRMOKE experimental data. Therefore, a brief introduction to FMR and BLS will be given in section 3.1.2 of this chapter.

3.1.1 VSM and SQUID

A vibrating sample magnetometer (VSM) is a common instrument used to measure magnetic hysteresis loops of a magnetic sample. A basic diagram of a VSM is shown in Fig. 3.1. The sample is mounted on a non-magnetic rod and oscillated or vibrated at the geometrical centre of the air gap between two pairs of fixed coils. An electromagnet is used to magnetize the sample in a certain orientation. The magnetic moment of the vibrating sample produces a changing magnetic flux in the coils. The coil pairs are connected in such a way that the signal due to the moving sample adds, and any signal due to fluctuations in the field from the electromagnet subtracts ideally cancels. Due to the very small value of the signal, a lock-in amplifier is always used to detect the signal at the vibrating frequency so as to increase the signal-to-noise ratio [124-126].

The model of the VSM used in York is the ADE (now MicroSense) model 10 VSM, which has high sensitivity ($< 0.1\mu emu$) and high maximum magnetic field of up to about 2.2 T. The electromagnet can rotate in the horizontal plane, and the sample can thus be put in the horizontal or vertical plane by changing the rod to obtain; hysteresis loop along any orientation. This equipment can also measure the temperature dependent hysteresis loop with a temperature range from 77 to 773 K.

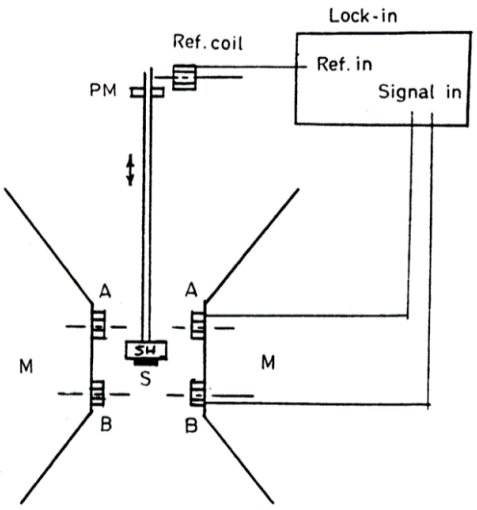

Figure 3.2: Schematical diagram of a VSM. PM=permanent magnet; SH=sample holder; M, M=electromagnet pole pieces; A, A-detection coils connected series aiding; B, B-detection coils connected series aiding but opposing A, A [127].

A Superconducting Quantum Interference Device (SQUID) VSM has a much higher sensitivity compared to conventional VSM. In any SQUID based measuring instrument, the signal of interest is coupled to the SQUID by a superconducting flux transformer that consists of a pick-up loop and an input coil that are tightly coupled to the SQUID. Due to flux quantization in superconducting rings, any change in magnetic flux through the pick-up loop due to the signal of interest will result in a flow of screening current in the flux transformer coupling magnetic flux through the SQUID loop; the SQUID then responds by generating a proportional output voltage. In a conventional SQUID magnetometer, the sample is repeatedly transported across a superconducting pick-up loop in the form of a first or second order gradiometer, and the SQUID output voltage is recorded as a function of sample position in the form of a flux profile. The magnetisation of the sample is inferred by fitting the measured flux profile to that expected for a point dipole. As a full flux profile must be recorded at each value of T and H, measurements over an extended range of T and H tend to take a long time, however. A conventional VSM measures the voltage induced in a pick-up loop using Faraday's law of induction as the sample is vibrated in its vicinity, making its measurements relatively quicker, although offering slightly poorer sensitivity to that offered by a conventional SQUID magnetometer. In a SQUID VSM, the sample is fixed

at the point where the slope of the flux profile is maximised and is vibrated about this mean position at a low frequency while the SQUID output is recorded as a function of temperature. As the full flux profile does not have to be recorded, measurements over an extended range of T and H can be completed in a relatively short period of time using a SQUID VSM compared to a conventional SQUID magnetometer. SQUID VSM thus combines the high sensitivity of SQUID with high speed of measurement of a conventional VSM.

The model of SQUID VSM used in Nanjing University is Quantum Design's MPMS 3. This machine's very high sensitivity of $\sim 10^{-8}$ emu makes it easier to use for measuring samples with low magnetisation. Using liquid helium, the temperature range stretches from 1.8 to 400 K, and the maximum magnetic field can be up to 7 T.

3.1.2 FMR and BLS

Magnetisation precession was discussed broadly in chapter 2. The implications are that at a static equilibrium state, magnetisation is determined by the effective field, $\boldsymbol{H}_{\mathrm{eff}}$, which receives contributions from exchange, anisotropy, dipolar fields, and the external field. To introduce precession of the magnetisation around its equilibrium position, the magnetisation must therefore be perturbated, which refers to the process of tilting the magnetisation at a small angle away from its equilibrium position. In ferromagnetic resonance, a weak microwave pumping field, $\boldsymbol{H}_{\mathrm{rf}}$, is applied, and a small perturbative torque, $\boldsymbol{M} \times \boldsymbol{H}_{\mathrm{rf}}$, thus exerted to tilt the magnetisation. In consequence, the local effective field will exert a restoring torque, $\boldsymbol{M} \times \boldsymbol{H}_{\mathrm{eff}}$. At that point, the magnetisation responds by adding a precessional motion to the restoring force. The magnetisation eventually spirals in after a perturbation towards its equilibrium position, due to magnetic damping; to maintain the precessional motion, the magnetisation thus has to be continuously perturbated by the pumping field. When the frequency of the pumping field is the same as the eigenfrequency of the precession, resonance absorption is obtained [128-132].

Brillouin light scattering (BLS) [133] involves scattering photons from thermally

excited traveling spin waves of wave vector $\boldsymbol{k}$ and energy E. The spin wave of wave vector $\boldsymbol{k}$ can be created or annihilated because energy and momentum conservation hold in the overall scattering process. This is in contrast to FMR excitations, in which no momentum is transferred and only modes are excited for, meaning that the total momentum is zero, $\boldsymbol{k} = 0$. In consequence, as well as the uniform FMR mode ($\boldsymbol{k} = 0$), finite wavelength modes with modulus $\boldsymbol{k} \neq 0$ can be excited in BLS. Modes such as standing spinwaves or Damon-Eshbach modes could be excited.

However, as FMR and BLS both work in the frequency domain, information on damping can only be indirectly obtained from any broadening of the absorption lines. Moreover, conventional FMR methods using commercially available connectors, waveguides, and cabling are generally limited in frequency range up to tens of gigahertz. For higher frequency electric circuits, the usage of waveguides and connectors suffer significant losses. Thus, the use of time resolved magneto-optical Kerr effect (TRMOKE) has many advantages. It measures the magnetisation response by means of a time-delayed laser pulse in the time domain after a field or laser pulse stimulation, allowing information on magnetisation dynamics to be accessed directly. The application of field pulses requires lithographically defined structures on the sample, and the pulse width is limited in the picoseconds time scale [59]. The all-optical method focuses and overlaps two ultrafast laser pulses at a sample surface to “kick” and probe the magnetisation. Compared to FMR, all-optical TRMOKE is more flexible, higher sensitivity and the frequency bandwidth is extended to the terahertz region. More importantly, TRMOKE can detect spin wave modes ($\boldsymbol{k} \neq 0$) as well as the uniform FMR mode ($\boldsymbol{k} = 0$), and can locally measure a very small area depending on the beam size of the probe laser beam, making it possible to both map a large sample and detect small devices. These advantages make all-optical TRMOKE a popular choice for investigating magnetisation dynamics.

3.2 MOKE signal detection

As discussed in chapter 2, after the interaction with the magnetic material surface, the polarisation of the incident linearly polarised light will rotate a very small angle which is known as the Kerr rotation. The reflected light also becomes elliptically polarised. To detect the Kerr rotation despite its small extent, one of the simplest methods is to use a pair of polarisers. The first polariser, denoted by "Polariser", is placed in front of the sample to polarise the incident light to the desired orientation, indicated by angle α_{P}. The second polariser, which is also called the analyser and thus denoted by "Analyser", is placed in the optical path after reflection from the sample surface. The polarisation orientation of the analyser is thus indicated by angle α_{A}. Using this geometry, tiny polarisation changes in the light can be picked up by projecting the light polarisation onto a fixed axis.

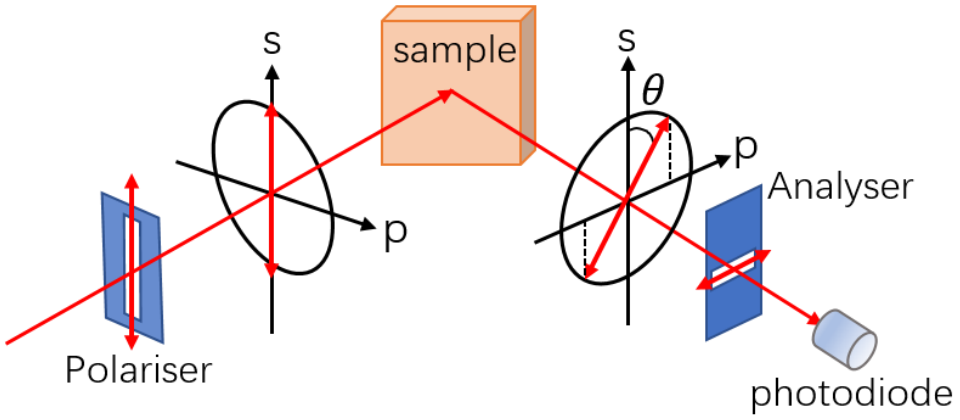

Figure 3.3: Schematic illustration of a simple cross-polariser method of detecting the Kerr effect. The incident light is s-polarized while the polarization orientation rotates by an angle θ after reflected from the magnetic sample.

The incident linearly polarised light can be described as the electric field amplitude

$$\boldsymbol{E} = E_{\mathrm{s}}\boldsymbol{e_{\mathrm{s}}} + E_{\mathrm{p}}\boldsymbol{e_{\mathrm{p}}} = \begin{pmatrix} E_{\mathrm{s}} \\ E_{\mathrm{s}} \end{pmatrix} = \begin{pmatrix} \sin\alpha_{\mathrm{P}} \\ \cos\alpha_{\mathrm{P}} \end{pmatrix}, \tag{3.1}$$

where E_{s} and E_{p} are the components along the unit vectors $\boldsymbol{e_{\mathrm{s}}}$ and $\boldsymbol{e_{\mathrm{p}}}$, which are perpendicular and parallel to the plane of incidence, respectively. The intensity of the

light is given by

$$I = EE^{*}. \tag{3.2}$$

Using matrix multiplication to account for the various optical components, the intensity detected can thus be derived as

$$I_d = R\left|(\sin\alpha_{\mathrm{A}} \quad \cos\alpha_{\mathrm{A}})S\begin{pmatrix}\sin\alpha_{\mathrm{P}}\\ \cos\alpha_{\mathrm{P}}\end{pmatrix}\right|^2, \tag{3.3}$$

where $R = |r_{\mathrm{s}}|^2$ is the reflectivity. Experimentally, as schematically illustrated in Fig. 3.3, α_{P} is always set at $\alpha_{\mathrm{P}} = 90°$, which means that the incident light is s-polarised, and the orientation of the analyser, A, almost crosses that of the polariser, P, giving $|\alpha_{\mathrm{A}}| \ll 1$. In this special case, the reflection from the magneto-optical sample, which contains the Kerr rotation, can be expressed using a Jones matrix as shown:

$$S = r_{\mathrm{s}}\begin{pmatrix}1 & -\tilde{\theta}\\ \tilde{\theta} & \rho\end{pmatrix}, \tag{3.4}$$

where r_{s} and r_{p} are complex reflection coefficients, and $\rho = \rho' + i\rho'' = r_{\mathrm{p}}/r_{\mathrm{s}}$. $\tilde{\theta} = \theta + i\varepsilon$ is the complex Kerr rotation where $|\tilde{\theta}| \ll 1$; here, θ is the rotation change and ε is the change in ellipticity. Therefor the light intensity is detected as

$$I_d = R(\alpha_{\mathrm{A}}^2 + 2\alpha_{\mathrm{A}}\theta + \theta^2 + \varepsilon^2). \tag{3.5}$$

Due to the very small Kerr rotation, only $\theta{\sim}10^{-3}$ rad, the terms θ^2 and ε^2 are negligible. Thus, in the dynamic case, and taking the partial derivative of Equation 3.5, the detected intensity change will be

$$\Delta I_d = 2R_0\alpha_{\mathrm{A}}\Delta\theta(t) + \alpha_{\mathrm{A}}^2\Delta R(t), \tag{3.6}$$

where $\Delta\theta(t)$ is the transient Kerr rotation representing the magnetisation dynamics and $\Delta R(t)$ is the transient reflectivity change, which is nonmagnetic, and which is caused by electron and lattice temperature changes. Equation 3.6 suggests that any increase in α_{A} will enhance the signal sensitivity; however, this will also enhance the nonmagnetic background scaling α_{A}^2. Consequently, α_{A} should be kept small. Unfortunately, when α_{A} becomes close to θ, the terms θ^2 and ε^2 are no longer be negligible, and this interferes dramatically with the measurements.

In order to improve sensitivity to small rotations in the polarisation of the reflected beam and to avoid the limitations of using a crossed-polariser configuration, a balanced-

diodes optical bridge detector is used in TR-MOKE measurements. As shown in Fig. 3.4, a polarising beam splitter (Wollaston prism) is adjusted to equalise the amplitudes of both the s- and p- components in front of the detectors. The intensities of the two components are detected separately using a pair of balanced photodiodes, and a difference signal is thus generated. Akin to the expression of intensity in Equation 3.4, the difference signal obtained is given by

$$I_d = R\left|(\sin\alpha_A \quad \cos\alpha_A)S\begin{pmatrix}\sin\alpha_P\\ \cos\alpha_P\end{pmatrix}\right|^2 - R\left|(\cos\alpha_A \quad -\sin\alpha_A)S\begin{pmatrix}\sin\alpha_P\\ \cos\alpha_P\end{pmatrix}\right|^2. \quad (3.7)$$

Using $\alpha_A = 45°$ yields an induced transient response in TR-MOKE where

$$\Delta I_d = 2R_0\Delta\theta(t) + 2\theta_0\Delta R(t). \quad (3.8)$$

As with Equation 3.6, this features two competing terms: one is the transient Kerr signal $\Delta\theta(t)$, representing magnetic response, while the other is the nonmagnetic transient reflectivity, $\Delta R(t)$. However, the signal sensitivity is significantly enhanced in Equation 3.8 because the small value of α_A in the first term no longer affects detection. Furthermore, in the exactly balanced configuration, $\alpha_A = \frac{1}{2}\arctan(\theta_0/2)$, the detected response will only feature the magnetic term $\Delta I_d = 2R_0\Delta\theta(t)$. Thus, an important improvement over the crossed-polariser configuration is achieved. The ellipticity change can also be measured with only a small modification: a quarter-wave plate placed between the Wollaston prism and the sample changes the detected signal from rotation to ellipticity.

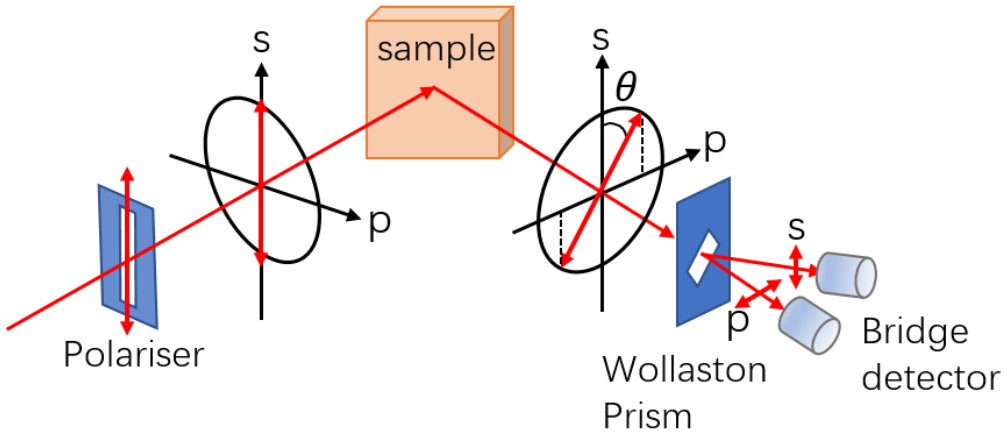

Figure 3.4: Schematic illustration of a balanced-diodes optical bridge detection of the Kerr

effect.

It is worth considering the symmetry of the detected signal with respect to the reversal of the magnetic field. Equation 3.8 intuitively suggests that ΔI_d is antisymmetric because $\Delta\theta$ and θ_0 have the same symmetry. However, as shown in Ref. [134], the TRMOKE curves are not completely inverted after reversal of the external magnetic field. This asymmetry is explained simply by means of a phenomenological model in that the magnetisation-independent contribution comes from the pump-induced change of optical anisotropies. In addition, the effect of reflectivity change $\Delta R(t)$ is not as small as assumed in many cases [23], and this can contribute to additional transient MOKE signal in the background. In all the TR-MOKE experiments, no matter using the bridge detection or the cross-polarizer detection, the photodiodes are used to measure the light intensity change which is proportional to the Kerr rotation.

3.3 TRMOKE experimental setup

This section will introduce the time-resolved magneto-optical Kerr effect technique used in this thesis. The experimental setup was based on the optical pump-probe technique, which is also called the stroboscopic technique. The magnetisation of the sample is optically stimulated by means of a pump laser pulse; after a controlled delay time, a probe laser pulse arrives at the sample to sense changes in the magnetisation. This process repeats again and again in order to gain good signal to noise ratio, and the repetitive measurements are taken at the frequency of the laser repetition rate. An external field is normally applied to reset that the magnetisation after each pump excitation. As long as the delay time between the pump and the probe remains unchanged, the temporal magnetic information sensed by the probe is the same. The temporal resolution is therefore determined by the pulse width of the probe. This section will present the key parts of the setup in terms of studying ultrafast magnetisation processes.

3.3.1 Laser sources

A precondition for the TRMOKE technique is to have a pulsed laser source. The pulse frequency should preferably have a high repetition rate (kHz~MHz) to achieve desired signal to noise ratio without prolonged measurement time; the more the probe pulses during the measuring period, the higher the signal to noise ratio. However, thermal accumulation issues will be significant at very high repetition rates, as the laser-induced heat cannot dissipate completely during each pump-probe cycle, which makes the ambient temperature increase. This heat accumulation will affect experimental conditions and becomes pronounced with high pump fluence. Thus, a laser source with a repetition rate in the kHz range may be preferred to one that works in MHz.

The femtosecond pulsed laser used in York is a Spectra-Physics Femto Spitfire system. It consists of three units: a MaiTai seed laser, an Evolution pump laser, and a Spitfire regenerative amplifier. The MaiTai seed laser consists of a continuous wave (CW) pumping chamber with a pulsed conversion chamber. The first chamber features a diode pumped, intra-cavity, frequency doubled, solid-state Nd:YVO_4 523 nm laser. The second chamber is a mode-locked Ti:Sapphire cavity. The MaiTai seed laser generates a 1.5 W pulsed laser with a wavelength of 800 nm and a frequency of 80 MHz and pulse width of 100 fs. The Evolution pump laser has an output wavelength of 527 nm; the laser resonator is acousto-optically Q-switched at 1 kHz, with pulses lasting for 100 ns. The power of the pump laser is 21 W, and this is used to pump the seed laser beam. In the Spitfire regenerative amplifier, the seed laser is amplified using a state-of-the-art chirped pulse amplification technique [135]. In general, the seed pulse is temporally stretched, reducing its peak power, prior to amplification, and then recompressed to form a short, high power pulse. The output is thus a 1 W pulsed beam with an 800 nm wavelength and a repetition rate of 1 kHz. The beam spot size is about 1 cm in diameter. The laser source used in Nanjing University is a new Coherent Libra laser system. Here, the three parts described above are integrated into a single laser, with key features and techniques similar to those of the York system, but with a higher output of ~5 W and a shorter pulse width of 60 fs.

3.3.2 Pump and probe beam

A schematic drawing of the appropriate pump-probe set-up is depicted in Fig. 3.5. The output beam from the Spitfire amplifier is split into two beams of different intensities by an ultrafast beam sampler (BS), at a ratio of about $9:1$. The beam with the greatest intensity is used as the pump and the other acts as the probe. After passing through the BS, the pump beam follows a fixed-length optical path before being focused onto the sample surface by a focus lens. The pump beam is linearly p-polarised straight out of the laser cavity, with an ellipticity of about $1/100$. This polarisation of the pump beam is inessential here, where it is only used to trigger a magnetic precession or to demagnetise the sample. However, in the experiments where magnetisation responds differently to different polarisations of the pump beam such as all-optical magnetisation switching (AOS), the polarisation of the pump beam must be accurately defined using polarising optics.

On the probe path, after being reflected from the BS, the frequency (wavelength) of the beam is doubled (decreased by a factor of two) by passing through a beta Barium Borate (BBO) crystal. This changes that the wavelength of the probe beam to 400 nm and its polarisation to s-polarised due to the nonlinear optical effects of the BBO crystal. A bandpass filter which only transmits wavelength within 400 ± 10 nm is placed after the BBO crystal to block any residual 800 nm beam. A Glan-Thomson or Glan-Taylor polariser is used so that the probe beam is linearly s-polarised with an extinction ratio of $1:10^5$ as required for MOKE measurements. The path length of the probe beam is varied by a retroreflector (also called as "corner cube") mounted on a motor-driven translation stage. This combination of retroreflector and the translation stage, also known as the "delay line", controls the time delay between the pump and probe pulses. Details of the delay line and the control of time delay will be presented in the next section. After the delay line, the probe beam is directed to become collinear with the pump beam before focused by the same lens to ensure the overlapping of both pump and probe spots on the sample surface. As shown in Fig. 3.5, after focusing the probe beam is incident at a small angle of about $4°$ with respect to the sample normal, while

the pump beam is normally incident directly onto the sample surface. This geometry means that mainly the out-of-plane component of the magnetisation contribute to the signal as discussed in chapter 2. The reflected probe beam is collimated by the same focus lens and its polarisation rotation, the Kerr rotation reflecting the magnetisation change is measured by a combination of a Wollaston prism and a bridge detector, as presented in Section 3.2. The pump and probe beam intensities are tuned by means of variable neutral density optical filters to maintain the ratio between pump and probe at larger than 10 ($I_{\mathrm{pump}}/I_{\mathrm{probe}} > 10$) to minimise any self-effect from the probe on the magnetisation dynamics. A magnetic field generated by an electromagnet is applied to reset the magnetisation state after each pump-probe cycle. This electromagnet is placed on a rotation stage in order to change the angle of the magnetic field horizontally with respect to the sample plane. Magnetic-field-orientation dependent measurements are usually required for studying magnetic precession as the precession frequency is determined by the applied field and its orientation. In demagnetisation or AOS experiments, a fixed magnetic field, introduced by an electromagnet or permanent magnet, and applied either in the plane or perpendicular to it, is sufficient to reset the magnetisation state. As shown in Fig. 3.5, an optical chopper is also used to modulate the pump beam, and this blocks the pump pulses at certain frequencies. A lock-in amplifier can thus be used to measure the photodetector signal based on the frequency of this modulation, in order to increase the signal-to-noise ratio.

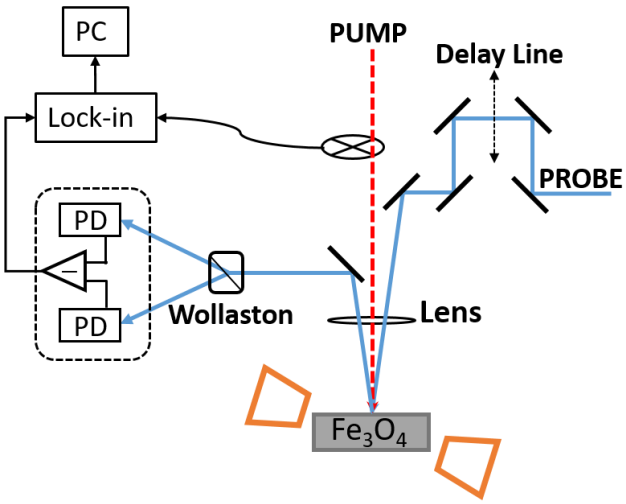

Figure 3.5: Schematic pump-probe TR-MOKE setup.

3.3.3 Pump and probe spot overlap

The spatial overlap of the pump and probe spots on the sample surface is of great importance in pump-probe measurements. To directly observe the position of the laser spots on the sample surface, an image system based on a charge-coupled device (CCD) camera must be used along with a 3-D translation sample stage of micrometre precision.

There are two methods for taking images of the sample surface using a CCD camera. The simplest way is to directly take the photo by placing the camera close to the sample. Using a high-amplification camera lens is necessary, and in this way, a spot of $\sim 100\ \mu m$ size can be clearly observed. However, the issue arises where high-vacuum-prepared thin films normally have good surface quality with little surface defects or contaminations, and therefore scatter little light to form an image. This happens particularly for $400\ nm$ probe beams of low intensity. The solution is to place a piece of Si substrate with its rough side upwards alongside the sample. Strong scattering light from the rough surface, form a clear image of both the pump and probe focused spots. After overlapping the two beam spots, the sample plane can be moved back to where the spots are without changing the beam focusing.

Another method is to build up an imaging light path, as shown in Fig. 3.6. A thin beam sampler is used to partially reflect the reflected probe and pump beams from the sample. A focus lens is then used in front of the CCD camera to form the image. The limitation is that, in contrast to the first method, as the image is formed directly by the part of the reflected laser beam, the intensity could be too bright without proper attenuation. It is better to remove the beam sampler after checking the overlapping to avoid reduction in the probe intensity for signal detection.

The beam spot size on the sample surface is a crucial parameter for calculating pump fluence. Here, a commercial beam profiler made of a CCD camera was used to characterise the beam size. When the pump and probe beam spots were adjusted to be overlapped, the beam profiler replaced the sample in the same position. By adjusting the position of the beam profiler to make the two spots overlap again, it can be assumed that the beam profiler is at the same position the sample previously occupied. The

diameters of the spots can thus be directly measured. This process for measuring the spot size is not required for every experiment, because as long as the focusing of the light is unchanged, the spot size will not change. It must, however, be noted that the ultrafast pulsed laser has a very high energy for each pulse, and thus the beams must be attenuated significantly to protect the beam profiler from damage.

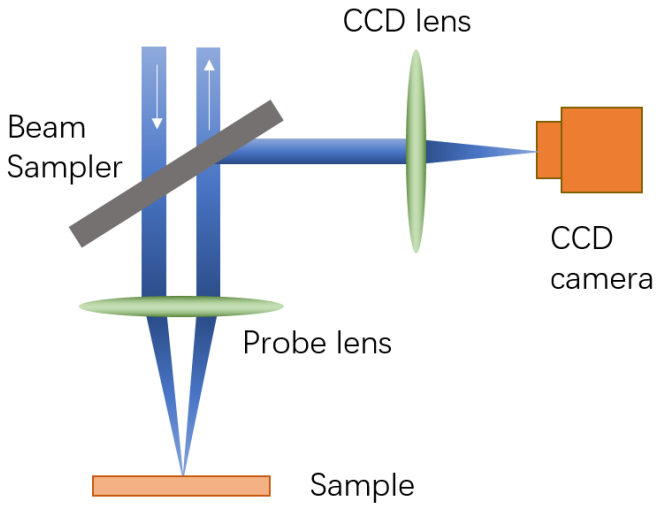

Figure 3.6: CCD camera-based image setup in a TRMOKE system.

3.3.4 Delay line and delay time

As briefly mentioned in section 3.3.2, the delay line, which is a combination of a retroreflector and a motor driven translation stage, is used in the path of the probe beam to control the time delay, Δt, between the pump and probe. By moving the retroreflector forward or backward in the translation stage, the length of the probe light path is controlled, and thus the time delay time, Δt, is also controlled. The reflected beam from the retroreflector is parallel to the direction of incidence, and the separation between the incident and reflected beams is dictated by the distance between the point of incidence and the centre of the retroreflector's base plane. Thus, in order to maintain the position of the probe spot on the sample surface, the incident beam of the retroreflector must be strictly perpendicular to the retroreflector's base plane. One way to ensure this is to extend the reflected beam in a long optical path using reflective mirrors to check that the laser spot is stable when moving the stage forward or backward.

The translation stage used in the current investigations to control the position of

the retroreflector was a Thorlab 300 mm linear translation stage with integrated controller (stepper motor). Its resolution is 2 µm, which corresponds to a temporal resolution of 13.3 fs ($\frac{2\ \mu m \times 2}{3\times10^8\ m/s}$). It is preferable to move in steps larger than five times the resolution, to minimise the potential backlash effect. By measuring and adjusting the optical path of the two beams from the first beam splitter to the sample surface, the coarse position of the "zero delay" can be defined such that it can be positioned close to the short end of the translation stage. "Zero delay" refers to a temporal overlap of the pump and probe due to equal optical path length. This "zero delay" can directly observed in the time-domain reflectivity scan obtained from an GaAs sample, as shown in Fig. 3.7 [136]. The fringes in the reflectivity data is caused by the interference between the reflected probe (800 nm without BBO) and the scattered pump light when they are temporally overlapping on the sample surface/detector. The FWHM of the fringes is approximately 250 fs, which indicates an 100 fs pulse width, as expected.

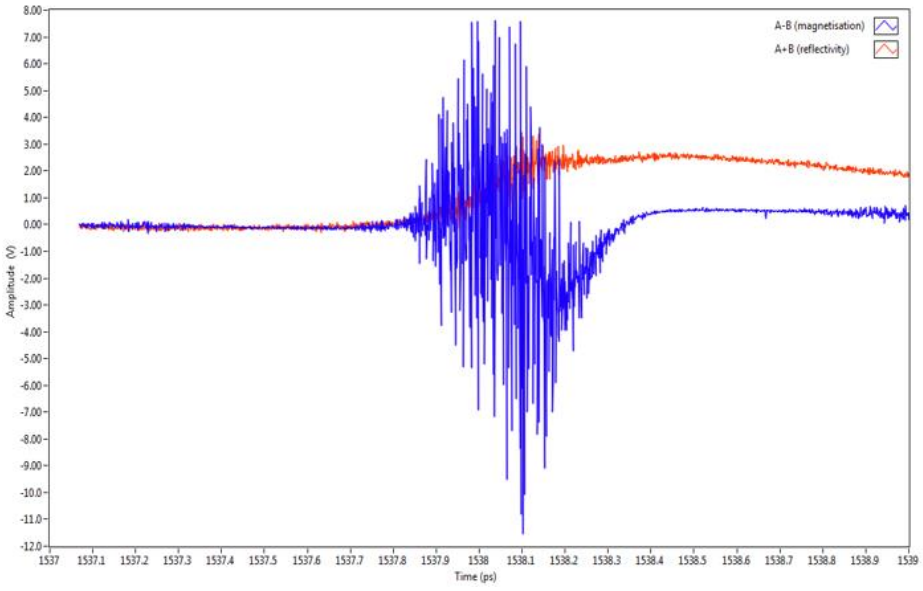

Figure 3.7: The time-domain scan data around zero delay. The step size is 1 fs, the blue line is the Kerr signal, and the red line is reflectivity change [136].

3.4 Comparison between TR-MOKE and FMR

It has been reported by different groups to compare the different methods described for measuring the magnetic damping parameters. In 2006, two substantive comparative studies were reported [41, 130]. In Ref. [41], the effective damping was measured using VNA-FMR, PIMM and TR-MOKE and the values showed good agreement, but the intrinsic damping values were of some variation. In this work, the effective damping obtained from TR-MOKE was lower than the other methods and this was attributed to the very small probed area. In the very small probed area, the magnetic properties are more uniform and less susceptible to extrinsic damping processes associated with inhomogeneities. Good agreement between conventional FMR and TR-MOKE for Ni was also demonstrated in Ref. [52], in which the issue of local/non-local probing was considered. Recently, using TR-MOKE and x-band cavity FMR, the damping values for Pt/Co/Pt as function of Co thickness was measured [137]. The values are generally in good agreement while there is some variation between the values for the thinnest samples. Recent study showed that additional damping, termed radiative damping, can broadening the linewidth in FMR measurements. the inductive coupling of the precessing magnetization can back into the transmission line can lead to a small enhancement in the measured damping [138]. this inductive coupling is inevitable in all geometries when the sample is very close to a conductive transmission line. However, direct laser-induced precession measured by TR-MOKE will not be affected.

Normally, the effective damping constant consists of intrinsic and extrinsic components and the extrinsic damping mainly comes from magnetic inhomogeneity or two magnon scattering. In TR-MOKE measurement, by varying the applied field, the intrinsic and extrinsic contributions can be separated. In the low magnetic field region, the effective field is dominated by the spatially fluctuating anisotropy field which leads to increased damping, while in the high field region the effect of anisotropy field becomes weak since the external field dominates and hence the effect of the magnetic inhomogeneity decreases along with the damping constant [53, 58, 139]. Therefore, if the applied field is large enough that the effective damping no longer change when the

field changes, we can treat this value of the effective damping as the intrinsic damping or at least the upper bound of it [104].

3.5 Angle-resolved photoemission spectroscopy (ARPES)

In order to investigate the correlation between the electronic structure, especially at the Fermi level, and magnetic damping, angle-resolved photoemission spectroscopy (ARPES) was implemented at Nanjing University. A brief description of ARPES will be presented in this section.

Since the photoelectric effect was discovered by Hertz in 1887 [140] and later explained as a manifestation of the quantum nature of light by Einstein in 1905 [141], photoelectron spectroscopy has become a powerful technique for directly probing the single-particle spectral function in solid materials.

When light is incident to a material, the electrons in the top several or tens of atom layers can absorb photons to escape from the material. The kinetic energy of the outgoing photoelectrons can be calculated using the following equation [141]:

$$E_{\mathrm{kin}} = h\nu - \phi - E_{\mathrm{B}}, \tag{3.9}$$

where $h\nu$ is the photon energy and ϕ, the work function, is the potential barrier at the surface that prevents valence electrons from escaping. The work function in many materials is typically around $4\sim5$ eV, and thus photon energy should be higher than 5 eV in photoemission spectroscopy. The energetics of the photoemission process are sketched in Fig. 3.8(a), and this indicates that the intensity of the spectrum is proportional to the density of states of the material.

The geometry of an ARPES experiment is shown in Fig. 3.8(b). After being stimulated by a beam of monochromatized radiation, supplied either by a gas-discharge lamp or a synchrotron beamline, electrons escape from the material into the vacuum in all directions. Using an angle resolved electron energy analyser, the photoelectrons can be collected in a finite acceptance angle. The kinetic energy, E_{kin}, of the photoelectrons for a given emission angle is thus measured, and the modulus of the

momentum of photoelectrons, $\boldsymbol{p}$, is also obtained using

$$p = \sqrt{2mE_{\mathrm{kin}}}, \tag{3.10}$$

where m is the electron mass. The momentum components that are parallel and perpendicular to the sample surface are determined based on the polar angle, θ, and the azimuthal angle, φ. For the low photon energies typically used in ARPES experiments, photon momentum is negligible compared to electron momentum. Thus, the kinetic energy and momentum of the photoelectrons, the binding energy E_{B}, and the crystal momentum, $\hbar\boldsymbol{k}$, inside the solid are related as follows:

$$p_{\parallel} = \hbar\boldsymbol{k}_{\parallel} = \sqrt{2mE_{\mathrm{kin}}} \cdot \sin\theta\,. \tag{3.11}$$

Here, $\hbar\boldsymbol{k}_{\parallel}$ is the component parallel to the surface of the electron crystal momentum in the extended Brillouin zone. For a large θ angle, the actual detection of the electron momentum may reach a higher-order Brillouin zone by subtracting the corresponding reciprocal lattice vector, $\mathbf{G}$. It must be noted, however, that the momentum component perpendicular to the sample surface is not conserved due to the lack of translational symmetry along the surface normal.

From Equation 3.11, the momentum resolution, $\Delta k_{\parallel}$, can be simply calculated as

$$\Delta k_{\parallel} = \sqrt{2mE_{\mathrm{kin}}/\hbar^2} \cdot \cos\theta \cdot \Delta\theta, \tag{3.12}$$

where $\Delta\theta$ is the angular resolution of the electron analyser. From Equation 3.12, it is clear that the momentum resolution will improve at lower photon energy levels, i.e. lower E_{kin}, and this is why most ARPES experiments are performed at photon energies in the ultraviolet range, particularly for $h\nu < 100$ eV.

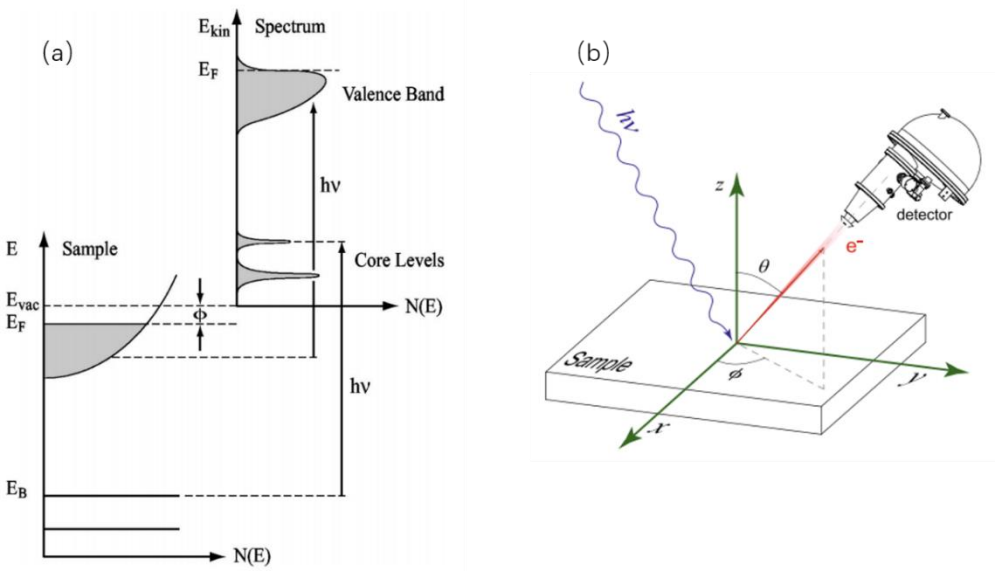

Figure 3.8: (a) Energetics of the photoemission process. The electron energy distribution produced by incoming photons and measured as a function of the kinetic energy E_{kin} of the photoelectrons (right) is more conveniently expressed in terms of the binding energy E_{B} (left) when one refers to the density of states inside the solid ($E_{\mathrm{B}} = 0$ at E_{F}) [142]. (b) Schematic of ARPES [143].

3.6 Sample preparation

The preparation of the various magnetic films involved several film growth techniques, such as molecular beam epitaxy (MBE) and pulsed laser deposition (PLD). This section thus briefly introduces these techniques.

3.6.1 Molecular beam epitaxy (MBE)

Molecular beam epitaxy (MBE) is an epitaxy method for high quality thin film deposition. Using an ultrahigh vacuum (UHV) technique, this growth method allows a growth rate as slow as a few atom layers per minute. The films are growth one monolayer at a time, which means that they can be grown with a distinct crystallographic relationship to the substrate, which is why MBE is one of the best methods for growing high-quality single crystal films.

The MBE system used in the Spintronics and Nanodevice Lab in York is schematically illustrated in Fig. 3.9. The growth chamber was equipped with a load-

lock chamber and a transfer arm used for loading and taking samples. The three-axis sample manipulator was able to rotate and adjust the position of the sample in the X - Y plane accurately. Using a heating filament, the substrate could be annealed up to 550 ℃, and a combination of a rotary pump, turbo pump, and titanium sublimation pump was used to reduce the base pressure of the growth chamber below 2×10^{-10} mbar after the "bake out" process. An electron gun and a phosphorescent screen were used to monitor the reflective high energy electron diffraction (RHEED) pattern, which reflects the crystal structure (single crystal, poly crystal, or amorphous) of the growth surface. An argon ion gun was used to sputter the substrate surface before film deposition to remove any contamination from the surface. This process also gently removes the surface layer of the substrate, in this case GaAs(100), to reveal a virgin layer. After annealing the substrate at high temperature, the GaAs(100) substrate displays a 4×2 or 4×6 surface reconstruction, which can be monitored by means of the RHEED pattern.

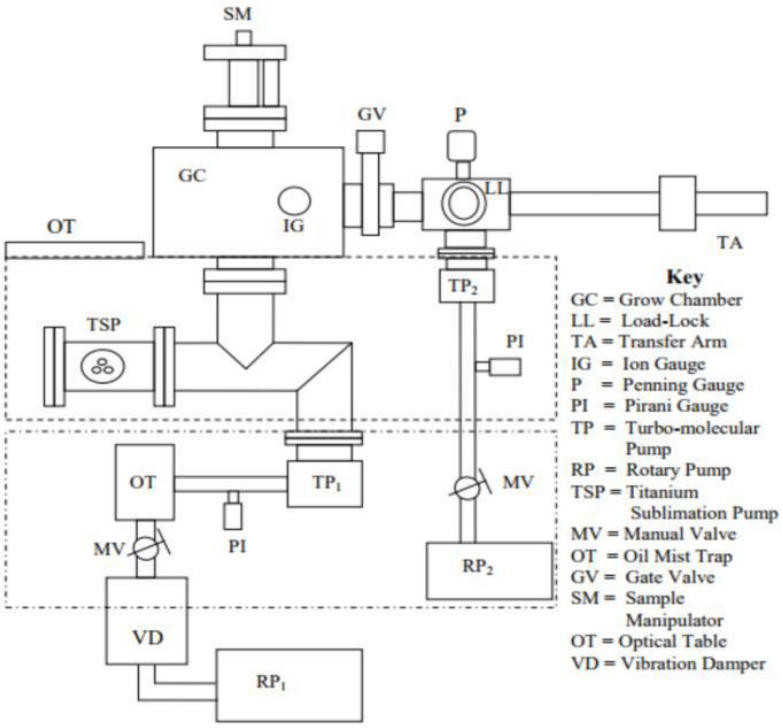

Figure 3.9: Schematic drawing of the MBE system in York [144].

3.6.2 Pulsed laser deposition (PLD)

Pulsed laser deposition (PLD) has been used to deposit high quality films for more than a decade. Its ease of use and success in depositing materials of complex stoichiometry, especially oxide thin films, has gained a great deal of attention. In this thesis, the Fe_3O_4 sample was grown by the Tokyo Institute of Technology in Japan using PLD [145, 146].

PLD uses high power laser pulses to melt, evaporate, and ionize material from the surface of a target. The laser source used in the current experiment was a KrF excimer laser with a wavelength of $248\ \text{nm}$ and a pulse duration of $\sim 20\ \text{ns}$, and the laser power density was fixed to $\sim 2.3\ \text{J/cm}^2$. The ablation event produces a transient, high luminous plasma plume that expands rapidly away from the target surface, and the ablated material is collected on an appropriately placed substrate where it can condense to firm a thin film. One of the main advantages of this technique is that it is generally easier to obtain the desired film stoichiometry for multi-element materials using PLD than by using other deposition technologies. High quality samples can also be grown reliably in a shorter time than by using MBE.

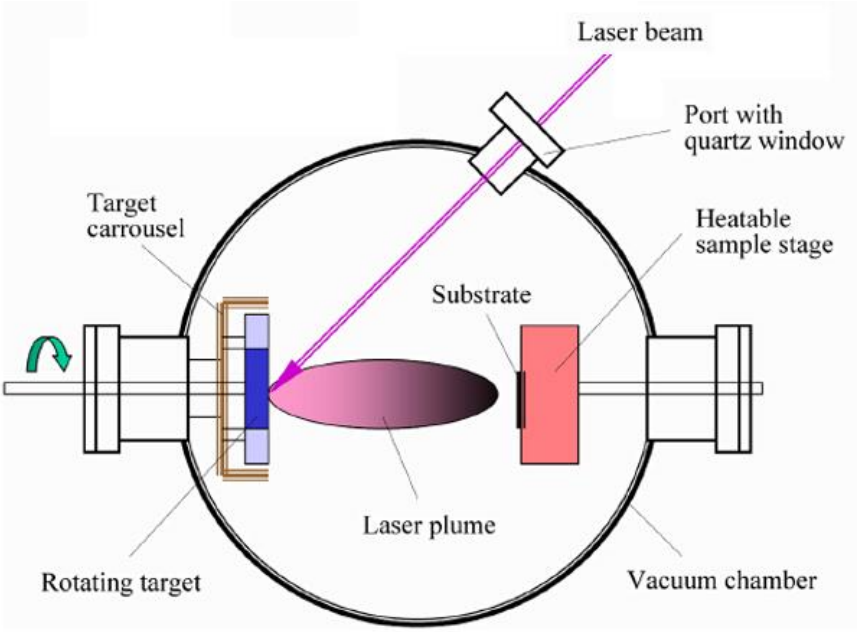

Figure 3.10: Schematic view of a PLD system [147].

Chapter 4 Magnetic and spin dynamic properties study in Au/Fe/Cr/GaAs(100) heterostructures

The origin of the uniaxial magnetic anisotropy (UMA) in ultrathin Fe/GaAs heterostructures is still unclear. Recently, an anisotropic magnetic damping was observed in ultrathin Fe/GaAs [148]. In this chapter, a set of Fe/Cr/GaAs samples are prepared by varying the thickness of Cr interlayer, to investigate the effects of the interface on these anisotropic phenomena. The potential relation between the UMA and magnetic damping will be investigated by the means of time-resolved magneto optic Kerr effect (TRMOKE) and X-ray magnetic circular dichroism (XMCD).

4.1 Introduction

Ferromagnetic metal (FM)/semiconductor(SC) heterostructure is an important material system for the development of next generation magnetoelectronic device [149-154]. At present, semiconductor technologies only make use of the charge property of electrons, whereas spintronics make use of both spin and charge properties of electrons which is the key for improving operation frequencies, reducing Joule heating, increasing storage densities, and achieving non-volatility. In this context, it is necessary to investigate the fundamental magnetic properties of FM/SC heterostucture, especially of the interface between ultrathin FM films and SC substrate [155-157]. One of the most popular FM/SC heterostuctures is the Fe/GaAs which has been extensively studied. The fact that the lattice constant of body-centered-cubic (bcc) Fe ($a_0 = 2.866$ Å) is almost exactly half that of GaAs ($a_0 = 5.654$ Å) facilitates an epitaxial growth of Fe on GaAs substrate, which is the most popular semiconductor studied [158, 159]. The onset of the room-temperature ferromagnetism was revealed at a Fe coverage of 4.8 ML [123], and an in-plane uniaxial magnetic anisotropy (UMA) was observed [160-162], unexpected from the four-folder crystalline symmetry of bulk bcc Fe. The

exact microscopic mechanism of the UMA in Fe/GaAs is still of hot debates. The interfacial anisotropic strain induced by magnetoelastic coupling due to lattice mismatch between GaAs and Fe was considered as the origin of the UMA [122, 163]. Another potential deterministic factor is the GaAs substrate reconstruction [123, 159, 164]. The last potential mechanism of the origin of the UMA is chemical bonds at the Fe/GaAs interface, which we will discuss in this chapter.

On the other hand, the fundamental parameter in magnetism, the phenomenological Gilbert damping constant, determining the performance of spintronic devices, is of great interests. Though magnetic damping, in general, is assumed to be isotropic, several theoretical works [165-168] predict that the damping should be anisotropic in single-crystalline ferromagnetic metals, such as bulk Fe. Depending on the orientation of the magnetisation direction, the electronic structure as well as the shape of the Fermi level is suggested to be anisotropic due to the spin-orbit coupling. The magnetic damping, determined by the anisotropic electronic structure, is therefore anisotropic. However, due to smearing of the energy bands in the presence of electron scattering, this anisotropic damping can be severely reduced. This is the reason why only a few experiments [169-171] have tried to prove the existence of anisotropic damping in bulk magnets and these attempts were not successful.

Very recently, Chen *et al.*, unambiguously demonstrated an anisotropic Gilbert damping in ultrathin Fe layers on GaAs(001) [148]. In this work, using spin-orbit ferromagnetic resonance (SO-FMR) [172, 173], a magnetic-field-angle dependence of the linewidth were measured. Consequently, the magnetic damping was obtained. As shown in Fig. 4.1, an anisotropic damping shows twofold symmetry: a large value of damping along magnetic easy axis $[110]$ and a small value of damping along magnetic hard axis $[\bar{1}10]$. This anisotropic magnetic damping was explained by an anisotropic density of state at the Fe/GaAs interface due to symmetry breaking. This anisotropic damping was exclusively observed in an ultrathin Fe film of $1.3\ \mathrm{nm}$ (9 ML) while the damping is nearly isotropic in Fe film of $1.9\ \mathrm{nm}$ (15 ML).

In this context, a question has been raised straightforwardly: is the anisotropic magnetic damping related to the magnetic uniaxial anisotropy in ultrathin Fe/GaAs

films? In other word, is these two anisotropic properties share the same underlining mechanism? Also, the significance of the Fe/GaAs interface is discussed in both magnetic and damping anisotropy, but is the interface affect both these two anisotropies equally? These questions are still open and of great importance to understanding the Fe/GaAs interface induced magnetic properties. To explore these issues, we have designed a set of Fe/GaAs sample of a fixed Fe thickness (10 ML) with a varied Cr interlayer between Fe and GaAs of thickness ranging from 0.5 ML to 20 ML. The magnetic anisotropy is investigated by vibrating sample magnetometer (VSM) and the magnetic damping constant are obtained by TR-MOKE. Furthermore, X-ray magnetic circularly dichroism (XMCD) is applied to obtain the spin and orbital moments of Fe. Combining these techniques, the potential relation between magnetic anisotropy and the magnetic damping is studied. Also, by changing the thickness of the Cr interlayer, the role of the Fe/GaAs interface and its contribution to these anisotropies are also investigated.

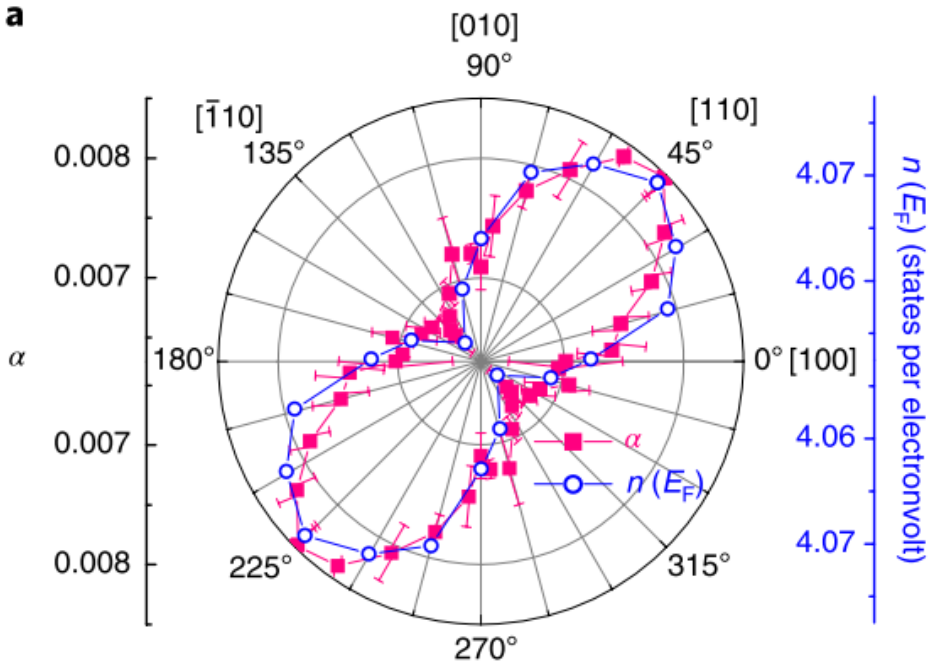

Figure 4.1: Magnetic-field-angle dependence of the damping constant for Fe(1.3 nm)/GaAs(001). The anisotropic damping shows twofold symmetry, which results from the anisotropic density of states at the Fe/GaAs interface, as shown by open symbols [148].

4.2 Sample growth and RHEED patterns

The 10 ML Fe films with a Cr interlayer of different thicknesses were grown on GaAs(100) substrates in a molecular beam chamber using an e-beam evaporator at ambient temperature. The commercial GaAs(100) substrates were chemically cleaned [174] before transferred into the MBE chamber. Firstly, any contaminants on the substrate surface were removed using acetone, iso-propyl alcohol (IPA) and deionized water. The second step was to remove the oxide layer by immersing the substrate into an $H_2SO_4/H_2O_2/H_2O$ (4:1:1) solution for 45 seconds. All these processes were performed in a level 100 clean room to prevent any contamination by dust particles. The chemical etched substrate was immediately transferred into an MBE chamber with a base pressure below 2×10^{-10} mbar. Afterwards the substrate surface was sputtered onto by low energy Argon ion beams to gently remove a thin layer of su rface material for 30 mins. Consequently, after annealing at 480 ℃ (at an annealing pressure lower than 8×10^{-9} mbar) for 60 mins to the natural oxides are further removed and a surface reconstruction is created. The growth pressures of Fe and Cr were below 6×10^{-10} mbar and 1×10^{-9} mbar. The deposition rates were 0.72 ML/min for both Fe and Cr growth, monitored by a calibrated quartz microbalance. A 3 nm Au capping layer was deposited on top of the films to prevent the Fe films from oxidization and contaminations.

The surface structure of the substrate and the deposited layers was monitored by the reflective high energy electron diffraction (RHEED) images. The RHEED pattern for $[0\bar{1}1]$ direction of GaAs substrate surface and the deposited Fe surface are shown in Fig. 4.2(a) and 4.2(b), respectively. The sharp streaky lines indicate a flat surface morphology, therefore the growth is smoothly pseudomorphic. A single crystalline structure of the deposited Fe layer is indicated from the RHEED pattern and this pattern will not be changed with a Cr interlayer (not shown). This means the Fe layer still possess a single crystalline structure which is expected as the lattice constants of Fe and Cr are almost same. The Cr and Fe coverages grow epitaxially on GaAs(100) with the epitaxial relationship Fe(100)<001>||Cr(100)<001>||GaAs(100)<001>. The measured

RHEED patterns are in consistent with the reported works [175, 176].

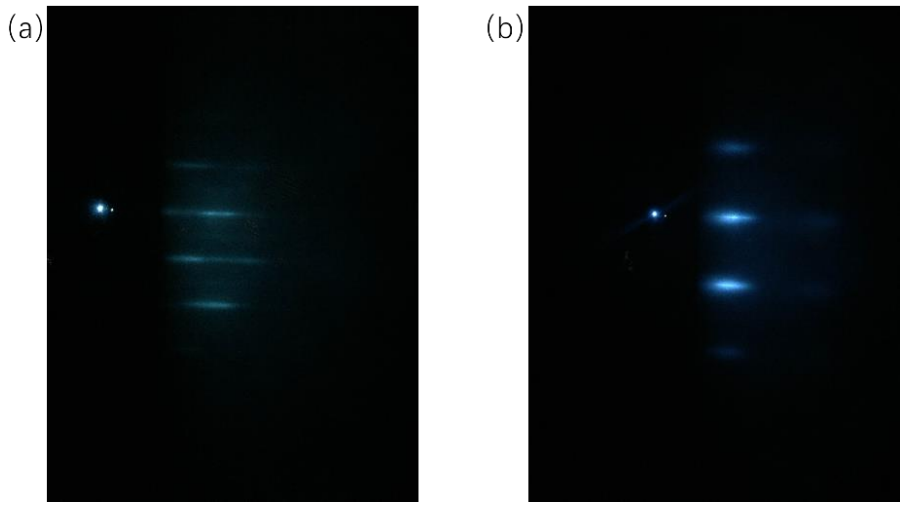

Figure 4.2: RHEED patterns for $[0\bar{1}1]$ direction of GaAs substrate surface (a) and the deposited Fe surface (b).

The lattice structures of the Cr interlayer with different thicknesses are also monitored by means of RHEED. Fig. 4.3(a) shows the RHEED pattern of GaAs(100) substrate along $[0\bar{1}1]$ direction after substrate treatment. When the substrate is covered by the initial 1 ML Cr, the RHEED pattern become blurry shown in Fig. 4.3(c). The RHEED pattern from GaAs substrate is partially undermined by the Cr clusters which shows no RHEED information. It can be seen from Fig. 4.3(d) that when the Cr coverage is deposited up to 4 ML, the RHEED pattern completely disappears. From 2 ML to 4.5 ML, the RHEED patterns from screen are fully dark, the Cr interlayer should be in a progress which is from an island film to be a continues film (single crystalline film). That makes the RHEED patterns are full dark. Until Cr interlayer growth to 5 ML, it can be seen from screen that the single crystalline RHEED pattern of Cr is shown and this pattern is week on the screen. But, it can evidence our guess: the interlayer Cr become a single crystalline film from 5 ML, and it fully covered GaAs(100) substrate and blocked the UMA from interface. This is an important discover that the UMA in Fe-GaAs(100) is from the interface interaction and not from the stress induced. It is easy to find that the Cr interlayer films (from 5.5 to 7ML) are all single crystalline by the clear RHEED patterns and these RHEED patterns become

more clearer compared with RHEED pattern from 5 ML Cr interlayer. The last RHEED pattern shown in Fig. 4.3(b) is from 10 ML Fe growth on 5 ML Cr interlayer, it shows this 10 ML Fe film is still the single crystalline film by RHEED pattern. The 10 ML Fe film was measured on the different thickness of Cr interlayer by RHEED measurement and all 10 ML Fe RHEED patterns all show the single crystalline structure. It means the Cr interlayer does not make any contribution on the formation of Fe single crystalline structure [123, 150]. The reason of using Cr as an interlayer is the lattice mismatch between Fe and Cr is quite small, Cr cannot be a major reason influence the Fe lattice structure.

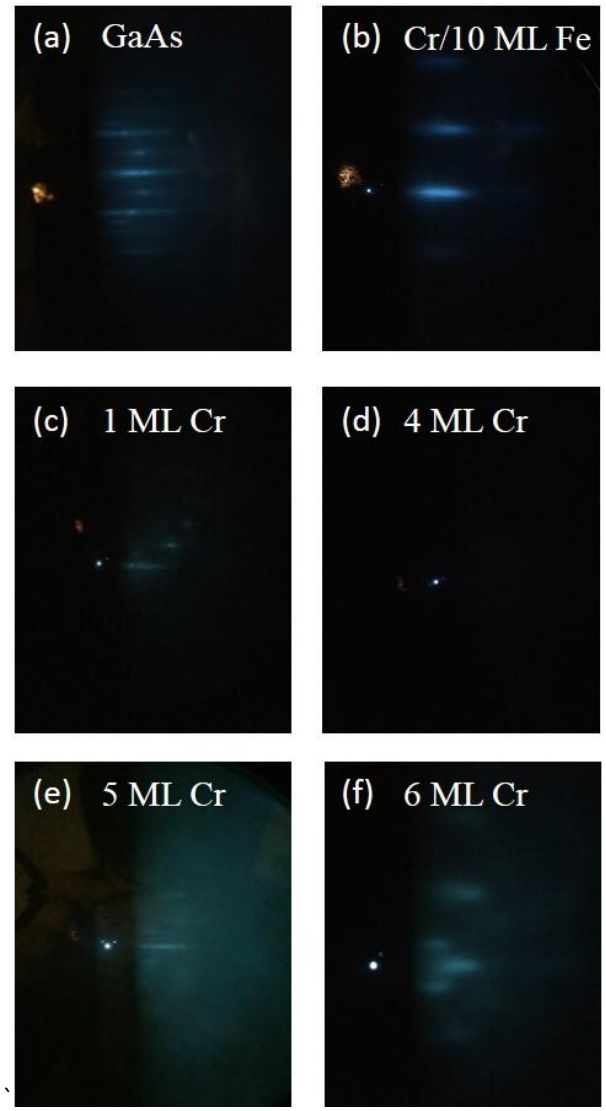

Figure 4.3: (a), (c)-(f)evolution of RHEED patterns of GaAs/Cr with different Cr layer thickness. (b) RHEED pattern of GaAs/Cr(5 ML)/Fe(10 ML).

4.3 VSM, TRMOKE and XMCD measurements

Fig. 4.4 shows the in-plane M-H loops measured by SQUID-VSM along the EA and HA of the Fe(10ML)/Cr(dCr)/GaAs(100) heterostructures with respect to the Cr interlayer coverage. Withouot the Cr interlayer (d_{Cr}=0 ML), a strong UMA is observed as similar as reported [123], showing a large magnetic saturation field H_s along the HA while a completely square-shape hysteresis loop is obtained along the EA. With increasing the coverage of the Cr interlayer, the decreasing value of the Hs along the HA shows a decreasing UMA until d_{Cr} is equal to 5 ML. When the Cr interlayer coverage is even larger, the UMA effect is not observable and the $[0\bar{1}1]$ and $[011]$ directions become equivalent intermediate axes [159], which is present in bulk bcc (100) Fe. This is due to the dominated cubic anisotropy showing a fourfold symmetry with the EA along [001] and [010] directions as the UMA is less pronounced with large Cr interlayer coverage.

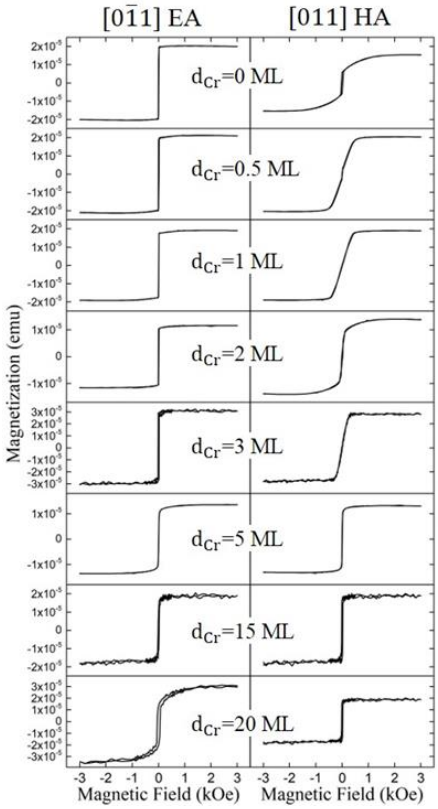

Figure 4.4: magnetic hysteresis loops measured by VSM in Au(3nm)/Fe(10ML)/GaAs(100) along $[0\bar{1}1]$ easy axis (left) and $[011]$ hard axis (right).

To quantitatively analysed the UMA as a function of the Cr interlayer coverage, the effective uniaxial anisotropy constant K_u^{eff} is obtained. Assuming the cubic anisotropy is unchanged for all the films due to the similar crystalline structure as shown in RHEED patterns, the value of the UMA field (H_k) can be obtained from the magnetic saturation field H_s along the HA direction. Furthermore, K_u^{eff} can be calculated by [157, 177]

$$K_u^{eff} = (H_k \times M_s)/2\,, \tag{4.1}$$

where the M_s is the measured saturation magnetization. In the inset of Fig. 4.5(a), the value of M_s is 1664 emu/cm^3 without Cr interlayer that is consistent with previous studies [178, 179]. The value of M_s increases gradually up to 2158 emu/cm^3, almost 50% enhancement compared to the value without Cr interlayer, as the Cr interlayer coverage increases to 5 ML. Then, the value of M_s decreases to some extent when the Cr interlayer coverage keeps increasing. The enhancement of M_s when the Cr interlayer coverage is below 5 ML cannot be fully explained, this may be related to the magnetic dead or half-magnetized layer or the antiferromagnetic interaction between Cr and Fe [180, 181]. The decrease of M_s, on the other hand, is believed to be attributed to the formed cubic anisotropy. It can be seen from Fig. 4.5(a) and (b) that the overall trend of H_k and K_u^{eff} as a function of Cr interlayer coverage is almost same, which means the M_s is not the dominate factor to determine the K_u^{eff}. The K_u^{eff} decreases gradually as the Cr interlayer coverage increases and it is close to zero when d_{Cr} is larger than 5 ML, where the UMA is not observed as shown in the corresponding M-H loops in Fig. 4.5(b). Because the single crystal structure of the grown Fe is unchanged for all the Cr interlayer coverage due to the tiny lattice constant mismatch with Cr and the Fe coverage keeps as a constant as 10 ML, the UMA is unambiguously reduced by the Cr interlayer between the Fe and the GaAs(100) substrate. Strikingly, the critical coverage of Cr interlayer (5 ML) to block the UMA in 10ML Fe coincide with the critical coverage (4.8 ML) of Fe grown on GaAs(100) as the onset of the

ferromagnetism [123]. It was demonstrated in Ref. [123] that, under 4.8ML, island-like Fe clusters are grown on GaAs and magnetic ordering is prevented for the first 3.5 ML while a superparamagnetic phase is found in the coverage range 3.5-4.8 ML. The islands coalesce and long-range ferromagnetic ordering develops at Fe coverage of 4.8 ML. In our measurements, it seems that the critical coverage 5 ML of Cr interlayer is the onset of a continuous layer to block the UMA of Fe film, via entirely blocking the Fe-GaAs.

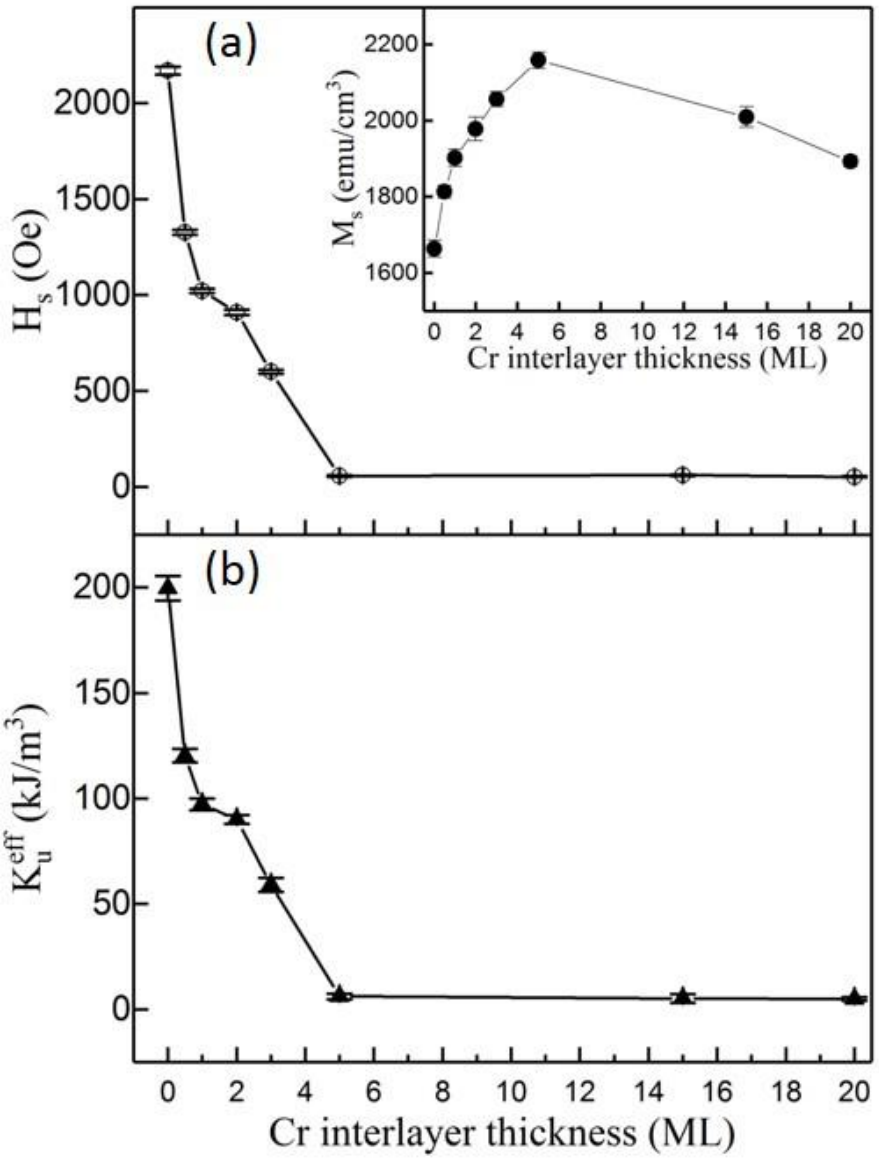

Figure 4.5: (a) saturation field, (b) effective uniaxial magnetic anisotropy constant, and the saturation magnetization (inset) as a function of Cr interlayer thickness in GaAs/Cr/Fe(10 ML) heterostructures.

To investigate the magnetisation dynamics and magnetic damping of the films, an

all-optical pump probe technique was employed to perform time-resolved magneto-optical Kerr effect (TRMOKE) measurement. The laser source is a pulsed Ti: sapphire regenerative amplifier with a wavelength of $800\ \mathrm{nm}$, a repetition rate of $1\ \mathrm{kHz}$, and a pulse duration of $60\ \mathrm{fs}$. A p-polarized pump beam ($800\ \mathrm{nm}$) is normally incident onto the sample surface with a spot size of $\sim 500\ \mu\mathrm{m}$ in diameter, while the s-polarized probe beam ($400\ \mathrm{nm}$) is incident onto the excited spot with a spot size of $\sim 200\ \mu\mathrm{m}$ in diameter at a small angle (around $4°$) away from the sample normal to measure the polar component of the Kerr signal. An external magnetic field H_{ext} with various amplitude was applied at an angle of $\theta_H = 60°$ away from the sample normal. The pump fluence was fixed at about $5\ \mathrm{mJ/cm^2}$ and all the measurements were performed at room temperature. Details of the setup geometry diagram can be referred in Chapter 3.

To explore the spin and orbit moments, X-ray magnetic circular dichroism (XMCD) measurements were performed in the I06 station of Diamond Light Source. XMCD is a unique technique that uses X-ray to study magnetism. It offers element-specificity and allows one to identify the origin of the magnetic signal in each material ranging from simple elemental films to complex alloys and compounds. In the 3d transition metals such as iron, cobalt and nickel, the X-ray absorption spectra (XAS) for XMCD are usually measured at the L-edge. This corresponds to the transition of a 2p electron excited to a 3d state by absorbing an X-ray photon. The spin property of the excited electron during the p-d transition is elected by the polarization of the circularly polarized X-ray photon, therefor the difference between the XAS spectra taken with left and right circularly polarized light reflects the difference of density of state of spin up and down in 3d states. Due to the existence of spin-orbit interaction, the 2p core state is split into two levels, the $2p_{1/2}$ and $2p_{3/2}$ states, corresponding the L_2 and L_3 transition, respectively. As the spin-orbit couping is opposite in these two states, the excitation's spin sensitivity is opposite. In our experiments, a circularly polarized X-ray beams incidents to the Au(3nm)/Fe(10 ML)/Cr/GaAs(100) samples at an angle of 60 degrees with respect to the sample normal. The XAS spectra were measured under positive and negative applied fields of $1\ \mathrm{T}$. The data were collected by a Total Electron Yield (TEY)

detector in the analysis chamber.

4.4 TRMOKE results

Fig. 4.6(a) shows the measured transient Kerr signal representing the time evolution of the magnetisation in Au/10Fe/GaAs film. The integers represent the number of monolayers. After a pump laser pulse excitation, an ultrafast demagnetisation is triggered and the anisotropy field suddenly changed which force the magnetisation to precess around a new equilibrium direction. Upon the anisotropy field recovers, the original equilibrium angle is gradually restored and the magnetisation continue to precess for hundreds of picoseconds [52]. This magnetisation precession is visualized as the damped oscillations in TRMOKE scans. Besides the prrecessional motion, an exponential-like background is also measured. This decay, reflecting the recovery of magnetisation and other possible optical effects, e.g. reflectivity change [23], lasts for over $1\ \mathrm{ns}$ and eventually the system returns to the initial state after heat dissipation. To analyse magnetisation precession quantitatively, a phenomenological equation is used to fit the TRMOKE curves

$$\Delta\theta_K \propto \mathrm{A}\exp(-t/\tau)\sin(2\pi f t + \varphi_0) + \mathrm{B}(t), \tag{4.2}$$

where A, τ, f, φ_0 are the amplitude of the magnetisation precession, the relaxation time, the precession frequency and the initial phase, respectively. $\mathrm{B}(t)$ represents the background which is simplified as an exponential decay $\mathrm{B}(t) = \mathrm{B}_0\exp -t/\tau_1$, where B_0 is the amplitude and τ_1 is the decay time. The best fitting curve presented in solid line in Fig. 4.6(a) is in good agreement with the measured data. Fig. 4.6(b)(c)(d) shows the measured magnetisation precessions (the backgrounds are removed) and the corresponding fitting curves in Au/10Fe/GaAs, Au/10Fe/0.5Cr/GaAs and Au/10Fe/2Cr/GaAs, in the same external magnetic field of $7993\ \mathrm{Oe}$, respectively.

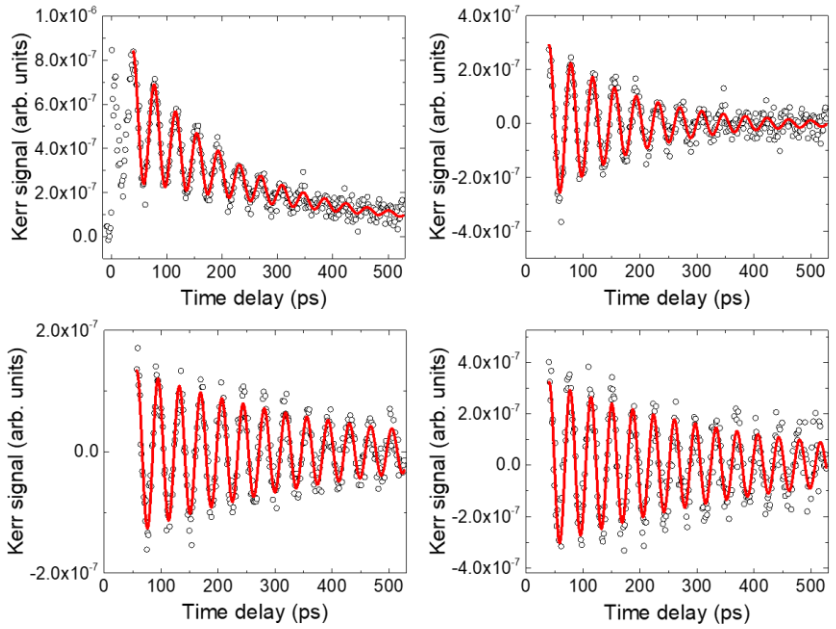

Figure 4.6: (a) raw TR-MOKE curve measured in 10Fe/GaAs with an applied magnetic field of 7993 Oe. (b)(c)(d) magnetisation precession measured with an applied filed of 7993 Oe in the samples 10Fe/GaAs, 10Fe/0.5Cr/GaAs and 10Fe/2Cr/GaAs, respectively. The magnetisation recovery background is subtracted. Solid red lines represent the phenomenological fittings.

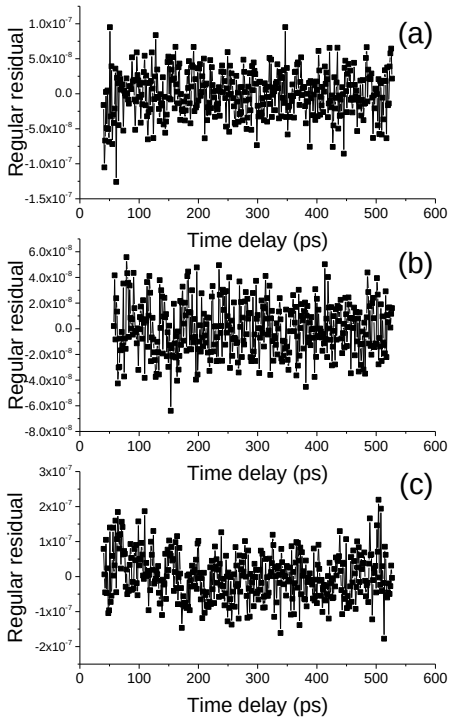

Figure 4.7: (a) (b) (c) residual plots corresponding to Fig. 4.6(b) (c) (d), respectively.

The residual plots of the fitting curves are shown in Fig. 4.7 (a) (b) (c) corresponding to Fig. 4.6 (b) (c) (d), respectively. No other observable signal but the pure noise is shown which indicates a successful fitting to the single damped sinusoidal equation. The comparable low signal to noise ratio may come from two facts. The first is the very thin Fe film whose thickness is only 10 ML. The second is the small Kerr rotation in Fe detected by $400\ \mathrm{nm}$ wavelength laser [182].

The precession frequencies are found of a similar value of $\sim 26.5\ \mathrm{GHz}$ between these three samples, but the relaxation of the magnetisation precession in Au/10Fe/GaAs sample is much faster compared to that of the other two samples with Cr interlayer. The relaxation rates between the two films with Cr interlayer, however, are at a similar level, even though the thicknesses of the Cr interlayers are quite different. In fact, the relaxation rates in the films with Cr interlayer are all in a similar level regardless of the thickness of Cr interlayer (not shown). It is indicated that the magnetic damping is indeed decreased due to the Cr interlayer but this decrease is independent to the thickness of Cr interlayer.

The extracted values of precession frequency f of the samples with different thickness of Cr interlayer are plotted as a function of external magnetic field in Fig. 4.8(a). For a uniform precession around the equilibrium direction with a small cone angle, the precession frequency can be fitted using the expression $f = (\gamma/2\pi)\sqrt{H_1 H_2}$, derived from the Landau-Lifshitz-Gilbert equation when the magnetic damping is much smaller than 1. In this formula, $\gamma = g\mu_\mathrm{B}/\hbar$ is the gyromagnetic ratio, where g, μ_B, $\hbar$ are Landé g factor, Bohr magneton number and Plank constant, respectively; H_1 and H_2 are derived as $H_1 = H_\mathrm{ext}\cos(\theta_\mathrm{H} - \theta_\mathrm{M}) - 4\pi M_\mathrm{eff}\cos 2\theta_\mathrm{M} + H_\mathrm{c}\cos 4\theta_\mathrm{M}$ and $H_2 = H_{ext}\cos(\theta_\mathrm{H} - \theta_\mathrm{M}) - 4\pi M_\mathrm{eff}\cos^2\theta_\mathrm{M} + H_\parallel + H_\mathrm{c} - (H_\mathrm{c}/2)\sin^2 2\theta_\mathrm{M}$, respectively, where $H_\mathrm{c} = 2K_\mathrm{c}/M_\mathrm{s}$ is the four-folder cubic anisotropy field, $H_\parallel = 2K_\parallel/M_\mathrm{s}$ in-plane uniaxial anisotropy field; $4\pi M_\mathrm{eff}$ is the effective demagnetisation field, which is expressed as $4\pi M_\mathrm{eff} = 4\pi M_\mathrm{s} - H_\perp$, where $H_\perp = 2K_\perp/M_\mathrm{s}$ is the perpendicular anisotropy field. The equilibrium angle of the magnetisation is determined from the equation $2H_\mathrm{ext}\sin(\theta_\mathrm{M} - \theta_\mathrm{H}) = 4\pi M_\mathrm{eff}\sin 2\theta_\mathrm{M} -$

$(H_c/2)\sin(4\theta_M)$. The Landé g factor is assumed as $g = 2$ for transition-metal magnets [54] and M_s is obtained from SQUID-VSM measurements. The fitting curves shown in solid lines in Fig. 4.8(a) are in good agreement with the measured frequency and the best fitting parameters are presented in Table. 4.1. The obtained values of in-plane anisotropy constant $K_{\parallel}$ and cubic anisotropy constant K_c are comparable to the reported results [70, 91]. To improve the accuracy of the fitting parameters, more measurements at different magnetic field are needed and the assumption of Landé g factor is also a source of error. The best fitted values of effective demagnetisation field $4\pi M_{\text{eff}}$ are plotted in Fig. 4.8(b) as a function of the thickness of Cr interlayer. The small $4\pi M_{\text{eff}}$ values of pure Fe/GaAs and the films with thin Cr interlayers are attributed to the existence of a perpendicular anisotropy in those samples [183]. This perpendicular anisotropy originated from the Fe/GaAs interface due to an increased degree of localization of electronic states [184]. With the increasing of the thickness of Cr, this perpendicular interface anisotropy becomes weak and the effective demagnetisation field increases.

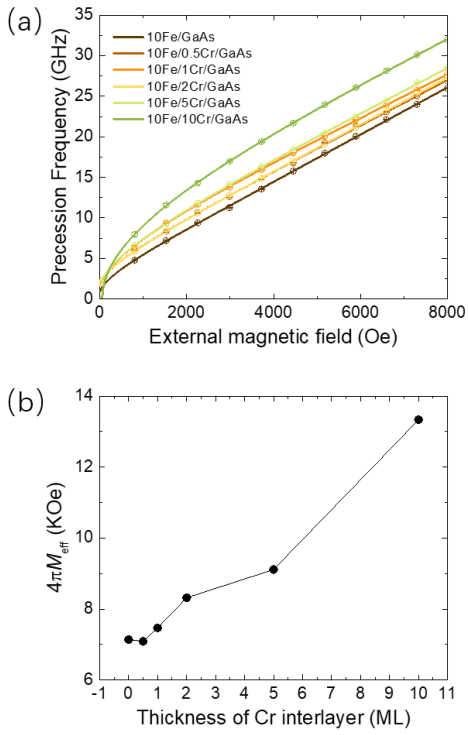

Figure 4.8: (a) precession frequency f as a function of applied field in six samples. Solid lines show the fitting curves. (b) effective demagnetisation field as a function of the thickness of Cr

interlayer.

Table 4.1: Obtained in-plane anisotropy constant $K_{\parallel}$ and cubic anisotropy constant K_c as a function of the thickness of Cr interlayer.

Cr thickness (ML)	$K_{\parallel}(10^5\ \mathrm{erg/cm^3})$	$K_c(10^5\ \mathrm{erg/cm^3})$
0	10.7	10.6
0.5	6.9	6.5
1	1.7	1.6
2	12.4	11.9
5	8.4	8.1
10	4.7	5.0

As plotted in Fig. 4.9, the effective damping constant α_{eff} is obtained as a function of external field using the equation [53, 54, 185]

$$\alpha_{\mathrm{eff}} = 1/2\pi f\tau\,, \tag{4.3}$$

where f and τ are the precession frequency and relaxation time, respectively. For all the samples, α_{eff} decreases with increasing magnetic field to some extent. This field dependence has been reported in many materials and this can be interpreted by the contributions from intrinsic (Gilbert) and extrinsic magnetic damping. The intrinsic damping is independent to the external field and the extrinsic damping is attributed to the magnetic inhomogeneities [58] and multiple-mode spin wave excitations [60]. In our measurements, no other spin wave modes but the uniform precession is detected. Thus, the multiple-mode spin wave excitations contribution should be excluded. The contribution from magnetic inhomogeneities, however, is dominate while the magnetic field is low and this contribution gets suppressed with magnetic field increasing. This has explained the field dependence of α_{eff} and α_{eff} would eventually become close to the intrinsic damping α_0 if the applied field is high enough. Another important effect to be discussed is the spin pumping effect in the FM/NM structures. A interfacial spin current flowing from the FM thin film into an adjacent NM layer results in an

enhanced damping in FM layer and this process is known as spin pumping [186]. This spin pumping effect is determined by the structure of the FM layer [187] and the materials of the NM layer [91]. In our measurements, the capping layer Au is demonstrated has no effect on spin pumping [91, 113], the thickness of Fe layer is unchanged, and the Fe layer is also in the same structure. Therefore, the spin pumping effect is eliminated.

From the obtained effective damping constants, the most striking finding is that the effective damping constant in pure Fe/GaAs film is much larger than that in the films with Cr interlayers. The effective damping constants of the films with Cr interlayers, are of similar values and independent to the thickness of Cr interlayer. This finding is consistent with the observation of the TRMOKE scans shown in Fig. 4.6. The smallest value of α_{eff} measured in pure Fe/GaAs is 0.043 ± 0.001 under the magnetic field of $7993\ \mathrm{Oe}$ while α_{eff} in the films with Cr interlayers is varying from 0.012 ± 0.002 to 0.019 ± 0.004 under the same magnetic field. As discussed above, the effective damping constant is the sum of the intrinsic and extrinsic contributions and the extrinsic contributions can be significantly suppressed with large applied field. Furthermore, the intrinsic damping can be expressed by a sum of the bulk Gilbert damping and the interface contribution [113, 188]. Due to the unchanged thickness and lattice structure of Fe layer, the bulk Gilbert damping contribution should be the same in all the films. Therefore, this large difference of effective damping in the films with and without Cr interlayer comes from the interface damping contribution. Interestingly, the Cr/Fe interface has been demonstrated to enhance the magnetic damping due to the two-magnon scattering effect [91], rather than decreasing the damping. Hence, we speculate that the Cr interlayer itself is not the reason the decrease the magnetic damping but it blocks the GaAs-Fe bonding which is the potential reason.

Comparing our smallest damping value to the reported values of magnetic damping constant of Fe/GaAs filme (0.003 for a $16\ \mathrm{ML}$ Fe) [91], the obtained value of α_{eff} is much larger and this could be explained from two aspects. One is the factor of film thickness: the magnetic damping in ferromagnetic transition metal would increases exponentially with decreasing film thickness [60]. In our measurements, the thickness

of Fe layer is 10 ML which is much smaller than the thickness of 16 ML in Ref. [91]. Therefore, the damping constant should be significantly larger and our value is comparable to the reported value of the 10 ML Fe dots in Ref. [183]. Though the Equation (4.3) only determines an upper bound for the intrinsic damping [54, 139] and the precession ellipticity factor $P = \gamma(H_1 + H_2)/4\pi f$ is ignored in our calculations [185], the feature of our results is not affected by considering the precession ellipticity factor (not shown).

In summary, the effective magnetic damping in the GaAs/Cr/Fe/Au films with various Cr interlayer thickness are obtained using the TR-MOKE methods. It is demonstrated that with the Cr interlayer, the effective damping decreases dramatically. However, the magnetic damping is nearly unchanged with various Cr thickness. We speculate that the Cr layer plays a role to block the GaAs-Fe bonding leading to this observation. Further investigation will be implemented in the following sections.

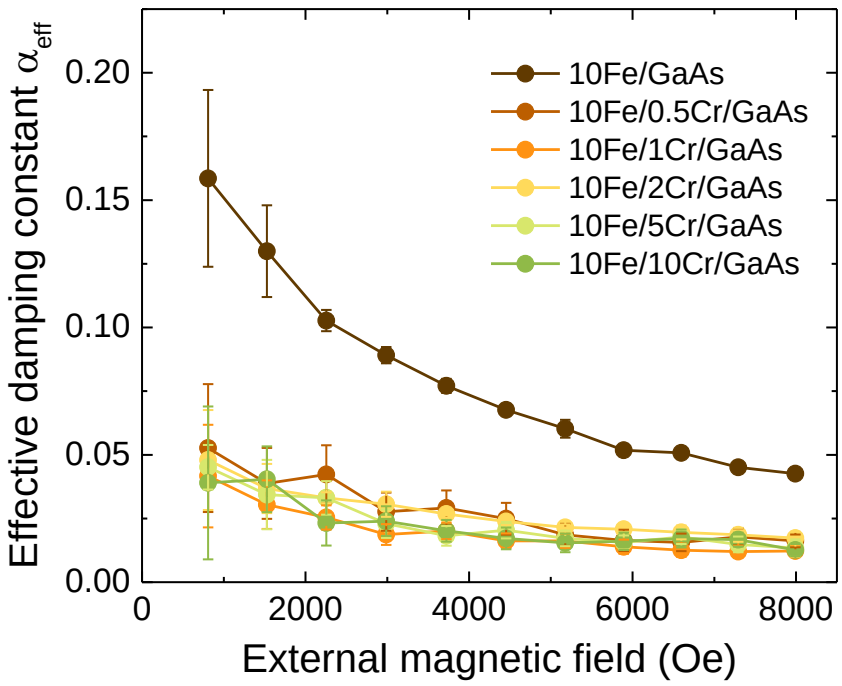

Figure 4.9: effective magnetic damping constant as function of applied field. Lines are guide to eye.

4.5 XMCD results

The XAS and XMCD spectra of Fe L_2 and L_3 edges for the sample Au/10Fe/GaAs is shown in Figure 4.10. In the XAS part, u_+ and u_- represent the absorption coefficients at both positive and negative applied fields. In the XMCD part, the value of $u_+ - u_-$ and the integrated value from $u_+ - u_-$ is shown; these data are used for calculating XMCD sum rules. According to the XMCD sum rules, the orbital (m_{orb}) and spin (m_{spin}) magnetic moments and the ratio (m_{ratio}) of m_{orb} to m_{spin} can be determined from XAS and XMCD spectra using the following equations [157, 189]:

$$m_{orb} = -\frac{4\int_{L_3+L_2}(u_+ - u_-)d\omega}{3\int_{L_3+L_2}(u_+ + u_-)d\omega}(10 - n_{3d}), \tag{4.4}$$

$$m_{spin} = -\frac{6\int_{L_3}(u_+ - u_-)d\omega - 4\int_{L_3+L_2}(u_+ - u_-)d\omega}{\int_{L_3+L_2}(u_+ + u_-)d\omega}(10 - n_{3d})\left(1 + \frac{7\langle T_Z\rangle}{2\langle S_Z\rangle}\right)^{-1}, \tag{4.5}$$

$$m_{ratio} = \frac{m_{orb}}{m_{spin}}, \tag{4.6}$$

where m_{orb} and m_{spin} are the orbital and spin magnetic moments in units $\mu_B/atom$, respectively and n_{3d} is the 3d electron occupation number of the specific transition metal atom. L_2 and L_3 denote the integration ranges. $\langle T_Z\rangle$ is the expectation value of magnetic dipole and $\langle S_Z\rangle$ is equal to half of m_{spin} in Hartree atomic units. According to Chen *et al* [189, 190], we have used the value of n_{3d} for Fe element of 6.61 to calculate all the results.

The detailed values of spin moments, orbital moments, and spin to orbital ratios for Fe are shown in Table 4.2. This table also includes the values of bulk Fe from previous researches. The tendency charts for orbital moment, spin moment and spin to orbital ratio of Fe atoms are shown in Figure 4.11(a), (b) and (c), respectively. Firstly, the spin moment of Fe atoms in the film without a Cr interlayer are as large as $1.96\ \mu_B$, which is similar to the value of bulk Fe ($1.98\ \mu_B$). The orbital moment, however, is much larger than the value of bulk Fe. This enhancement of the orbital moment may be characteristic of a loss of symmetry close to the interface, attributable to qualities of the

substrate surface, resulting in localization of the Fe wave functions [191]. The spin moment and orbital moment of Fe then experienced a decrease with a Cr interlayer. Both of them gradually decreases with increasing the Cr thickness from 0.5 ML to 5 ML. The decreased situation from the orbital moment of Fe atoms is proposed to be correlated to the decreased uniaxial magnetic anisotropy. When the thickness of Cr interlay increases from 5 ML to 20 ML, the orbital moment retains a similar value, around $0.111\,\mu_B$ which is close to the bulk value $0.085\,\mu_B$. The spin moments, however, increases slightly from the 5 ML to 20 ML Cr interlayer. This can be attributed to the decreasing influence from the antiferromagnetic property of Cr interlayer. The orbital to spin moment ratio has the same tendency with the orbital moment, while from the 5 ML to 20 ML Cr interlayer, there is a small decrease caused by the enhancement of the spin moment.

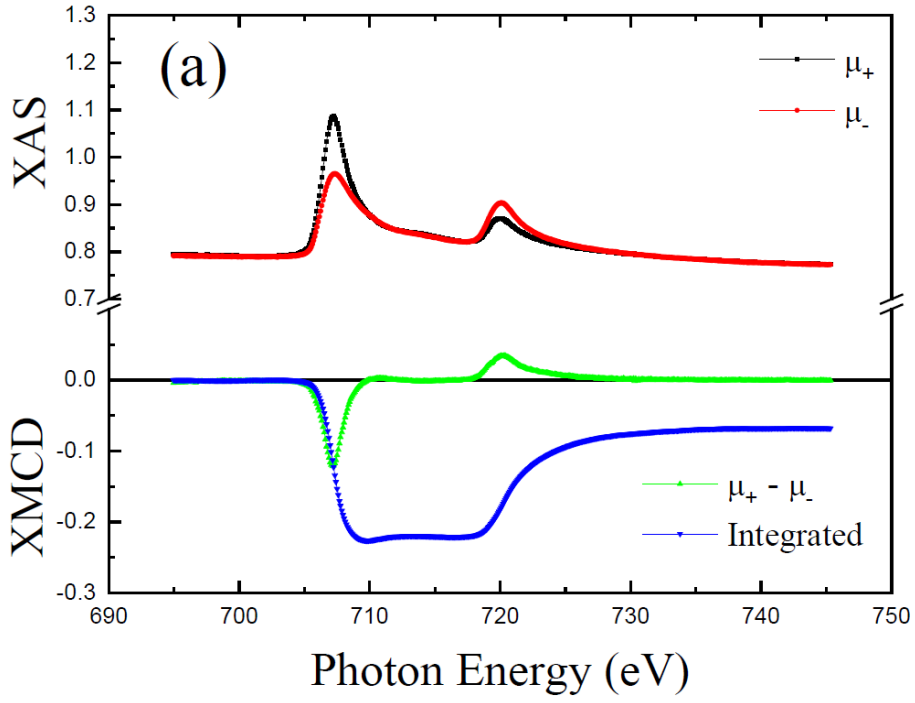

Figure 4.10: XAS and XMCD spectra of Fe atoms at L_2 and L_3 edges in Au(3nm)/ Fe(10ML)/GaAs(100) sample.

Table 4.2: orbital moment, spin moment and orbital to spin ratio of Fe atom from various samples.

Sample	$m_{orb}(\mu_B)$	$m_{spin}(\mu_B)$	m_{ratio}
Au/Fe(10ML)/GaAs	0.201 ± 0.002	1.96 ± 0.02	0.103
Au/Fe(10ML)/Cr(0.5ML)/GaAs	0.173 ± 0.004	1.87 ± 0.02	0.093
Au/Fe(10ML)/Cr(1ML)/GaAs	0.161 ± 0.005	1.76 ± 0.02	0.091
Au/Fe(10ML)/Cr(2ML)/GaAs	0.148 ± 0.003	1.68 ± 0.01	0.088
Au/Fe(10ML)/Cr(5ML)/GaAs	0.111 ± 0.003	1.64 ± 0.01	0.067
Au/Fe(10ML)/Cr(15ML)/GaAs	0.108 ± 0.006	1.69 ± 0.01	0.064
Au/Fe(10ML)/Cr(20ML)/GaAs	0.111 ± 0.008	1.73 ± 0.02	0.063
Bulk Fe [189]	0.085 ± 0.002	1.98 ± 0.02	0.043

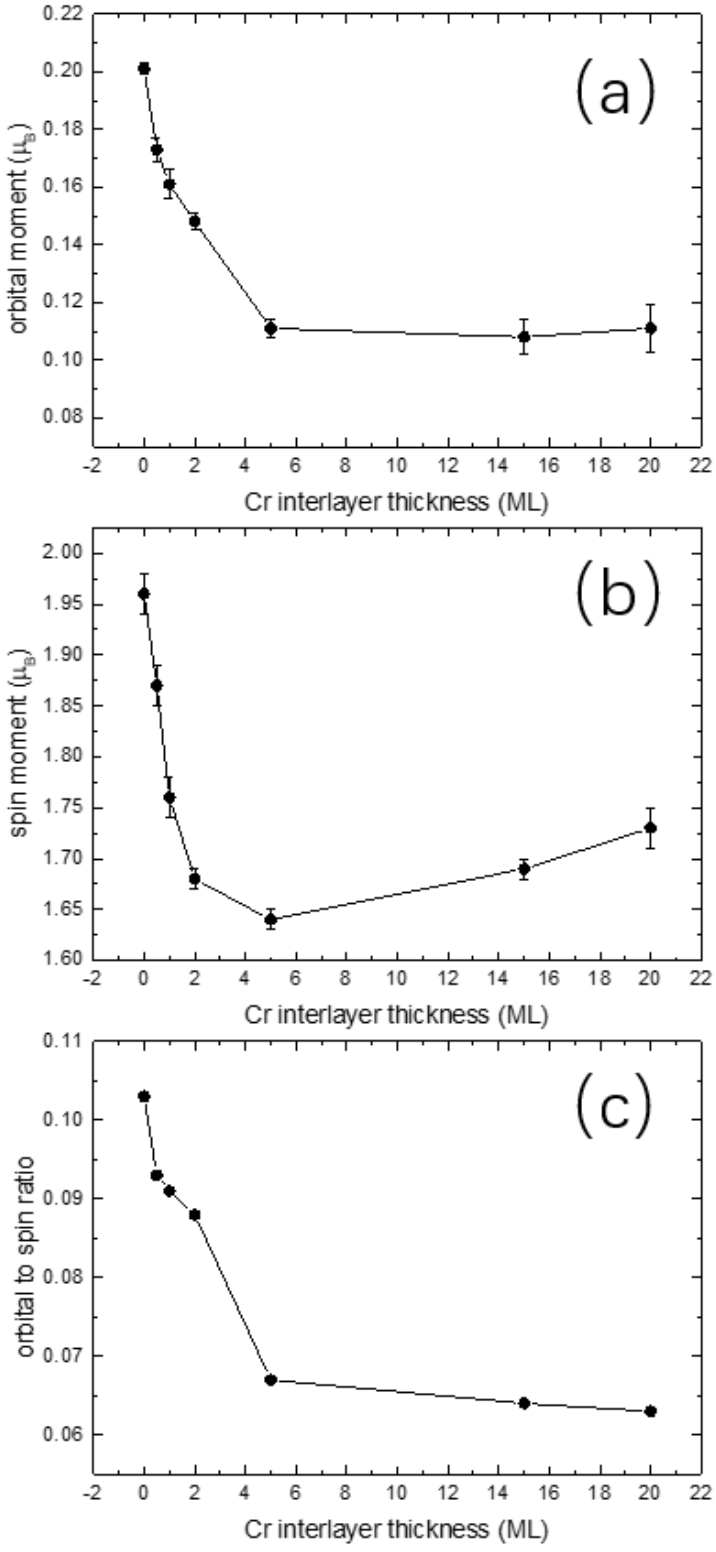

Figure 4.11: (a) and (b) show the orbital and spin moments of Fe atoms as a function of the thickness of Cr interlay, respectively. (c) gives the values of orbital to spin moment ratio.

4.6 Discussion and conclusion

Now the behaviour the magnetic damping and the role of the Cr interlayer between Fe layer and GaAs substrate will be discussed. First, a correlation between uniaxial magnetic anisotropy (UMA) and the orbital moment will be presented. In collaboration with my colleague PhD student Yu Yan in electronics department, two sets of samples are designed and prepared. One of them is the present one using an Au capping layer (Au(3nm)/Fe(10ML)/Cr(t)/GaAs(100)) while the other set of samples have similar structure but the capping layer is replaced by Cr (Cr(3nm)/Fe(10ML)/Cr(t)/GaAs(100)). From VSM measurements, the uniaxial anisotropy constants of both sets of samples are obtained shown in Fig. 4.12(a) & (b) as a function of the thickness of Cr interlayer. The spin moments and orbital moments of both sets of samples are also determined by XMCD measurements, shown in Fig. 4.12(c), (d), (e) & (f). The UMA in the Fe(10ML)/Cr/GaAs structures, with either Au or Cr capping layer, is reduced by the Cr interlayer until the thickness of Cr is 5 ML. The tendency of orbital moments as a function of Cr interlayer in both sets of samples coincides to the UMA, while the spin moments does not. In the samples with Au capping layer, due to the antiferromagnetic nature of Cr, the spin moments of Fe atoms (Fig. 4.12(e)) decrease with increasing Cr interlayer until 5 ML. The reason of the slight restore of spin moment with 20 ML Cr interlayer is still not clear. In contrast, in the samples with Cr capping layer, the spin moments of Fe atoms increase with increasing Cr interlayer until 5 ML. This may be related to a restore of symmetry while increasing Cr interlayer. Similar to Au/Fe/Cr/GaAs structure, a phenomenon of slight decrease of spin moment from 5 ML to 20 ML Cr interlayer is also an open issue. More importantly, the orbital moments of both sets of samples have similar dependence with respect to the Cr interlayer thickness, coinciding with the UMA. Therefore, it is suggested that the existence of the UMA in Fe/GaAs system is related to the enhancement of the orbital moment in Fe atoms. We attribute the UMA and the enhancement of the orbital moment to the Fe-GaAs bonding at interface. When the Cr interlayer is very thin, which is in island-like morphology between Fe and GaAs, this bonding is partially blocked and the UMA and

orbital moments are reduced correspondingly. When the Cr interlayer is grown as a continuous layer at 5 ML, The Fe-GaAs bonding is completely blocked and the UMA no longer exists.

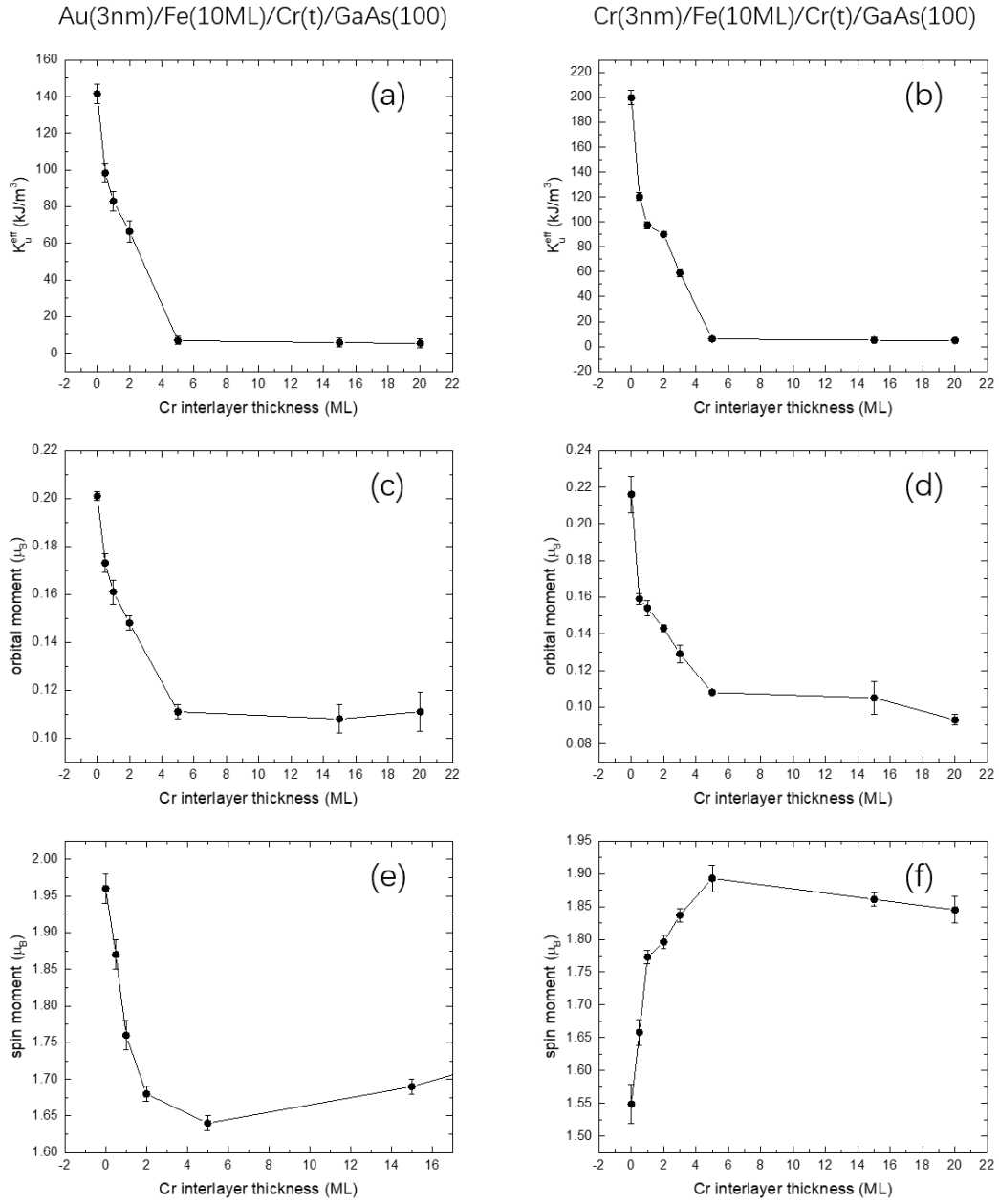

Figure 4.12: (a)(b) shows the effective uniaxial anisotropy constant as a function of Cr interlayer thickness. (c)(d) shows the orbital moments obtained from XMCD measurements. (e)(f) shows the spin moments obtained from XMCD measurements. Left column represents the results of Au(3nm)/Fe(10ML)/Cr(t)/GaAs(100) while right column represents the results of Cr(3nm)/Fe(10ML)/Cr(t)/GaAs(100)

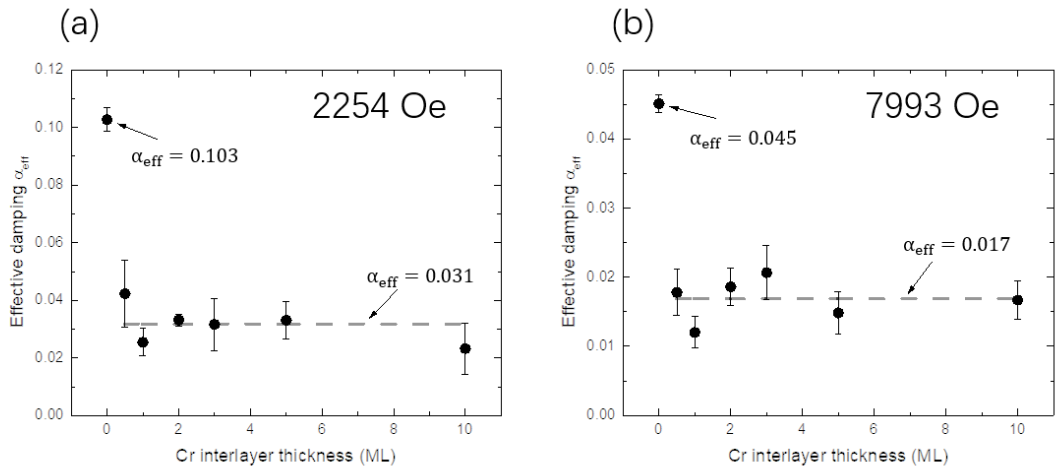

Figure 4.13: the effective magnetic damping constants as a function of Cr interlayer thickness at a magnetic field of 2254 Oe (a) and 7993 Oe (b), respectively.

Back to the magnetic damping, does it share the same underlining mechanism of the origin of the UMA, or, is the magnetic damping directly related to the UMA? To answer this question, the effective magnetic damping constants as a function of Cr interlayer are plotted, at low field region (Fig. 4.13(a)) and at high field region (Fig. 4.13(b)). We can see at both low and high external field, the effective damping presents the same tendency with respect to the Cr interlayer thickness: the effective damping is much larger without a Cr interlayer than that with Cr interlayer and does not significantly affected by the thickness of the Cr interlayer. At a low external field of 2254 Oe, the effective damping constant of the sample without the Cr interlayer is ($\alpha_{\mathrm{eff}} = 0.103$) is nearly three times larger than the average value of the samples with Cr interlayers ($\alpha_{\mathrm{eff}} = 0.031$). Situation at a high external field of 7993 Oe is similar: $\alpha_{\mathrm{eff}} = 0.045$ with Cr interlayer and an averaged value of $\alpha_{\mathrm{eff}} = 0.017$ without Cr interlayer.

To directly investigate the relation between the magnetic damping, anisotropy and the magnetic moments, the effective anisotropy constant from Fig. 4.12(a), the orbital moments of Fe from Fig. 4.12(c), and the effective magnetic damping constant at high applied field from Fig. 4.13(b) are plot in Fig. 4.14 for direct graphical comparison. The anisotropy constant and the Fe orbital moment, as discussed above, have a very similar

behaviour as a function of the Cr thickness. However, it is clear that the behaviour of effective damping has completely different tendency. Both anisotropy constant and the orbital moment decrease gradually from 0 ML to 5 ML Cr thickness while the value of effective damping drops dramatically from 0 ML to 0.5 ML Cr thickness. When the Cr interlayer thickness increases, the effective damping constant stays at a stable level. Therefore, the relations between the anisotropy, magnetic damping and the Fe orbital moment are indicated. In the GaAs/Cr/Fe/Au system, the uniaxial magnetic anisotropy is correlated to the Fe orbital moment but the magnetic damping is not.

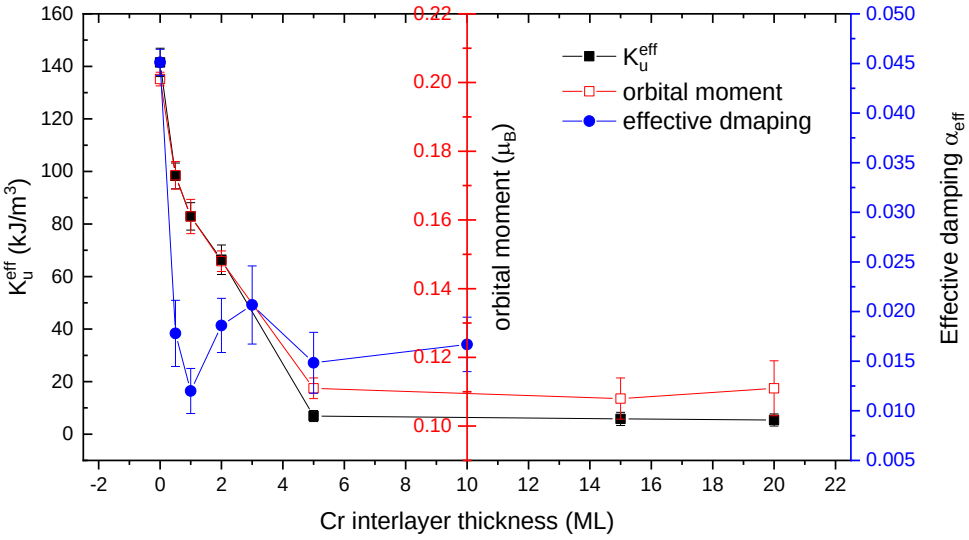

Figure 4.14: the effective uniaxial magnetic anisotropy constant (black), the orbital moment of Fe element (red), and the effective magnetic damping constant (blue) as a function of Cr interlayer thickness. Solid lines are guides to eye.

In summary, in this chapter, the magnetic properties and the magnetic damping are investigated in the GaAs/Cr/Fe/Au system. A series of high-quality films with different Cr interlayer thickness are prepared using MBE. The lattice structures are characterized by RHEED patterns showing the single crystalline structure of Fe films. The uniaxial magnetic anisotropy is obtained from the hysteresis loops measured by VSM. The effective magnetic damping constant is determined from the TR-MOKE measurements and the spin and orbital moments of Fe element are measured from XMCD measurements. It is indicated that the Fe orbital moment plays a significant role in the

UMA because the Cr thickness dependence of UMA constant and Fe orbital moment are almost same. Also, the critical Cr thickness of 5 ML where the UMA disappears corresponds to the RHEED pattern of Cr layer where it completely blocks the GaAs substrate. Therefore, the UMA is suggested to originated form the GaAs-Fe bonding. On the other hand, the magnetic damping has a quite larger value in the film without the Cr interlayer compared to the value of the films with Cr interlayer. And the damping values stays in a stable value when the Cr thickness increases. It is suggested that the GaAs/Fe interface may account to this phenomenon rather than the Cr interlayer. But this interfacial contribution differs from the effect to the UMA because the Cr thickness dependence of effective damping is completely different compared to the UMA and orbital moment. Although the exact physical mechanism of this interface-induced enhancement of the magnetic damping still needs further instigation, this work has provided further insight on the relation between the magnetic damping, UMA and the magnetic moments in the GaAs/Fe system. This would help in controlling the magnetic damping and spin-injection in the FM/SC systems.

Chapter 5 Study on Gilbert damping and electronic structure in Co_2FeAl

It's been predicted that the electronic density of state (DOS) at Fermi level $D(E_F)$ of a material is one of the key factors determining its Gilbert damping constant [7]. This chapter is to obtain experimental evidence to verify this prediction by varying the electronic density of state (DOS) of epitaxial Co_2FeAl thin films by growth under different temperatures. The correlation between the Gilbert damping and DOS at Fermi level will be investigated using time-resolved magneto-optic Kerr effect (TR-MOKE) and angle-resolved photoemission spectroscopy (ARPES).

5.1 Introduction

Magnetization dynamics in ferromagnets can be well described by the phenomenological Landau-Lifshitz-Gilbert equation in Equation 2.25. Study on Gilbert damping is currently a hot topic because it plays an important role in performance of spintronic devices and magnetic storage. In magnetic tunnel junctions (MTJs), which are the basis of spin transfer torque magnetic random-access memory (STT-MRAM), the critical current density for current-induced magnetization switching is proportional to the Gilbert damping constant α [137, 192]. It has been demonstrated in ultrafast magnetization behaviours such as laser-induced demagnetization and magnetization precession that Gilbert damping also plays a key role on determining the relaxation times [52, 61].

Theoretical studies indicated that Gilbert damping has its origin in spin-orbital coupling (SOC) [193] and is proportional to a simple expression of $[\mu_B^2 D(E_F)/\gamma M_S](\xi/W)^2/\tau_E$, where $D(E_F)$ is the density of states at Fermi level, ξ the spin-orbit interaction energy, W the d-band width, and $1/\tau_E$ the electron scattering frequency [54]. This relation has been demonstrated in a variety of magnets, e.g., Fe [148], MnGa [54], CoFe [82] and Heusler alloys [89] by comparing between the

experimental obtained Gilbert damping constant with the theoretical calculated density of states at Fermi level $D(E_F)$. Among these materials, Co-based Heusler alloys (Co_2FeAl) were reported to possess a small value of Gilbert damping varying from 0.001 [89] to 0.004 [57]. Moreover, recently it has been proposed theoretically that the ultrafast demagnetization time τ_M is inversely proportional to $D(E_F)$ [194] and τ_M was proposed to be inversely proportional to damping constant [61]. Even though, the correlation has been suggested by first-principle calculations [195, 196], a direct all-experimental observation of the dependence of damping parameter with respect to electronic structure has not yet been reported to clarify this correlation.

Before we explore the correlation between the $D(E_F)$ and the Gilbert damping, it is necessary to review the studies on the Gilbert damping of Co-based Heusler alloys. Half-metallic ferromagnet (HMF) present a gap in the minority band and thus can be used as perfect spin filters or to enhance the performance of spin-dependent devices as electrons at the Fermi level are 100% spin polarized. The first HMF material predicted by de Groot and collaborators in 1983 was the half-Heusler alloy NiMnSb [197]. Although half-Heusler alloys have attracted a lot of interest, the second family of Heusler compounds, the so-called full-Heusler alloys, have been studied much more extensively due to the existence of diverse magnetic phenomena [198]. The full-Heusler alloys have the type X_2YZ (see Fig. 5.1) and they crystallize in the $L2_1$ structure which consists of four fcc sublattices. The Co-based full-Heusler (Co_2YZ) alloys has been systematically studies from film preparation, magnetic and electronic characterization to ab initio calculations [199-205].

The damping constant of the Co-based full-Heusler alloys have been widely studied. As introduced in chapter 3, the two main experimental methods to measure the damping are TRMOKE and FMR. Besides, first-principle calculations can be applied to obtain the intrinsic damping using the torque-correlation model of Kamberský and co-workers [65, 85]. All of the obtained damping parameters in Co-based full-Heusler alloys using FMR, TRMOKE and first-principle calculations are presented in Table 5.1.

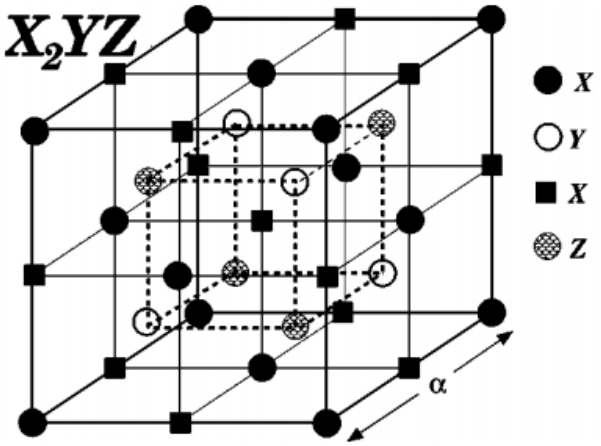

Figure 5.1: Schematic representation of the $L2_1$ structure. The lattice consists of four fcc sublattices [198].

Table 5.1: damping values and experimental methods of Co-based Heusler alloy.

Heusler Alloy	Damping parameters α	Methods	Year
Co_2MnAl [206]	0.007	FMR	2005
Co_2MnAl [105]	0.006	FMR	2006
Co_2MnAl [207]	0.015~0.05	TRMOKE	2007
Co_2MnSi [196]	0.6×10^{-4}	First-principles	2009
Co_2MnSi [208]	0.023	FMR	2007
Co_2MnSi [171]	0.003~0.006	FMR	2007
Co_2MnSi [209]	0.005~0.006	TRMOKE	2010
Co_2MnGe [196]	1.9×10^{-4}	First-principles	2010
$Co_2MnAl_xSi_{1-x}$ [210]	$G = 5.5 \times 10^7$ rad/s*	FMR	2010
$Co_2Fe_xMn_{1-x}Si$ [211]	0.003	FMR	2009
$Co_2Fe_{1-x}Mn_xAl$ [212]	~0.006	TRMOKE	2013
$Co_2FeGa_{0.5}Ge_{0.5}$ [213]	0.008	FMR	2012
$(Co_{50}Fe_{50})_{100-x}Ge_x$ [195]	0.0025~0.0130	FMR	2009
Co_2FeSi [207]	0.008	FMR	2007
Co_2FeAl [89]	0.001	FMR	2009
Co_2FeAl [57]	0.004	TRMOKE	2013
Co_2FeAl [214]	0.0011~0.0068	FMR	2013
Co_2FeAl [215]	0.0011~0.054	FMR	2014
Co_2FeAl [216]	0.003~0.01	FMR	2014
Co_2FeAl [217]	0.0034~0.0098	TRMOKE	2014
Co_2FeAl [218]	0.0044~0.0049	TRMOKE	2014
Co_2FeAl [219]	0.0015~0.0053	FMR	2016
Co_2FeAl [220]	0.0013	FMR	2018
Co_2FeAl [221]	0.0025	FMR	2018
$Co_2FeAl_{0.5}Si_{0.5}$ [222]	0.0025	FMR	2014

*$G = \alpha\gamma M_s$

Among all of these Co-based full Heusler alloys, one can see that Co_2FeAl (CFA) has the smallest value of damping parameter, making it one of the most promising material for application. More importantly, in the earliest study on Co_2FeAl [89], the extremely small value of damping was successfully explained by the proportional relation between the damping constant and the density of states calculated from first principles. Therefore, we choose the Heusler alloy Co_2FeAl to experimentally investigate the correlation between the damping and the electronic structures.

To explore the experimental evidence on how does the $D(E_F)$ contribute to the Gilbert damping, two experimental techniques are needed. The electronic structure can be characterised using angle-resolved photoemission spectroscopy (ARPES). The integrated spectra over a large k space of the measured energy distribution curves (EDCs) can be used to mimic the density of state (DOS) [223]. Meanwhile, Gilbert damping can be obtained by measuring laser-induced magnetisation precession in time domain using time-resolved magneto-optic Kerr effect (TR-MOKE). Heulser alloys Co_2FeAl (CFA) epitaxially grown on GaAs(110) is chosen to be the specimens. Heusler alloys are theoretically predicted to be half-metal in which one spin band has metallic character while the other spin band is semiconductive [197, 224]. Recently, a high spin polarization of 58% at Fermi level has been observed in CFA using spin-resolved angle-resolved photoemission spectroscopy (ARPES) [225]. Its unique magnetic properties of large spin-polarization, large saturated magnetization, and small Gilbert damping make the Heusler alloys a promising candidate for next-generation spintronic device. In this chapter, the Gilbert damping constants of CFA films are investigated by TR-MOKE and their density of state at Fermi level is investigated by ARPES. We find that the effective Gilbert damping varies between the CFA films grown under different temperature. The difference in the effective Gilbert damping is explained by the correlation with the measured DOS. A “shoulder-like” peak is observed in the vicinity of Fermi level in photoemission spectra of two CFA films grown above room temperatures. This peak enhances the DOS at Fermi level and therefore contributes to the increased Gilbert damping in these two samples.

5.2 Sample preparation and XRD results

A series of high-quality CFA films were fabricated in Nanjing University by molecular beam epitaxy (MBE) growth with the base pressure below 3×10^{-9} mbar onto GaAs(110) substrates, whose lattice constant is very close to CFA [226]. Real-time reflection high energy electron diffraction (RHEED) was used to monitor the *in-situ* growth dynamics. The epitaxial relationship is $Co_2FeAl(110)[001]||GaAs(110)[001]$. The thickness of the films is 80 ML grown at a deposition rate ~ 1 ML/min measured by a quartz microbalance. Different growth temperatures of 300K, 500K, and 600K are applied in order to adjust the films' properties [218, 219]. There three samples will be denoted as CFA-300K, CFA-500K, and CFA-600K, respectively, in the following text.

Although we have not implement the XRD measurements on the samples grown on GaAs(110), the CFA films grown on GaAs(001) in the same preparation condition are characterized. Fig. 5.2(a) & 5.2(b) show the RHEED patterns of an as-grown $Co_2FeAl(001)$ film. The sharp streaky lines indicate a flat surface morphology and the growth is smoothly pseudomorphic.X-ray 2θ–ω diffraction pattern of one of the films is presented in Fig. 5.2(d), where Co_2FeAl (200) and (400) peaks can be clearly observed, in addition to the peaks of GaAs substrate. From the diffraction peaks, the lattice constant of the film can be estimated as 5.70 Å, slightly smaller than the theoretical value of 5.727 Å. This suggests that the film is still under compressive strain induced by the GaAs substrate. In theory, a perfect chemically and structurally ordered Co_2FeAl crystal is $L2_1$ phase. Co atoms (golden balls) sit at the eight vertexes of the cubic, and Fe (purple balls) and Al atoms (red balls) occupy the body centre place alternately as shown in Fig. 5.2(c). $L2_1$ phase would be characterized by the peaks of superlattice reflections like (111) and (311) [227, 228]. *B*2 phase would appear if Fe and Al atoms mix with each other. The presence of both (200) and (400) peak indicates that the Co_2FeAl films are in the *B*2 phase [229] in our case. There are no extra peaks apart from the two main peaks, suggesting the single crystal structure of the Co_2FeAl films.

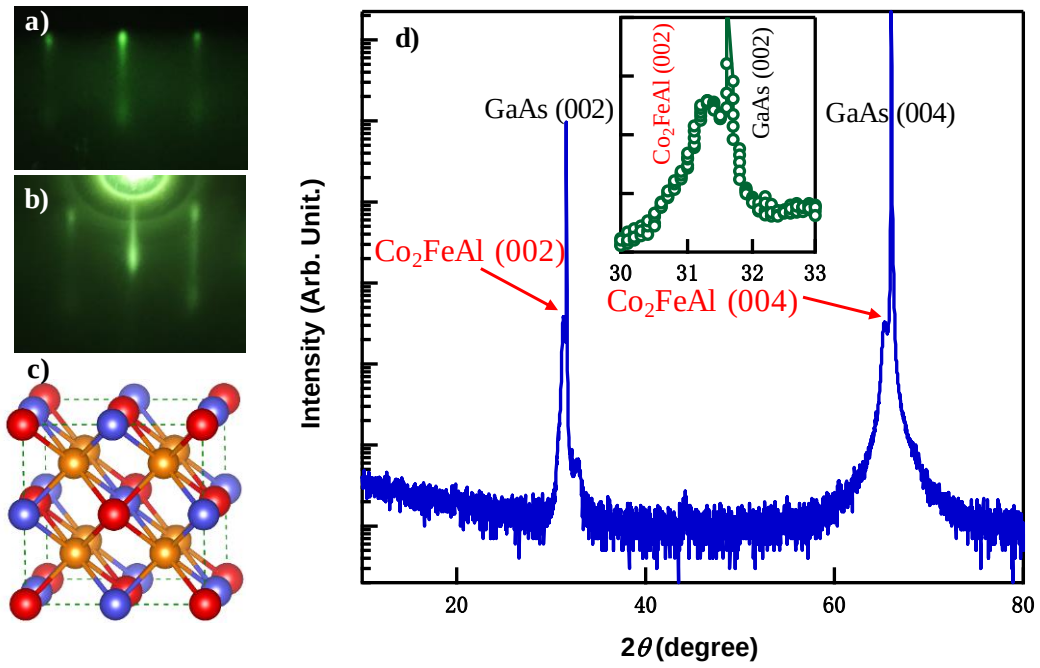

Figure 5.2: (a) & (b) RHEED patterns of a Co_2FeAl (001) film with the electron beam along [110] & [100], respectively. (c) Schematic representation of Co_2FeAl with $L2_1$ structure. The golden, purple and red balls denote Co, Al and Fe atoms, respectively. (d) X-ray 2θ–ω diffraction patterns of a 13-uc-thick Co_2FeAl film grown on GaAs (001) substrate. Top inset is a close view of the Co_2FeAl (002) peak [225].

5.3 VSM, ARPES and TRMOKE measurements

After film deposition, the samples were transferred into the ARPES chamber without breaking vacuum and the photoemission measurements were performed in-situ using Helium lamp with 21.2 eV photons. The energy and angular resolutions were 30 meV and $0.06°$, respectively, and the spectrometer is fixed at a large acceptance angle ($\pm 15°$), which covers the complete Brillouin zone. A 2 nm Al capping layer were deposited upon the films to protect the films from oxidation before being transferred out from the high vacuum chamber. Then TR-MOKE measurements were implement using a pulsed Ti: sapphire regenerative amplified laser with a central wavelength of 800 nm, a repetition rate of 1 kHz, and a pulse duration of 60 fs. The schematic diagram of the geometry of the TR-MOKE setup is shown in Fig. 5.2. The p-polarized pump beam (800 nm in red) is normally incident onto the sample surface with a spot size of $\sim 500\ \mu m$ in diameter, while the s-polarized probe beam (400 nm in blue) with a spot

size of $\sim 200\ \mu m$ is incident onto the same area at a small angle of about $4°$ away from the sample normal to sense mainly the perpendicular component of the magnetization via the Polar Kerr signal. A varying external magnetic field H_{ext} up to about 1 T is applied at an angle of $\theta_H = 50°$ away from the sample normal and presented all the time during TR-MOKE measurements. θ is the angle between magnetization direction in equilibrium and the sample normal. The pump fluence is set at 20.4 mJ/cm^2 and all measurements are performed at room temperature [53].

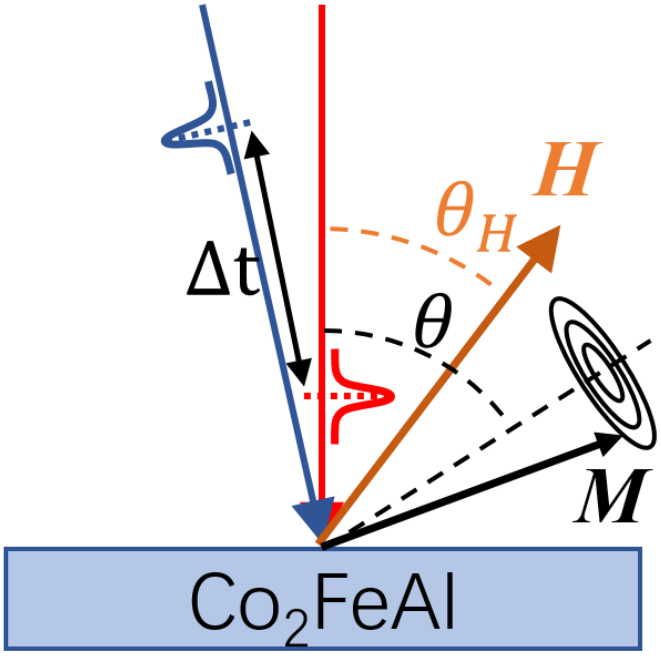

Figure 5.3: Schematic pump-probe TR-MOKE geometry.

The in-plane hysteresis loops of the Co_2FeAl films were measured by a vibrating sample magnetometer (VSM) as shown in Fig. 5.3. A very small coercive field less than 20 Oe is observed. The saturation field is around 500 Oe ensuring the applied field can reset the magnetization in pump-probe measurements. From the hysteresis loops measured along $0°$, $45°$, $90°$ with respect to [001] direction, no distinct in-plane anisotropy is presented.

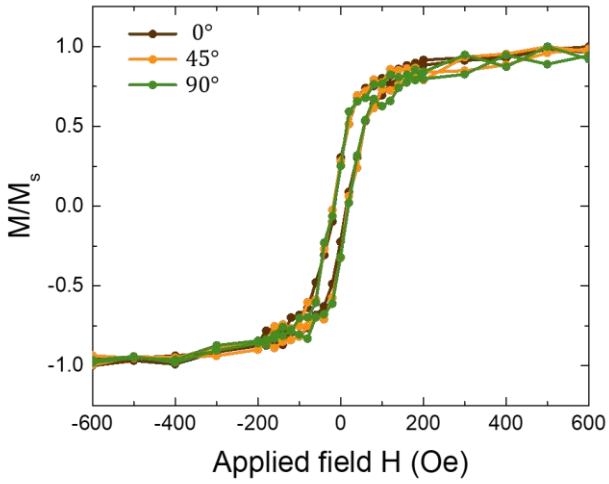

Figure 5.4: in-plane hysteresis loops measured along 0°, 45°, 90° with respect to [001] direction using VSM.

5.4 TR-MOKE results

Two TR-MOKE time scans of sample CFA-300K measured in two magnetic fields with the same field strength of 9687 Oe but in opposite directions are shown in Fig.5.5. The oscillations in both curves correspond to the laser-induced magnetic precession and the difference between the phase of the oscillations is exactly equal to π. The initial rapid change in Kerr signal within the first ps after the pump excitation is a typical ultrafast demagnetization due to a transient rising in electron temperature and a photon-electron-spin interaction. Then the magnetization starts to recover when electron/spin temperature starts to cool down by transfer energy/angular momentum to lattice. Meanwhile, a sudden change in the effective magnetic anisotropy field due to laser heating defines a transient new magnetization equilibrium direction, which acts effectively as a transient torque exerted on the magnetization. This torque forces the magnetization precess towards the transient new equilibrium direction which is gradually back to its original direction upon the fully restoring of the anisotropy and the magnetization [52, 139]. One can see the oscillations of the excited precession riding on an exponentially-decay-background in the observed Kerr signal. This background represents the magnetization recovery while the systems temperature cools

down as heat diffused away. The recovery rate is determined by many factors, such as the underlying nanostructure, pump-laser fluence and ambient temperature, etc. [139, 230] and in our measurements the magnetization recovery time is about tens of ps. The non-magnetic optical contribution at zero delay is also observed which is denoted as "dichroic bleaching" effect [27]. The raw TR-MOKE time scans may also include the contribution from the transient reflectivity change [23] which is again non-magnetic.

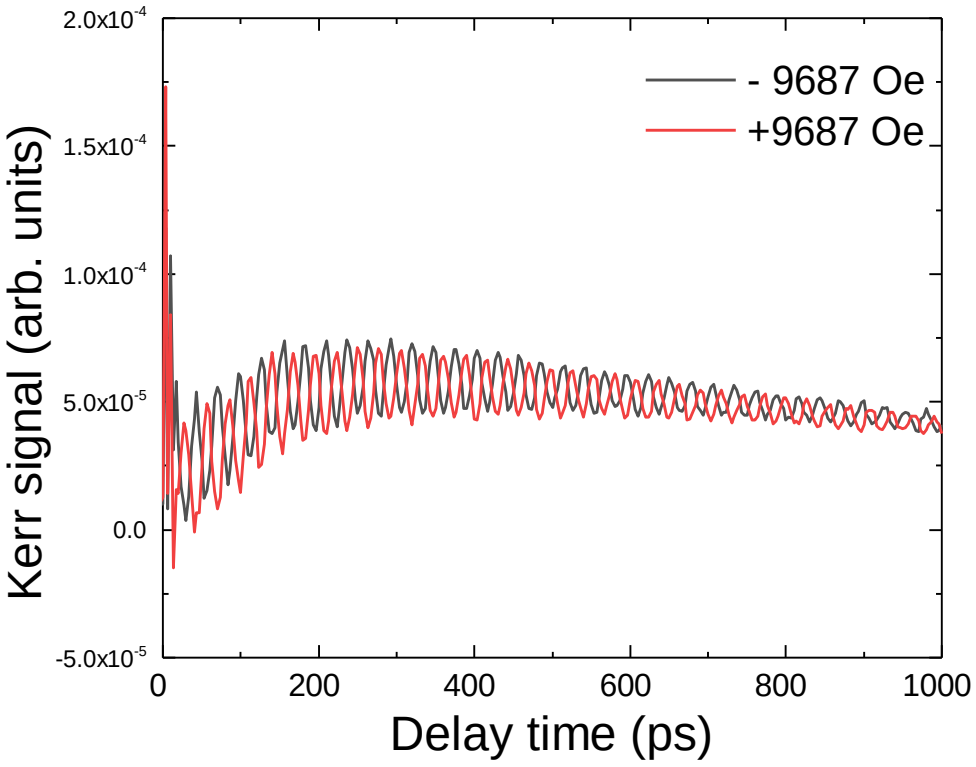

Figure 5.5: raw TR-MOKE time scans of sample CFA-300K measured in opposite magnetic fields of $\pm$9687 Oe.

To eliminate the non-magnetic contributions, a differential TR-MOKE curve (not shown) is obtained by substracting between the time scans measured in the two opposite magnetic fields with the same field strength. The exponential-decaying background representing the magnetization recovery is also subtracted. Then the pure magnetization precession curves are obtained and such magnetization precession curves of three CFA films obtained under the same value of external field (9687 Oe) are shown in Fig. 5.6. Before any further analysis, one can visually observe that the precession relaxation time in CFA-300K is dramatically larger than that in CFA-600K while the CFA-500K is in

the middle.

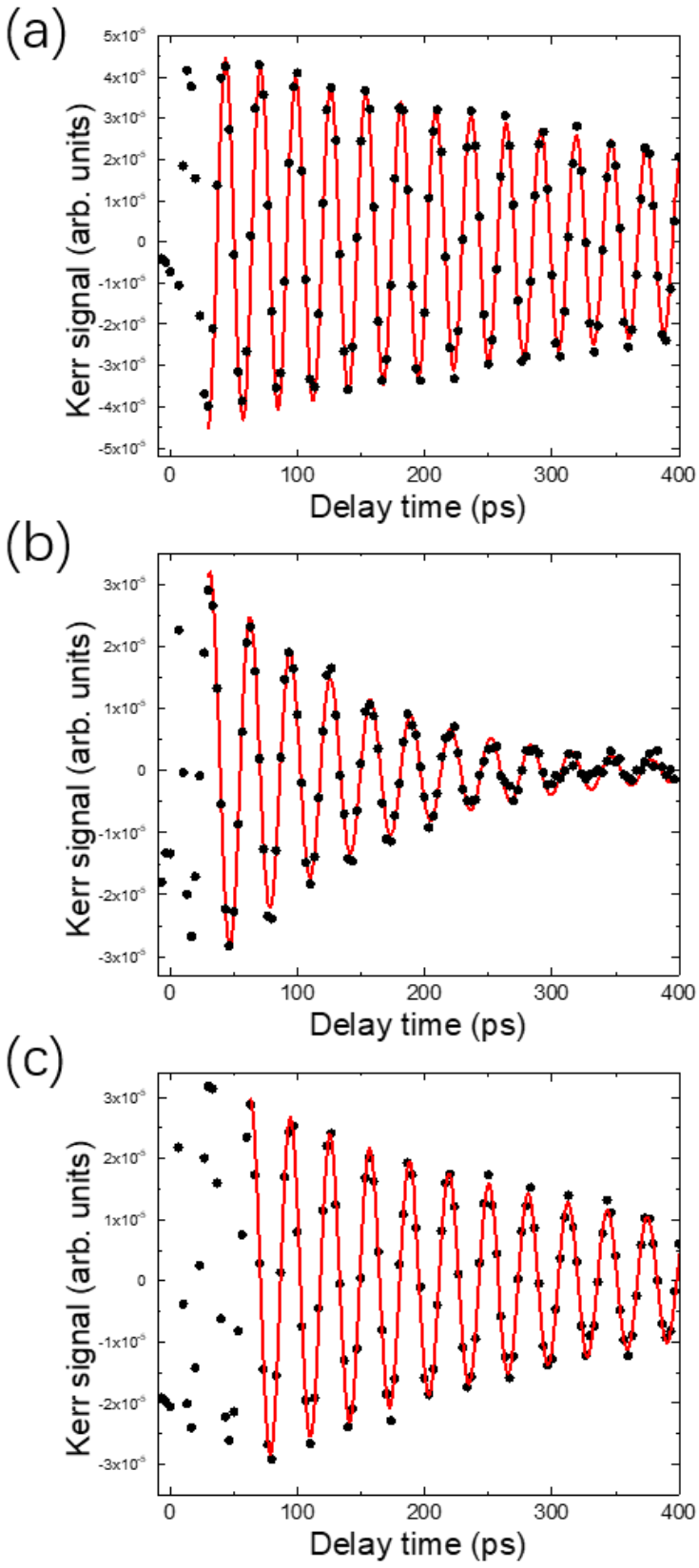

Figure 5.6: Magnetic precession curves of the sample CFA-300K (a), CFA-500K (b), CFA-600K (c), respectively, in the applied field of 9687 Oe. Solid lines represent the best fitting.

To quantitatively analyse the excited precession in the CFA films, a phenomenological damped harmonic function,$a\sin(2\pi ft + \varphi_0)\exp(-t/\tau)$, is applied to fit the oscillations, where a, f, φ_0 and τ are the amplitude, frequency, initial phase, and relaxation time of magnetization precession, respectively. The best fit are shown in red solid curves in Fig. 5.6, which perfectly reproduce the experimental results. The extracted values of relaxation time, τ, and frequency, f, are plotted in Fig. 5.7(a) and 5.7(b) as a function of external magnetic field, respectively. The relaxation times decreases with increasing external magnetic field in all three CFA films. τ is affected by magnetic damping, including intrinsic and extrinsic contributions, and effective fields [231]. In the light of the linearized LLG equations τ is inversely proportional to magnetic Gilbert damping. Therefore difference τ indicates the difference of magnetic damping between these CFA films. The precession frequency f is fitted by the formulas [53, 104] derived from the linearized LLG equations:

$$f = \frac{\gamma}{2\pi}\sqrt{H_1 H_2}, \tag{5.1}$$

$$H_1 = H_{\text{ext}}\cos(\theta_H - \theta) - 4\pi M_{\text{eff}}\cos^2\theta\,, \tag{5.2}$$

$$H_1 = H_{\text{ext}}\cos(\theta_H - \theta) - 4\pi M_{\text{eff}}\cos 2\theta\,, \tag{5.3}$$

where $4\pi M_{\text{eff}}$ is the effective demagnetization field. γ is the gyromagnetic ratio defined as $\gamma \equiv \mathrm{g}\mu_B/\hbar$, where g, μ_B and $\hbar$ are the Lande's g-factor, Bohr magneton and the Planck's constant, respectively. The equilibrium orientation of the magnetization θ is determined by the equation $\sin 2\theta = (2H_{\text{ext}}/4\pi M_{\text{eff}})\sin(\theta - \theta_H)$. The fitted f in solid lines in Fig. 5.7(b) is shown in good agreement with the measured data. The extracted fitting parameter M_{eff} and g are present in Table. 5.2.

Table 5.2: The fitted values of M_{eff} and g

Sample	M_{eff} (emu/cm^3)	g
CFA-300K	1120 ± 24	2.04 ± 0.02
CFA-500K	814 ± 46	1.95 ± 0.04
CFA-600K	660 ± 20	2.08 ± 0.02

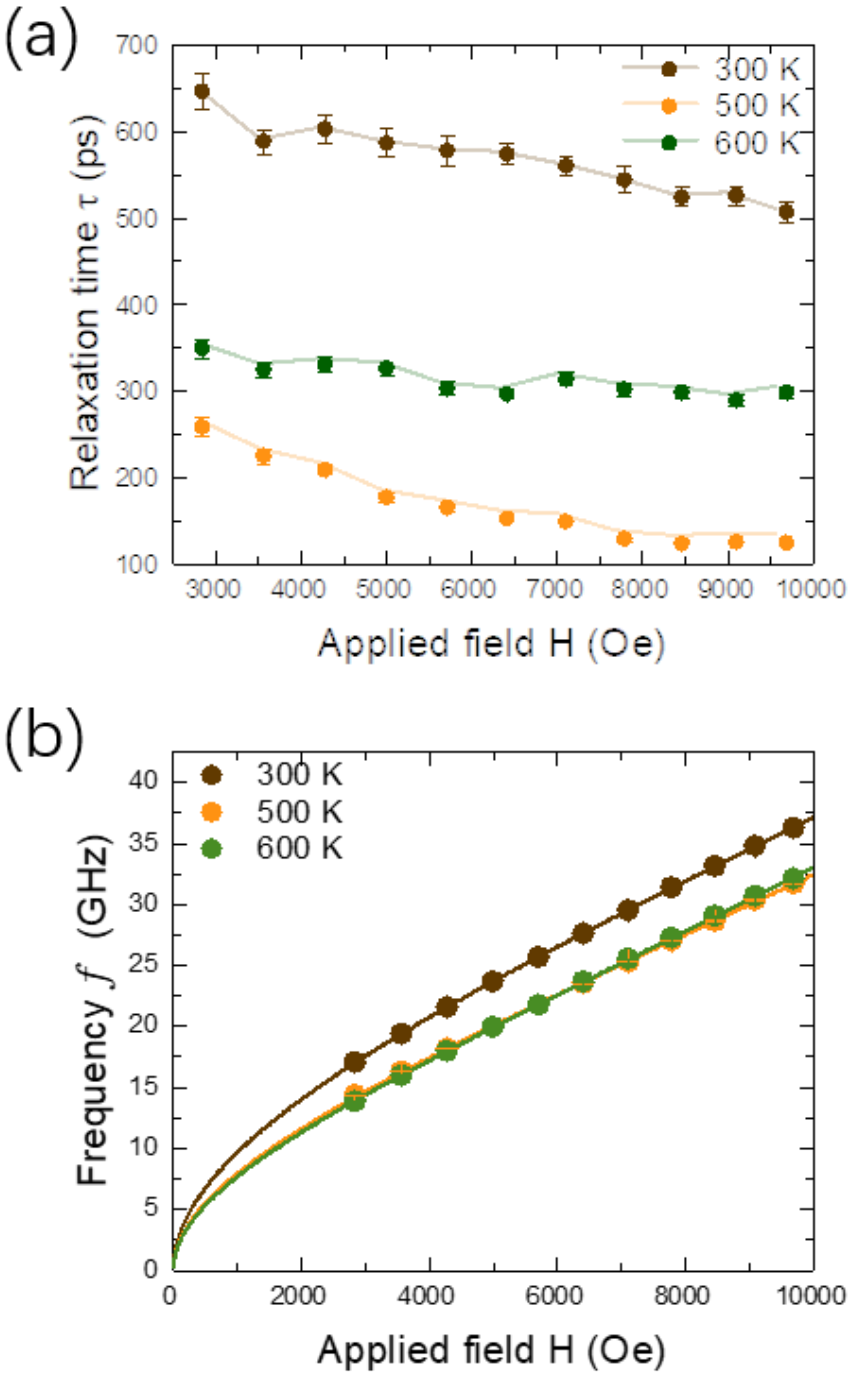

Figure 5.7: (a) Relaxation time τ and (b) Frequency f as a function of applied field. Solid lines show the fitting curves while in (a) is guide to eye.

The effective damping constant, α_{eff}, are derived from the precession frequency and the relaxation time by the formula $\alpha_{\text{eff}} = 1/2\pi f\tau$ [54, 232, 233], and plotted as a function of applied external fields in Fig. 5.8. α_{eff} consists of intrinsic (Gilbert) and extrinsic contributions. The extrinsic damping is attributed to the magnetic

inhomogeneity or two magnon scattering and its contribution is significant at small applied fields [212]. As the applied field becoming significantly large, the effects of anisotropy field and consequently the magnetic inhomogeneity would be expected to be supressed so that the extrinsic damping contribution would be reduced and α_{eff} would become close to the intrinsic value. The α_{eff} shows a significant different field-dependence between these three CFA films. The α_{eff} in CFA-600K stays fairly constant around a large value of 0.042 over the range of the applied fields, which suggests a large intrinsic damping while the extrinsic damping contribution is small. While as, the α_{eff} of the other two samples, CFA-300K and CFA-500K, decrease as the increase of the applied fields. The α_{eff} of the CFA-500K sample at the highest field is 0.04, which is nearly five times larger than the value (0.0086) in the CFA-300K sample. Therefore, the dramatic differences of the substracted α_{eff} among these three CFA films are consistent with the visual impression of the measured precessional oscillation in Fig. 5.6.

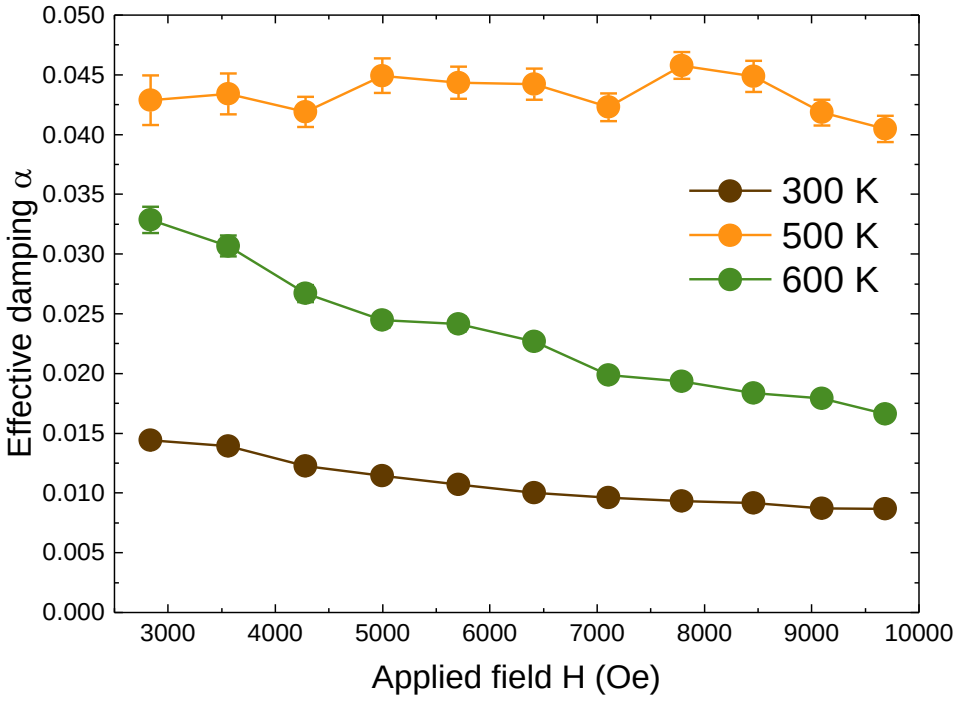

Figure 5.8: Effective magnetic damping as a function of applied field for CFA-300K CFA-500K, and CFA-600K.

Compared to the damping values obtained by other researchers shown in Table 5.1, the smallest damping constant in our measurements of 0.0086 is significanly larger. The reason of the comparable larger damping constant will be discussed from three aspects. Firstly, Mizukami *et al.* proposed that the damping constant decreases drastically with increasing the degree of *B*2 order [89]. This dependence of magnetic damping with respect to the *B*2 ordering is also observed by Cui *et al.*[216]. In our measurements, although the Co_2FeAl present a *B*2 order, the temperature dependence of the *B*2 order is still needed to be investigated. The second potential reason for the larger damping is the GaAs substrate in our study. The damping value obtained in the CFA grown on GaAs substrate is indeed larger [57] than those grown on MgO substrate, which is used in the most studies. This is probably due to the low thermal stability of GaAs compared to MgO making the As atoms intermixing into the CFA films at the interfaces. This speculation can be studied by high-resolution TEM images at the GaAs/CFA interface. The last reason for the larger damping value is the values from TRMOKE are larger than those from FMR [209], which can be seen from Table 5.1. The TRMOKE method measure the effective damping containing the inhomogeneous broadening and other magnon excitation while the FMR method will subtract the extrinsic contribution to obtain the intrinsic damping. Therefore, the magnetic damping constants in our measurements are larger but still comparable to the values reported by other studies considering that value of effective damping are affected by different growth techniques and conditions, the CFA films ordering, as well as the method to determine the parameters [57, 89, 217, 234, 235]

5.5 APRES results

To explore the correlation between magnetic damping and the electronic structure, especially the density of state (DOS) at Fermi level $D(E_F)$, in situ ARPES measurements were performed for the three CFA films before they were taken out of the vacuum. The k-resolved energy distribution curves (EDCs) for the three films are

shown in Fig. 5.9, in which no obvious k-resolved band dispersion is observed. A broad peak at ~ 1.0 eV below Fermi level may come from a mixture of metallic-like Co and Fe components, which is similar to the observation in Co_2MnSi [236]. This peak is significantly suppressed in CFA-300K films compared to CFA-500K and -600K.

The EDCs over a large k space are integrated to mimic the DOS [223]. To qualitatively compared the DOS between the three CFA films, the integrated EDC is normalized to the integral area from Fermi level to 5.5 eV below. In theoretical calculation, the d-bands start at about 5.5 eV below Fermi level [237] and it is assumed that only the d-band electrons contribute to the magnetic properties in CFA. From the normalized EDCs of three samples shown in Fig. 5.10(a), two main features are presented regarding to $D(E_F)$. The first one is the intensity itself at Fermi level: besides the diminished peak at ~ -1.0 eV, the intensity at Fermi level, which can be referred to $D(E_F)$, in CFA-300K is unambiguously smaller than the value in CFA-500K and -600K. The second feature is a "shoulder-like" peak in the vicinity of Fermi level in both CFA-500K and -600K, though the intensities at Fermi level are quite similar in them. This weak but discernible peak is sitting on a large background which is mainly a tail of the -1.0 eV peak. Similar observations were reported in superconductive materials [223, 238]. We apply the method in Ref. [223] to subtract the background from the EDC and a straight line is used for the background as shown in Fig. 5.10(b). The background-subtracted EDCs of CFA-500K and -600K are plotted in Fig. 5.10(c). The peaks are centred around ~ 50 meV and clearly the value of peak in CFA-600K is smaller than the value in CFA-500K.

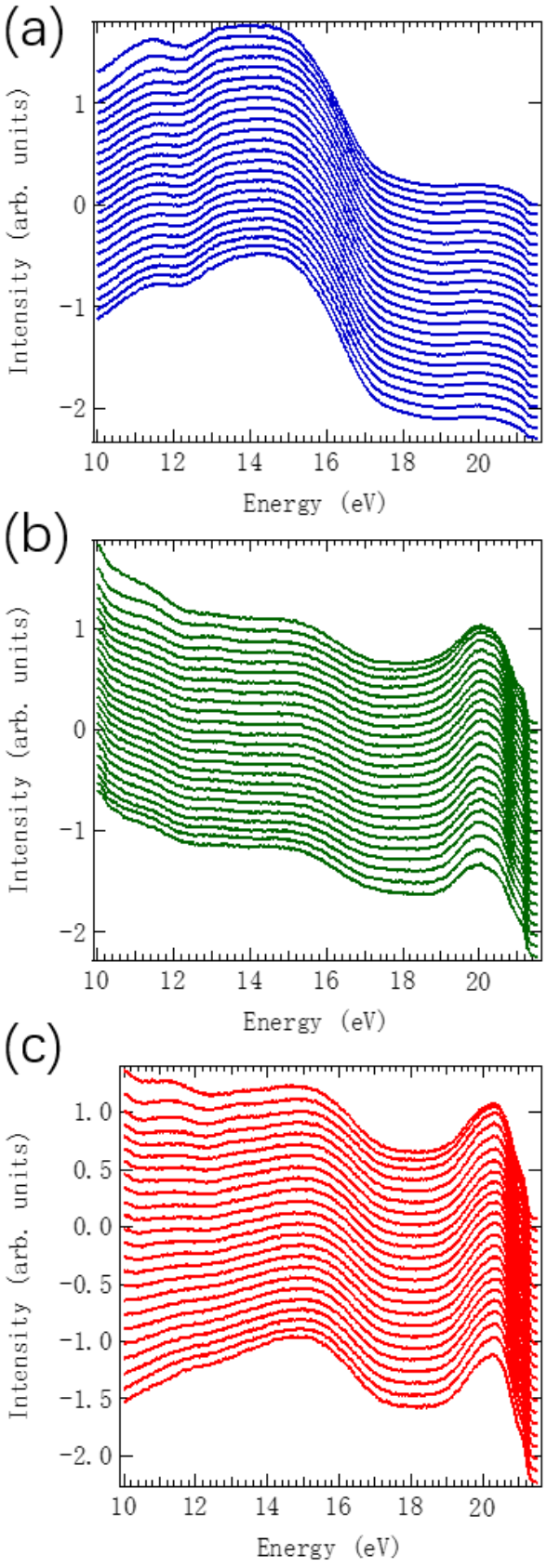

Figure 5.9: K-resolved EDCs of CFA-300K(a), CFA-500K(b) and CFA-600K(c), respectively.

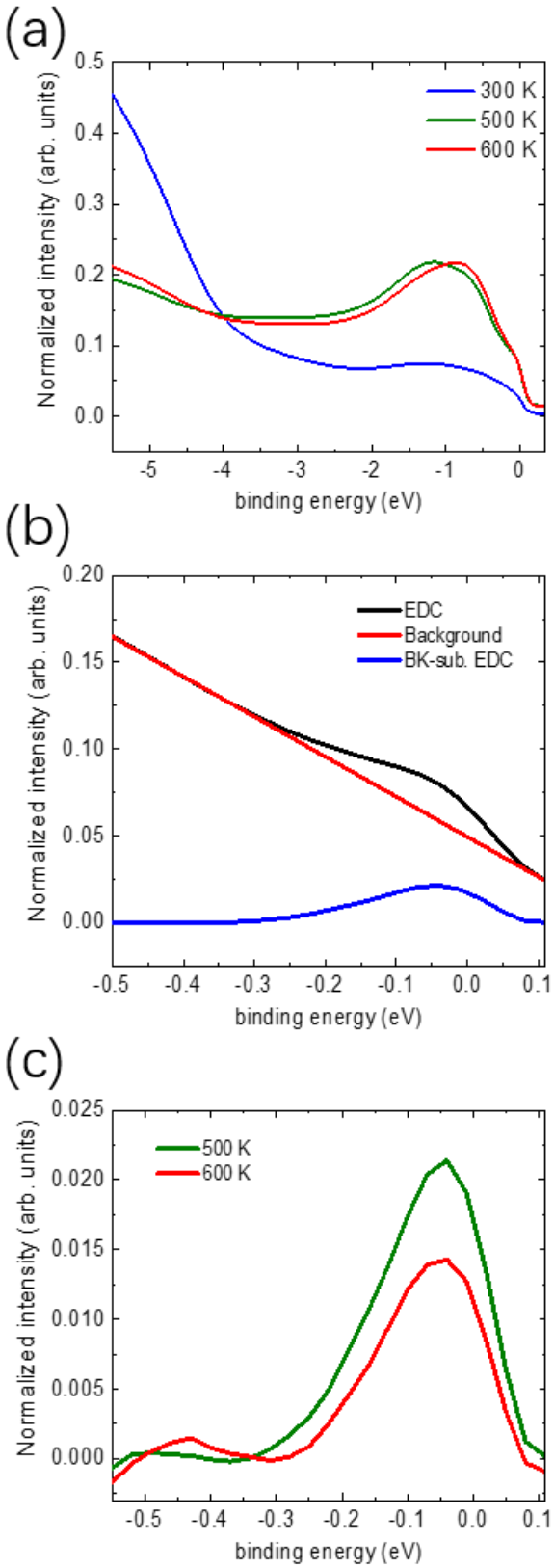

Figure 5.10: (a) normalized integrated EDCs (e) Shoulder-like peak and back-ground subtraction in CFA-500K. (f) EDCs after background-subtracted in CFA-500K and CFA-600K.

5.6 Discussion and conclusion

Now the damping parameters obtained from TR-MOKE measurements can be interpreted by the correlation with the photoemission spectra. The most important finding is the small value of magnetic damping measured in CFA-300K corresponds to the small intensity of EDC at Fermi level, which is referred to the density of states at Fermi level. Compared to CFA-500K and -600K, this suppression of $D(E_F)$ may be related to the diminished peak at $\sim$1.0 eV below the Fermi level. As discussed above, the correlation between magnetic damping and $D(E_F)$ has been predicted theoretically, especially in CFA Heusler alloy. The experimental finding reported here verifies this correlation experimentally. The theoretical expression of Gilbert damping is proportional to $[\mu_B^2 D(E_F)/\gamma M_S](\xi/W)^2/\tau_E$ which could be further verified quantitatively if the spin-orbit coupling parameter ξ can be obtained through X-ray magnetic circular dichroism (XMCD). Together with the observation of $D(E_F)$ by ARPES technique, to manipulate or predict magnetic damping is becoming more promising.

Another interesting finding is the correlation of the magnetic damping with the "shoulder-like" peak observed in the vicinity of Fermi level in EDCs. This small peak indicate that there is an extended flatband just above the Fermi level and the leftover intensity is from the Fermi function cutoff [223]. Moreover, $D(E_F)$ would certainly be enhanced which attributes to the enhancement of magnetic damping in CFA-500K and 600K compared to CFA-300K. The difference of magnetic damping between CFA-500K and 600K can be explained by the different peak intensity of the background-subtracted EDC of the "shoulder-like" peak. This difference between these two films may be also related to the shift of the peak at $\sim$1.0 eV below the Fermi level. This gives further experimental proof of the correlation between $D(E_F)$ and the magnetic damping.

Recently, it is reported that, the spin-gap at Fermi level, measured by spin-resolved photoemission, results in the extremely small damping coefficient in Co_2MnSi Heusler alloy [239]. It seems that the low damping value in Heusler alloy is from the half-

metallic property. Also, a first-principles calculation study on half-metal predicts the consistent dependence between spin-polarization and magnetic damping [196]. These results are different compared to the conclusion in Ref. [89] and ours that the low magnetic damping in Co-based Heusler alloy is from the DOS at Fermi level. However, the spin gap at Fermi level or the high spin polarization would naturally lower the DOS. Therefore, the high-spin-polarization-induced low damping is not in conflict with our results. Importantly, to our best knowledge, studying the magnetic damping using the method of photoemission method has not been reported. In the future work, the exact relationship between magnetic damping, spin polarization and DOS will be investigated systematically in a series of CFA films. And our studies may provide a new direction to study the magnetic damping, especially in half-metals.

In conclusion, we investigate spin dynamics in the Co_2FeAl Heusler alloy grown on GaAs(110) with different growing temperatures by TR-MOKE. The precessional oscillations in the transient MOKE curves in these films present obvious different relaxation rates. The effective magnetic damping constants are extracted and the smallest value is 0.0087 measured in CFA-300K sample, which is consistent with other reported values. Moreover, the electronic structure, especially the density of state (DOS) at Fermi level $D(E_F)$ is investigated by ARPES. The energy distribution curves (EDCs) are integrated over k space to mimic the DOS. The correlation between the magnetic damping and the DOS at Fermi level is qualitatively demonstrated. The small value of magnetic damping is attributed to the small intensity of EDC at Fermi level in CFA-300K film. A “shoulder-like” peak is observed in the vicinity of Fermi level and this peak may explain the enhancement of the effective damping due to an enhanced DOS in CFA-500K film. These results have experimentally suggested the correlation between magnetic damping and $D(E_F)$ as predicted by the theoretic studies and given instructive indication on manipulation of magnetic damping.

Chapter 6 Magnetic damping in half-metallic Fe_3O_4

The magnetic damping is of fundamental and practical interest in spintronics and magnetic recording. Structural defect is expected to be an important factor affecting the magnetic damping. However, the role of the defect is far from clear, especially in magnetite. In this chapter, I have investigated the magnetic damping in precessional spin dynamics in defect-controlled epitaxial grown Fe_3O_4(111)/YSZ films by all-optical pump-probe measurements. The perpendicular standing spin wave (PSSW mode) is observed only in the annealed film without atomic defects. The numerical simulation results confirm the presence of a standing wave in addition to the coherent magnetic precession (Kittel mode). The intrinsic damping constant $\alpha_0 = 0.063 \pm 0.010$ of the defect free Fe3O4 film was found to be strikingly larger than that of the as-grown film of $\alpha_0 = 0.039 \pm 0.004$. The results indicate that the PSSW mode leads to the enhancement of the magnetic damping associated with the emergence of an additional energy transfer channel from the uniform spin precession to the PSSW mode in the defect free Fe_3O_4.

6.1 Introduction

The photo-induced precessional spin dynamics in various magnetic materials has attracted significant attention since the observation of the uniform magnetic precession (Kittel mode) and the corresponding first-order perpendicular standing spin wave (PSSW mode) in Ni films by the all-optical pump-probe technique [52, 240, 241]. After excitation by a femtosecond laser pulse, besides uniform Kittel mode, different spin wave modes can be stimulated including first-order perpendicular standing spin wave (PSSW) and Damon-Eshbach dipolar surface spin waves (DE modes) [60]. Compared to the ferromagnetic resonance (FMR), this photo-induced precessional spin dynamics

is more sensitive to multi-mode spin waves since FMR selection rules allow only the excitations with a net magnetic moment [52, 242]. At the same time, all-optical pump-probe measurement allows the determination of the magnetic Gilbert damping α[55, 243], which is a key parameter for magnetic data recording and the next-generation spintronic memory devices such as Magnetoresistive Random Access Memory (MRAM) [54, 61, 82, 244]. Therefore, understanding and controlling the magnetic damping is of crucial importance.

Among many factors affecting the magnetic damping, structural defect is crucial because it is inevitable when preparing films or devices. It was proposed theoretically that the defects would scatter the Kittel mode into short wavelength spin waves via two magnon scattering, producing a extrinsic contribution to magnetic damping [90]. This extrinsic mechanism was verified by the fact that in NiFe the FMR linewidth increases while the thickness decreases [245]. Also, the magnetic damping was found to be increased by the interfacial defects in the ultrathin Fe/Cr layers [91]. These previous works suggested that with less structural defects the magnetic damping would be smaller. However, the thickness-dependent study in Fe_3O_4/MgO films has shown a strong increase of effective damping from 0.037 up to 0.2 with increasing film thickness from $5\,\mathrm{nm}$ up to $100\,\mathrm{nm}$[246], and the explanation of this effect is still unclear.

As a half metal, Fe_3O_4 is one of the most promising materials for spintronics. Half metals are defined as magnetic materials showing a band gap at the Fermi level for one spin direction. Consequently, only charge carriers of one spin direction contribute to the electronic transport properties [247]. Using the local spin density approximation (LSDA) method, the total density of states and band structure are obtained shown in Fig. 6.1[248]. The LSDA gives a uniform half-metallic ferrimagnetic solution agrees well with previous band structure calculations [249]. These theoretical calculations, therefore, expect a -100% spin polarization at the Fermi level in Fe_3O_4 and a spin polarization of -80% was found near the Fermi energy using spin-resolved photoemission spectra [250]. Both the theoretical and experimental works show a high spin polarization at Fermi level in Fe_3O_4 leading to highly efficient spin injection and

spin transport.

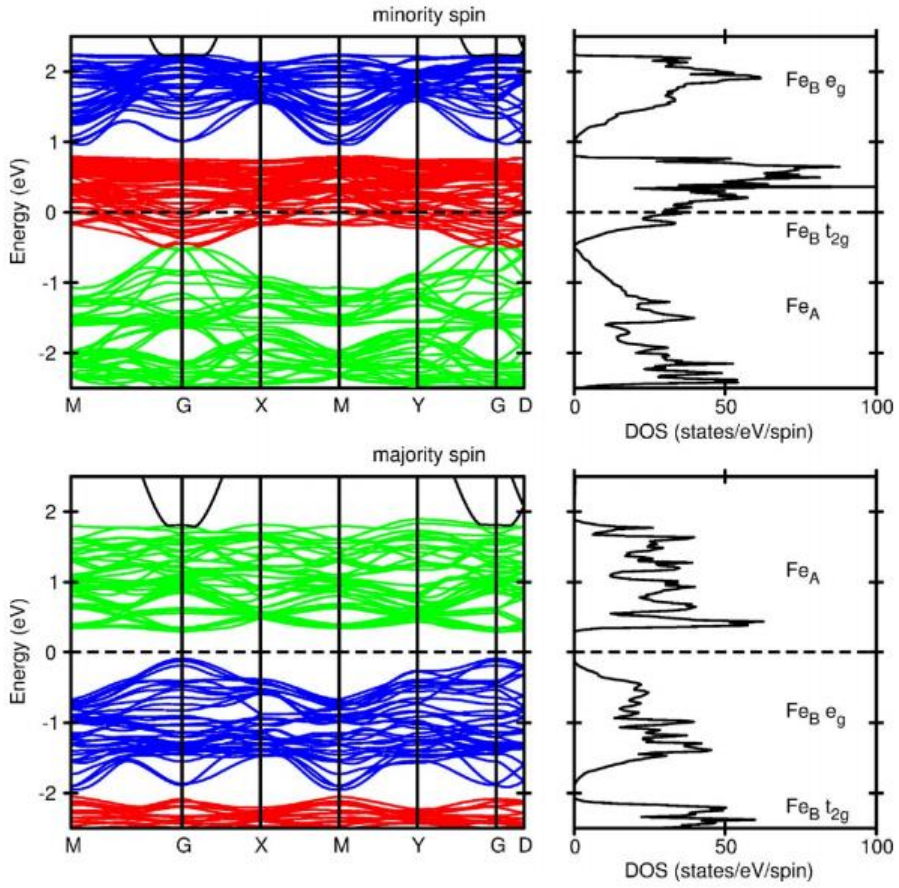

Figure 6.1: total density of states and band structure of Fe_3O_4 self-consistently obtained using the LSDA method. The Fermi level is shown by dotted lines[248].

Magnetite has the inverse spinel cubic structure AB_2O_4 with space group $Fd\bar{3}m$ and lattice parameter $a_c \approx 8.3948$ Å [251]. It contains 6 nonequivalent iron sites, two tetrahedral coordinates (A site), and four octahedral coordinates (B site) in a crystal unit cell, as shown in Fig. 6.2(a) [252]. The A sites are occupied by Fe^{3+} ions, whereas B sites are the mixture of Fe^{3+} and Fe^{2+} ions equally [253, 254]. The X-ray diffraction (XRD) patterns of the Fe_3O_4 films with different thicknesses on Si(100) are shown in Fig. 6.2(b) [255]. Only diffraction peaks of $\{111\}$ crystallographic planes are detected, indicating the oriented growth of these films. It has to be noted that due to the similar structure between magnetite and γ-Fe_2O_3, other characterise methods, like XMCD measurement, are needed to distinguish Fe_3O_4 and γ-Fe_2O_3.

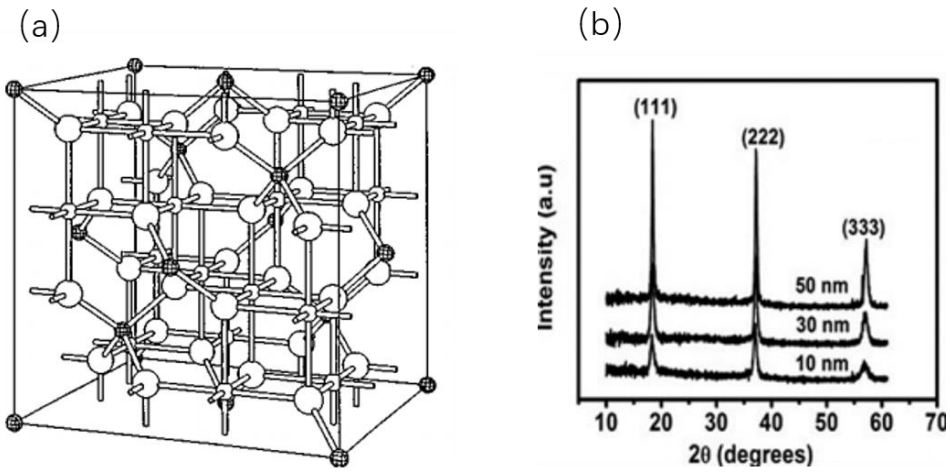

Figure 6.2: (a) Crystal structure of Fe_3O_4[252]. Structure characterization of Fe_3O_4 films with different thicknesses by X-ray diffraction[255].

Fe_3O_4 often contains defects including antiphase boundaries (APBs) and twin defects. APBs are structural defects formed during the film growth originating from the mismatch between Fe_3O_4 films and substrates [256] and their low formation energy means that they are commonly observed in thin film samples [257, 258]. In addition to APBs, it was recently demonstrated that as-grown films can have also significant numbers of twin defects [259]. Because of the presence of antiferromagnetic superexchange interactions across the APBs the magnetic and electrical transport properties are strongly affected, such as negative magnetoresistance (MR) [146, 260] and very high magnetic saturation fields. However, the influence of the defects in Fe_3O_4 thin films has not been investigated and only few studies on the magnetization dynamics and magnetic damping of Fe_3O_4 have been reported [59, 230]. Therefore, the aim of the experiment work in this chapter is focusing on how the structural defects would affect the magnetic damping, especially in the Fe_3O_4 thin films.

To explore the physical nature of magnetic damping and how it is affected by structural defect in Fe_3O_4, a pair of defect-controlled epitaxial grown Fe_3O_4(111) on Yttria-stabilized Zirconia (YSZ) substrate is prepared by PLD growth and annealing. Using time-resolved magneto-optical Kerr effect (TR-MOKE), we find the perpendicular standing spin wave (PSSW) mode only exists in the defect free annealed Fe_3O_4 film, supported by theoretical simulations. More importantly, in contrast to general belief, the magnetic damping of the defect free Fe_3O_4 film was found to be

significantly larger than that of the as-grown film with defects. We also propose a model to describe the coupling effect between the non-uniform PSSW and the uniform Kittel mode.

6.2 Sample preparation and TEM characterization

The Fe_3O_4 films were prepared on Yttria-stabilized Zirconia (YSZ)(111) substrates by pulsed laser deposition (PLD) methods using a KrF excimer laser (wavelength is 248 nm, pulse duration ~20 ns) by our collaborators in Tokyo Institute of Technology in Japan and supplied by Dr. Vlado Lazarov. During deposition, the substrate temperature was held at 300 ℃ in an oxygen partial pressure of 2×10^{-4} Pa. One of the as-grown samples was annealed in an image furnace at 1100 ℃ for 30 minutes in a CO/CO_2 atmosphere with ratio of 1:5000 to reduce the defects and to achieve conditions for stable Fe_3O_4 phase [146].

To compare the structural properties and the defect condition between these two as-grown and annealed films, transmission electron microscopy (TEM) observations have been performed. The TEM was carried out by Dr. Balati Kuerbanjiang. Cross-sectional TEM specimens have been prepared using conventional methods including mechanical thinning and polishing followed by Ar ion milling in order to achieve electron transparency [261]. TEM observations and electron diffraction have been performed using JEOL 2011 operated at 200 kV. It is demonstrated that the annealed Fe_3O_4 film contains a lower density of defects, including APBs and twin defects, compared to the as-grown film. The cross-sectional TEM images of as-grown and annealed Fe_3O_4 films are shown in Fig. 6.3 (a) and (d), respectively. In both films, there is a layer of ~5 nm at the interface between YSZ substrate and Fe_3O_4 film which is oxygen deficient, as discussed in. The thickness of as-grown film and annealed films are ~80 nm and ~50 nm, respectively. The APBs and twin defects are observed in the as-grown film while the annealed film shows a uniform single crystal structure in the Fe_3O_4 layer with drastic reduction of APBs and disorder. Selected area electron

diffraction (SAED) pattern shown in Fig. 6.3(e) demonstrates the single crystal spinel structure of the annealed film. In contrast, the diffraction pattern obtained from the as-grown film (Fig. 6.3(b)) shows the substrate (red rhombus and indices) as well as twinned regions of the Fe_3O_4 film. Atomically resolved HAADF-STEM images further confirm improved crystallinity and the presence of spinel structure as shown in Figs. 6.3(c) and (f). It is interesting to note that besides regular twin structures in Fe_3O_4 as reported before [259], some of the grains separated by an APB also have twinned. The epitaxial relation between the film and the substrate is Fe_3O_4 (111) || YSZ (111) and Fe_3O_4 ($1\bar{1}0$) || YSZ ($1\bar{1}0$) [146]. It is worth to note that the atomic twin boundary is confined to the (111) growth plane and it is non-stoichiometric due to a missing Fe octahedral plane and the first principles calculations show that the local atomic structural configuration of the twin boundary does not change the nature of the superexchange interactions btween the two Fe sublattices across the twin grain boundary [259]. We note that the reduction of the defects in annealed Fe_3O_4 film is also confirmed by the drop of MR (almost an order of magnitude in comparison to as-prepared film), the lower magnetization saturation field, and larger saturation magnetization (M_s~480 emu/cm^3) [259], which is very close to bulk single crystal values of the magnetite.

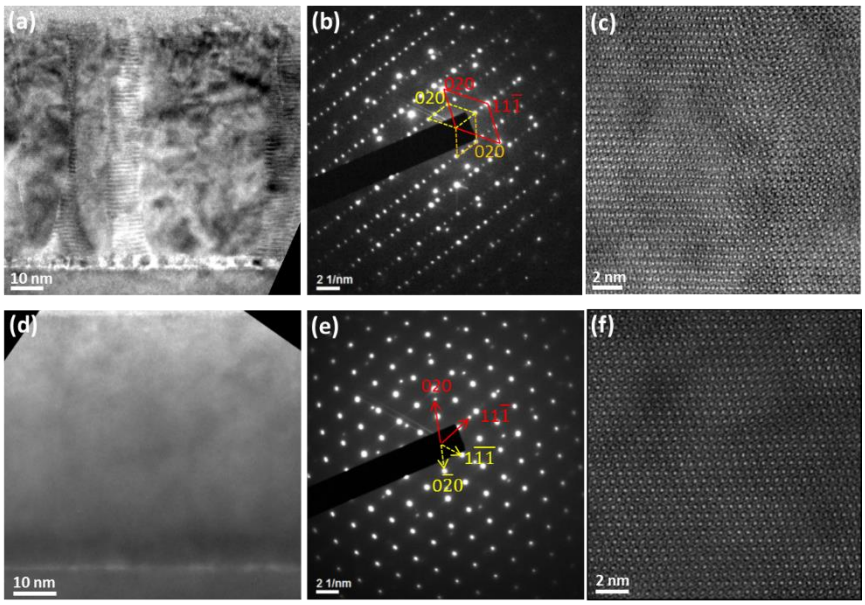

Figure 6.3: (a)(d) TEM images of (a) the as-grown Fe_3O_4/YSZ(111) interface and (d) the

annealed Fe_3O_4/YSZ(111) interface. (b)(e) Selected area electron diffraction (SAED) pattern obtained from both (b) as-grown and (e) annealed films associated with the [110] zone axis of both YSZ and Fe_3O_4. The red rhombus in as-grown film and red arrows in annealed film indicate the YSZ substrate. The two smaller rhombohedral constructions in yellow and orange from the as-grown Fe_3O_4 film indicate to twinned nature of the defects while yellow arrows shows single crystal structure of Fe_3O_4 in annealed film. (c) and (f) are HAADF-STEM images of as-grown and annealed Fe_3O_4 samples, respectively.

6.3 VSM and TR-MOKE measurements

The static magnetic properties are measured by VSM. In both as-grown and annealed Fe_3O_4 films, a very weak in-plane anisotropy is shown in Fig. 6.4(a) and (c) which account for the in-plane anisotropy energy involved in frequency fitting. Compared with the out-of-plane hysteresis loops shown in Fig. 6.4(c) and (d), the sample plane is the magnetic easy plane for both films. The higher saturation field of the out-of-plane hysteresis loop in the annealed film shows a higher anisotropy field which is in good agreement with the fitted anisotropy constants.

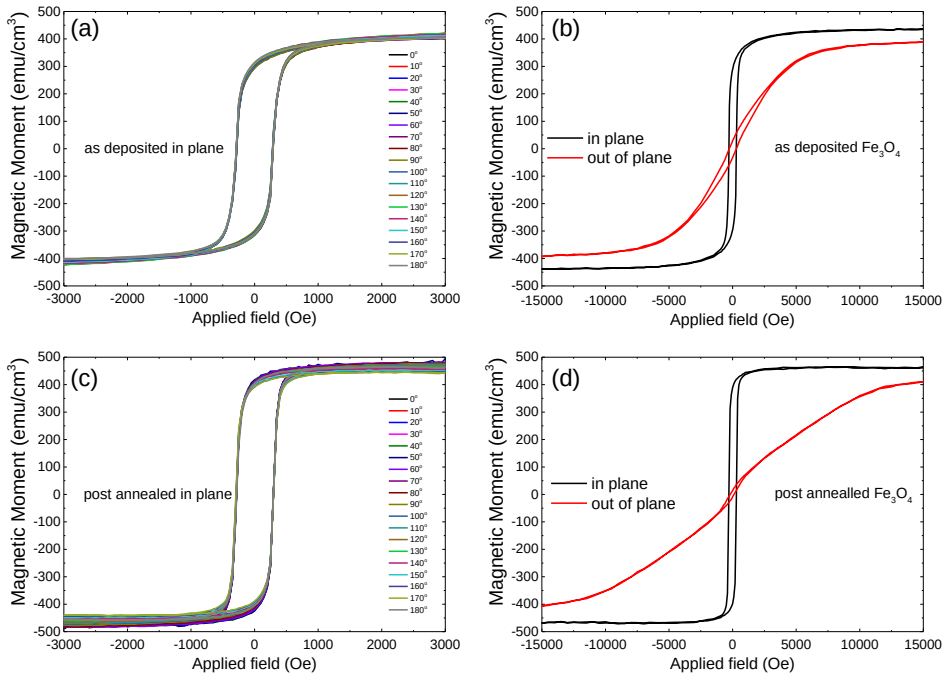

Figure 6.4: Magnetic hysteresis loops measured by VSM. In-plane hysteresis loops of both (a) as-grown and (c) annealed films measured in different orientations. Zero degree represents the

$[11\bar{2}]$ direction. Comparison of out-of-plane and in-plane hysteresis loops in both (b) as-grown and (d) annealed films.

The geometry diagram of our TR-MOKE measurements has been shown in chapter 3. The laser source used in our setup is a mode-locked amplified Ti: Sapphire laser to emit pulses (800 nm) with a duration of $\sim$60 fs at repetition frequency of 1000 Hz. The p-polarized pump beam (red), which is modulated by an optical chopper at a frequency of 333 Hz as reference for a lock-in amplifier, is normally incident onto the sample surface with a spot size of $\sim$500 μm in diameter. The s-polarized probe beam (blue) with 400 nm wavelength is generated through a beta Barium Borate (BBO) crystal so as to be distinct from the pump frequency to avoid signal interference. After passing through the optical delay line, the delayed probe beam is incident onto the excited spot at an angle of around 4° with respect to the sample normal with a spot size of $\sim$200 μm. An optical bridge detection is used to measure the small Kerr signal. During the measurement, a varying external magnetic field H_{ext} up to about 0.5 T is applied at an angle of $\theta_H = 50°$ away from the sample normal direction, shown in Fig. 6.5. All measurements were performed at room temperature.

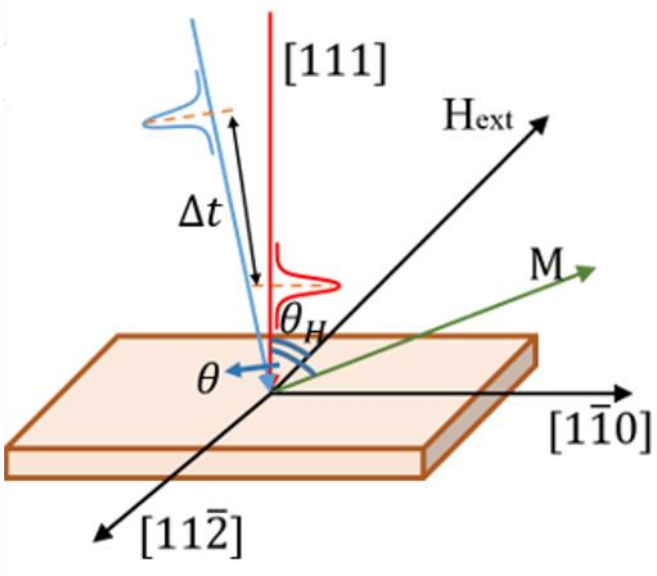

Figure 6.5: Schematic geometry of pump-probe TR-MOKE measurements.

6.4 TR-MOKE results and analysis

The TR-MOKE results for both as-grown and annealed Fe_3O_4 samples are presented in Fig. 6.6(a). and Fig. 6.6(b) under a pump fluence of $5.09\ \mathrm{mJ/cm^2}$. Initially, the magnetization of the film is in a direction determined by the combination of anisotropy field and externally applied field. The initial rapid decrease in magnitude of the magnetization within $1\ \mathrm{ps}$ after the pump pulse excitation is the ultrafast demagnetization resulted from a photon-electron-spin interaction. Meanwhile, the local magnetic anisotropy is reduced due to the thermally induced magnetization fluctuations. The heat-induced changes in saturation magnetization and anisotropy force the magnetization to move to a new equilibrium direction. On cooling after the laser pulse the original values of saturation magnetization and anisotropy are recovered, resulting in a precessional motion of the magnetization towards the original equilibrium directions. This process takes hundreds of picoseconds and during this phase it is possible to determine both the precession frequency and the damping constant.

The external field applied is varied and the field dependence verifies the magnetic precession which is equivalent to ferromagnetic resonance to some extent. To analyze the precessional curves, a phenomenological formula is applied to fit the results:

$$\Delta\theta_K \propto \sum_{i=1}^{2} \mathrm{A}_i \exp(-t/\tau_i) \sin(2\pi f_i t + \varphi_i) + \mathrm{B}(t), \tag{6.1}$$

where τ_i and f_i are the relaxation time and the precession frequency, respectively. The sum of two damped sinusoidal functions is only used to fit the transient magnetization curves of the annealed film in the high field region shown in Fig. 6.6(b).

All the fitting coefficients are listed in Table. 6.1. As the background term $\mathrm{B}(t)$ is a negligible small constant, it is not included in the table. The errors are estimated from the 95% confidence bounds for the fitted coefficients. The estimated errors of the effective damping constants obtained from Equation 6.12 are derived from the fitting coefficients here following the propagation of error. The larger errors of the annealed film compared to the as-grown one, measured in the same experimental condition, are probably due to the high-frequency CAP mode which is not included in the fitting for

simplicity. To justify the necessity to use a sum of two damped sinusoidal function to fit the curves of annealed film measured in the high applied fields, the best fitted curve with a single damped sinusoidal function is presented in Fig. 6.7 for comparison. It can be seen that using a single damped sinusoidal formula, the measured TR-MOKE data under a field of 5401 Oe in the annealed Fe_3O_4 cannot be fitted as good as using a sum of two damped sinusoidal formula. As shown in Fig. 6.7(b), the fitted red line matches the measured data better, especially in the first three periods of the precession. And the values of the R-square and adjusted R-square, which are used to evaluate the goodness of the fit, are significantly larger with a sum of two damped sinusoidal formula, meaning the fitting is much improved with a double damped sinusoidal formula rather than the single one. Therefore, besides the dominating uniform Kittel mode, the extra PSSW mode has to be introduced to fit our measured data.

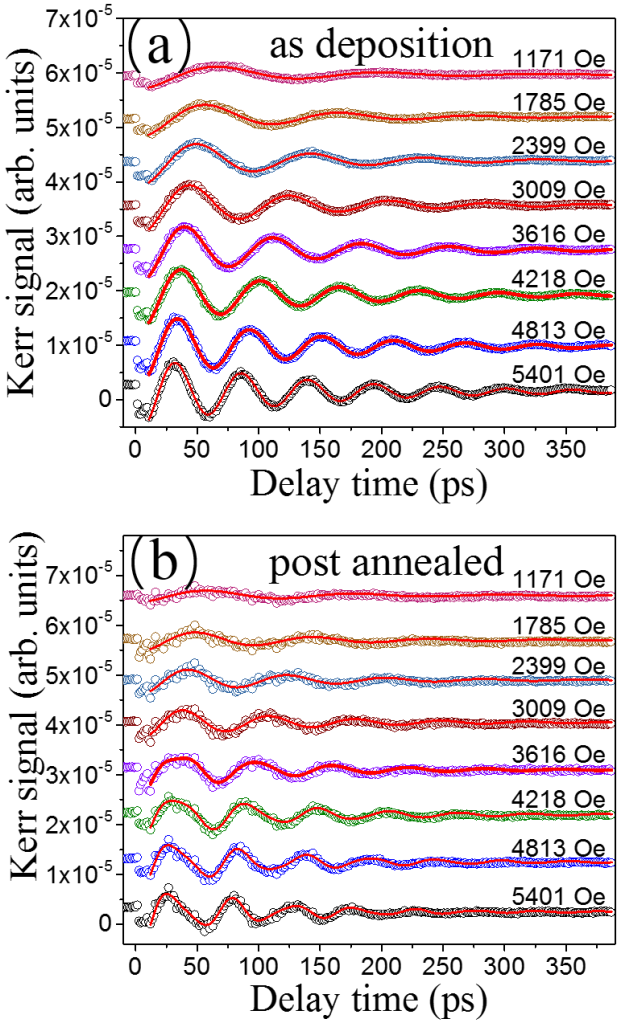

Figure 6.6: Coherent magnetic precession (Kittel) of as-grown Fe_3O_4 (a) and annealed Fe_3O_4 (b). The perpendicular standing spin wave (PSSW) is exclusively observed in annealed Fe_3O_4. The red solid lines show the best fitting according to the Equation 6.1.

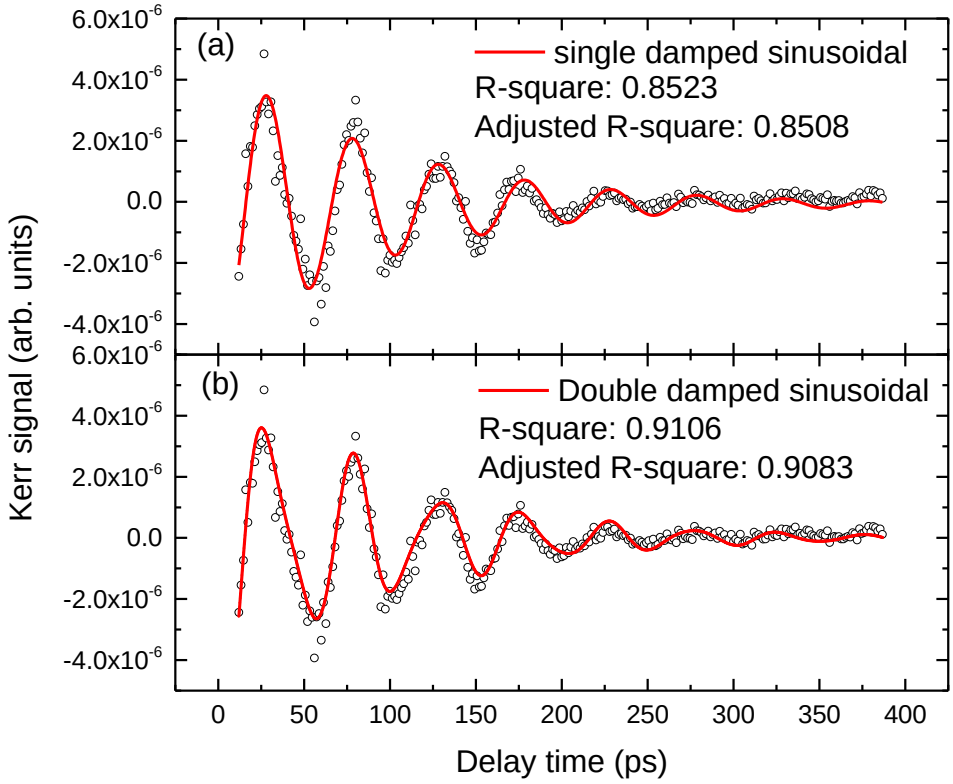

Figure 6.7: Best fitting curves, using (a) single damped sinusoidal formula and (b) double damped sinusoidal formula, for the TR-MOKE results of annealed film under 5401 Oe. The corresponding R-square and adjusted R-square values are presented, respectively.

As shown in Fig. 6.6, one can see clearly that there is more than one oscillation mode. In other cases, a single damped sinusoidal function ($A_2 = 0$) is applied to give a good fit to the curves. φ_0 is the initial phase of magnetization precession and $B(t)$ represents the background accounting for the slow recovery of the magnetization, which is very weak in our measurements. The best fitted lines are plotted in Fig. 6.6(a) and Fig. 6.6(b) by solid red lines showing the fitting function to be a good representation of the experimental results. The first dominating mode ($i = 1$) observed in both films is the magnetic uniform precession mode obeying the Landau-Lifshitz-Gilbert (LLG) equation while the second mode ($i = 2$) which is only present in the annealed film is the first-order PSSW.

Table 6.1: fitting parameters extracted from the phenomenological fitting of the TR-MOKE precessional curves.

Sample	Applied field (Oe)	Kittel mode				PSSW mode			
		$A_1(10^{-6})$	f_1(GHz)	τ_1(ps)	φ_1	$A_2(10^{-6})$	f_2(GHz)	τ_2(ps)	φ_2
Annealed Fe_3O_4	5401	5.01 ± 0.35	20.2 ± 0.1	96.3 ± 7.8	4.10 ± 0.06	1.50 ± 0.40	33.2 ± 0.6	81.3 ± 24.1	3.88 ± 0.24
	4813	4.91 ± 0.34	18.7 ± 0.1	104.3 ± 8.4	4.18 ± 0.06	1.44 ± 0.44	32.2 ± 0.7	74.9 ± 25.0	3.99 ± 0.27
	4218	4.68 ± 0.32	17.4 ± 0.1	109.2 ± 8.6	4.19 ± 0.06	1.47 ± 0.51	30.9 ± 0.9	58.5 ± 21.4	4.23 ± 0.31
	3616	4.41 ± 0.41	16.1 ± 0.1	97.7 ± 9.9	4.11 ± 0.08	1.95 ± 0.97	30.4 ± 1.6	38.2 ± 17.2	4.21 ± 0.39
	3009	3.49 ± 0.30	14.3 ± 0.2	109.2 ± 11.6	4.11 ± 0.07	–	–	–	–
	2399	3.11 ± 0.32	12.5 ± 0.2	108.5 ± 13.5	4.42 ± 0.08	–	–	–	–
	1785	2.43 ± 0.31	10.5 ± 0.2	110.7 ± 17.0	4.53 ± 0.10	–	–	–	–
	1171	1.49 ± 0.21	8.3 ± 0.2	128.8 ± 22.7	4.73 ± 0.11	–	–	–	–
As-grown Fe_3O_4	5401	6.85 ± 0.09	18.5 ± 0.1	120.5 ± 2.0	4.09 ± 0.02	–	–	–	–
	4813	6.83 ± 0.06	17.1 ± 0.1	115.3 ± 1.4	4.15 ± 0.02	–	–	–	–
	4218	6.48 ± 0.06	15.5 ± 0.1	112.9 ± 1.3	4.22 ± 0.02	–	–	–	–
	3616	6.09 ± 0.06	13.9 ± 0.1	111.5 ± 1.5	4.28 ± 0.02	–	–	–	–
	3009	5.47 ± 0.06	12.4 ± 0.1	108.6 ± 1.4	4.34 ± 0.02	–	–	–	–
	2399	4.84 ± 0.06	10.8 ± 0.1	107.0 ± 1.6	4.39 ± 0.03	–	–	–	–
	1785	3.84 ± 0.06	9.2 ± 0.1	104.7 ± 2.0	4.44 ± 0.04	–	–	–	–
	1171	2.76 ± 0.05	7.6 ± 0.1	103.4 ± 2.3	4.50 ± 0.05	–	–	–	–

It is worth to note that the possibility of the DE mode is excluded because of the excitation mechanism and its relevant length scales: film thickness and penetration depth [242]. This surface mode can only be observed when the film thickness is much

larger than the penetration depth because the resulting strong asymmetry will make DE modes the favoured relaxation channel. Although our sample is of $50(80)$ nm thickness, the penetration depth of Fe_3O_4 is greater than 100 nm for a 400 nm wavelength probe beam due to the small conductivity of Fe_3O_4 compared to a transition metal[262], which is larger the film thickness. Furthermore, the frequency term of the DE mode in addition to the Kittel mode, if it exists, can be simply estimated[60] as $f_{DE}^2 = f_{Kittel}^2 + \left(\frac{\gamma}{2\pi}\right)^2$, where k_{DE} is the wave vector and f_{Kittel} is the frequency of the Kittel mode. If we assume the high-frequency mode is the DE mode, the estimated value of k_{DE} is $\sim 5.8\,\mu\mathrm{m}^{-1}$ which gives a wavelength of $\sim 1.1\,\mu\mathrm{m}$. Although this value seems comparable with the wave vectors observed in Ni thin films [60, 212, 242], this surface mode with such a small wavelength is impossible to be detected with a probe size in diameter of 200 μm in our measurements.

The frequency f_1 and the relaxation time τ_1 of the Kittel mode are obtained with different external fields for both samples. It is shown in Fig. 6.8(a) that the field dependence of relaxation time τ_1 is completely different in the as-grown and annealed samples. τ_1 increases with increasing applied field in as-grown Fe_3O_4 while in the annealed sample τ_1 decreases. The PSSW mode (Fig. 6.8 purple square symbols), on the other hand, emerges in the annealed film for sufficiently large applied field. Comparing the relaxation times of these two modes, they exhibit completely different field dependence. The relaxation time of the PSSW mode τ_2 increases dramatically with increasing field while that of the Kittel mode τ_1 decreases. Noting the increase of Kittel mode relaxation time τ_1 with field for the as-grown sample, the corresponding decrease for the annealed sample indicates that energy is transferred from the uniform precession mode to the PSSW mode.

The uniform precession or Kittel mode's frequency as a function of external magnetic field has been fitted according to the frequency-field relationship for ferromagnetic resonance, derived from the LLG equation

$$\frac{d\boldsymbol{M}}{dt} = \gamma \boldsymbol{M} \times \boldsymbol{H}_{eff} + \frac{\alpha}{|\boldsymbol{M}|}\left(\boldsymbol{M} \times \frac{d\boldsymbol{M}}{dt}\right), \tag{6.2}$$

where $\gamma = g\mu_B/\hbar$ is the gyromagnetic ratio while $g = 2.12$[263] is used and μ_B is

Bohr magneton, and α is the Gilbert damping constant. $\boldsymbol{M}$ and $\boldsymbol{H}_{eff}$, respectively, are the vector of magnetization and the effective magnetic field applied on $\boldsymbol{M}$, including the external field, demagnetization field and anisotropy field. Thus, the effective field $\boldsymbol{H}_{eff}$ is equal to $-dG/d\boldsymbol{M}$, where G is the free magnetic energy density and can be written as follows

$$G = G_Z + G_d + G_u + G_c, \tag{6.3}$$

where G_Z, G_d, G_u, G_c represent the Zeeman energy, the demagnetization energy, the perpendicular anisotropy energy and Cubic anisotropy energy given by

$$G_Z = -H_{ext}M_s(\cos\theta_{\mathrm{H}}\cos\theta_{\mathrm{M}} + \cos(\phi_{\mathrm{H}} - \phi_{\mathrm{M}})\sin\theta_{\mathrm{H}}\sin\theta_{\mathrm{M}}), \tag{6.4}$$

$$G_d = 2\pi {M_s}^2 \cos^2\theta_{\mathrm{M}}, \tag{6.5}$$

$$G_u = K_u \sin^2\theta_{\mathrm{M}}, \tag{6.6}$$

$$G_c = \frac{1}{4}K_c(\sin^2 2\theta_{\mathrm{M}} + \sin^2 2\phi_{\mathrm{M}}\sin^4\theta_{\mathrm{M}}), \tag{6.7}$$

Here, θ_{M} and θ_{H} correspond to out of plane orientation of magnetization vector and external field, respectively, with respect to film normal in spherical coordinates which is shown is Fig. 6.8(b). ϕ_{H} and ϕ_{M} are the in-plane angles of external field and magnetization with respect to the $\langle 11\bar{2}\rangle$ direction, while ϕ_{H} is zero in our experiment and consequently ϕ_{M} is zero as well due to symmetry. M_s is the saturation magnetization, K_u and K_c are the perpendicular anisotropy constant and cubic anisotropy constant, respectively. The weak in-plane uniaxial anisotropy energy is ignored[145, 146]. The Kittel mode's frequency is derived from dispersion equation, which is widely used in FMR studies, given by[103, 264]

$$\left(\frac{2\pi f_1}{\gamma}\right)^2 = \frac{1}{(M_s\sin\theta_{\mathrm{M}})^2}\left[\frac{\partial^2 G}{\partial {\theta_{\mathrm{M}}}^2}\frac{\partial^2 G}{\partial {\phi_{\mathrm{M}}}^2} - \left(\frac{\partial^2 G}{\partial\theta_{\mathrm{M}}\partial\phi_{\mathrm{M}}}\right)^2\right], \tag{6.8}$$

Combined with Equations 6.3-6.8, the uniform precession frequency is derived as

$$f_1 = \frac{\gamma}{2\pi}\left[\begin{matrix}(H_{ext}M_s\cos(\theta_{\mathrm{H}} - \theta_{\mathrm{M}}) + 2(K_u - 2\pi M_s^2)\cos 2\theta_{\mathrm{M}} + K_c\cos 4\theta_{\mathrm{M}}) \\ (H_{ext}M_s\sin\theta_{\mathrm{H}}/\sin\theta_{\mathrm{M}} + 2K_c\sin^2\theta_{\mathrm{M}})\end{matrix}\right]^{\frac{1}{2}}, \tag{6.9}$$

The orientation of magnetization vector in equilibrium state of different external field is determined by the following condition

$$\frac{\partial G}{\partial\theta_{\mathrm{M}}} = 0, \tag{6.10}$$

Based on Equation 6.9, the frequency of PSSW mode f_2 which is observed in annealed Fe_3O_4 film can also be fitted by

$$f_2 = \frac{\gamma}{2\pi}\left[\begin{matrix}(H_{ext}M_s\cos(\theta_{\mathrm{H}}-\theta_{\mathrm{M}}) + 2(K_u - 2\pi M_s^2)\cos 2\theta_{\mathrm{M}} + K_c\cos 4\theta_{\mathrm{M}} + 2Aq^2) \\ (H_{ext}M_s\sin\theta_{\mathrm{H}}/\sin\theta_{\mathrm{M}} + 2K_c\sin^2\theta_{\mathrm{M}} + 2Aq^2)\end{matrix}\right]^{\frac{1}{2}}, \quad (6.11)$$

where A is the exchange stiffness constant and $q = \pi/L$ is the wave number of the first-order perpendicular standing spin wave.

The fitted frequency f_1 of the Kittel mode as a function of external magnetic field for both samples is plotted in Fig. 6.8(b) which is in good agreement with the values extracted from damped sinusoidal fitting. The best fitted f_2 as a function of applied field is also plotted in Fig. 6.8(b) and the extracted value of the exchange stiffness constant A is 1.47 ± 0.15 μerg/cm which is comparably close to the reported value as $A = 1.19$ μerg/cm estimated from exchange coupling constant[265]. If we substitute K_u, K_c, L and M_s of as-grown film as well as the extracted A from annealed film into Equation 6.11, the field dependence of the frequency of PSSW in as-grown film is estimated (dashed line in Fig. 6.8(b)). However, this mode is not observed, neither in the TR-MOKE results (Fig. 6.8(b)) nor the corresponding Fourier spectrum (Fig. 6.8(a)). Therefore, the PSSW mode is observed in the single crystal annealed Fe_3O_4 film without defects and is not present in the as-grown film due to magnon scattering induced by a high density of defects, as illustrated in left half of Fig. 6.9. The fact that the PSSW mode is not observed in the low field region (not shown) can be attributed to magnon scattering due to magnetic inhomogeneities.

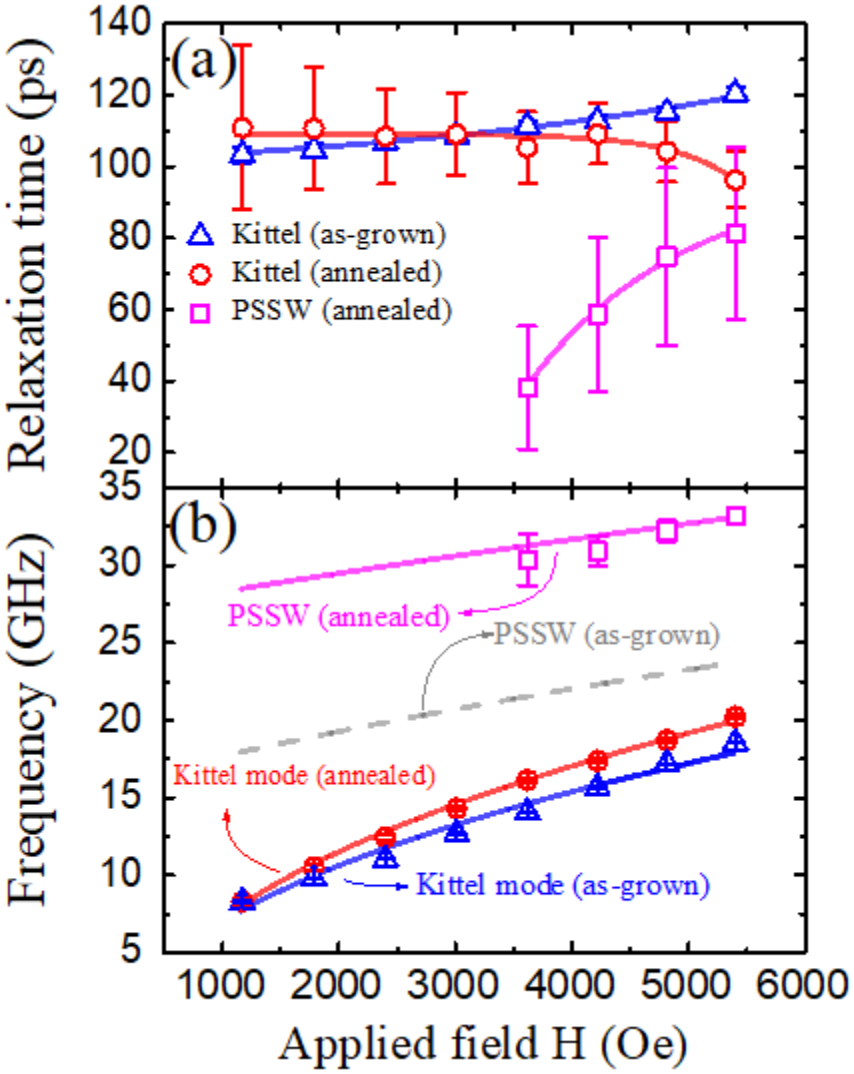

Figure 6.8: (a) Extracted τ_1 of Kittel mode in as-grown Fe_3O_4 film (blue triangle), Kittel mode in annealed Fe_3O_4 film (red circle) and τ_2 of PSSW mode in annealed film (purple square). Solid lines are guide to eyes. (b) f_1 of Kittel mode of both as-grown film (blue triangle) and annealed film (red circle). f_2 of the PSSW mode observed in annealed film is also plotted (purple square). The solid line represents the fitting curves. Dashed line represents the estimated PSSW mode in as-grown film which is not observed.

6.5 Fourier analysis and numerical simulations

Fourier analysis is used to explore the observed multiple-mode oscillations, Fig. 6.9(a) shows the frequency spectrum for the as-grown film, which shows a single uniform precession mode. In Fig. 6.9(b), from the Fourier spectrum of the annealed film, one can observe a main peak referring to the Kittel mode (first mode) and two

extra high-frequency modes. The second mode (red dashed line) is the PSSW mode as previously discussed. Unexpectedly, a very weak third mode (blue dashed line) is found which is field-independent and with a frequency of ~ 95.8 GHz. The origin of the third mode is not from the film itself but from the interface between Fe3O4 film and substrate, namely coherent acoustic phonon (CAP). The origin of the third mode, observed from the FFT spectrum of the annealed film, is not from the film itself but from the substrate, namely coherent acoustic phonon (CAP). This CAP has been reported in GaSb/GaAs heterostructure [266], where the GaSb layer absorbs photon energy so that a strain wave, specifically coherent longitudinal acoustic (LA) phonons, is generated which could travel to the GaAs substrate. The oscillation mode arises from the interference of the probe lights reflected from the surface of GaSb and GaSb/GaAs interface. In our experiment, the Fe_3O_4 layer absorbs photon energy because the energy gap (1.3 eV) [267] in the majority band is just smaller than the pump photon energy (1.5 eV), which may lead to CAP in YSZ substrate. The frequency of CAP can be estimated by the equation, $f = 2nV_s/\lambda$, where n is the refractive index of YSZ substrate, V_s is the speed of LA phonons in YSZ and $\lambda = 400$ nm is the wavelength of probe light. Although the speed of LA phonons in YSZ along $[111]$ direction is not known to the best of our knowledge, the speed of LA phonons along $[100]$ direction is taken as about $8100\ \mathrm{m\ s^{-1}}$ and a refractive index $n = 2.2$ is used [268]. The calculated frequency of the CAP mode in the YSZ substrate is ~ 89.1 GHz which is slightly smaller than the frequency of the third mode (95.8 GHz) and this could be explained by the possibility of using an underestimated value of the speed of LA phonons compared to the speed along $[111]$ direction [269]. Nevertheless, the coincidence between the frequencies of estimated CAP mode in YSZ substrate and the measured third mode suggests that the origin of this high frequency mode is the coherent acoustic phonon generated in Fe_3O_4 layer and then propagating to the YSZ layer. This CAP mode is not observed in as-grown film may because of the diffraction caused by defects.

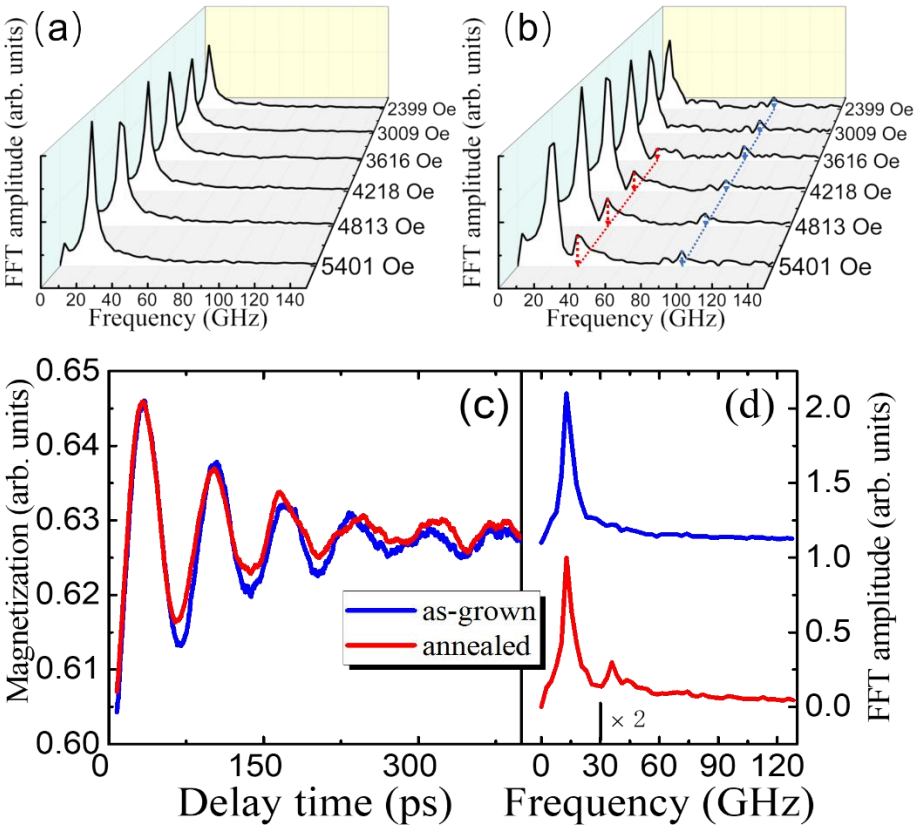

Figure 6.9: Fourier spectrum of as-grown (a) and annealed (b) Fe_3O_4. Kittel mode is recognized as the main peak. In annealed film, the second mode (red dashed line) originate from the perpendicular standing spin wave (PSSW). The field independent high-frequency third mode is coherent acoustic phonon (CAP) mode (blue dashed line) from the Fe_3O_4/YSZ interface. (c) numerical simulation of magnetisation dynamics in as-grown (blue) and annealed (red) Fe_3O_4 thin film. (d) corresponding Fourier spectrums show a single peak in the as-grown film while a second peak is shown in the annealed Fe_3O_4 film.

In further support of the experimental data a model based on the Landau-Lifshitz-Bloch (LLB)[270-273] equation has been used to gain further insight into the cause of the additional peaks seen in the Fourier spectrum. The phenomenological LLG equation, which is usually used to describe the magnetization dysnmics requires a fixed magnetization length for nanoelements at nonzero temperature. However, experimentally, the magnetization can decrease in time upon heating by a laser pulse and recovers gradually. Hence, we use the LLB equation which can naturally describe the effect at elevated temperatures[271]. To model the Fe_3O_4 thin film a Voronoi construction was implemented to simulate the granular structure, with approximately three thousand 10 nm cells in the x-y plane and eight 10 nm cells in the z-axis,

resulting in a system that is $500\ \text{nm}$ by $500\ \text{nm}$ in the x-y plane and $80\ \text{nm}$ in the z-axis, with periodic boundary conditions. The cells that simulate the domain structure of the thin film are strongly exchange coupled comparable with the bulk exchange coupling for Fe_3O_4, resulting in the system acting as a single macro-spin. The restoring applied field was set at an angle of 50 degrees from the z-axis into the y-axis. The system was first allowed to equilibrate at a high temperature of $600\ \text{K}$, at which point the temperature was lowered to $300\ \text{K}$ in a single step, in order to cause the magnetization to return to the temperature dependent equilibrium position, so that the oscillating magnetization could be observed. To simulate the annealed case the exchange between the layers is introduced to account for the removal of the defects.

The as-grown thin film showed significant defects running in the x-y plane, resulting in a layered structure. It is believed that these defects will result in a significant reduction in the inter-granular exchange between the observed layers. This effect is simulated by removing the exchange between the cells in the z-axis and the only exchange between the cells in the x-y plane remains. After the thin film has undergone the annealing process the structure of the thin film is seen to change as the defects are removed. The same set of experiments are undertaken with the annealed thin film to recover the second spin wave mode. Comparing the magnetisation time sequence results of both film, shown in Fig. 6.9(c), it is demonstrated that there is a phase mismatch between these two curves caused by the extra mode in the annealed film. Also, the second peak is observed in the corresponding Fourier spectrum in the annealed film (Fig. 6.9(d)), similar to the experimental results. This result confirms the present of a standing wave moving in the z-axis in addition to the standard Kittel precession moving across the thin film in the x-y plane.

6.6 Magnetic damping and discussion

Now, the effective damping constants α_{eff} are derived from the Kittel mode using [54, 232, 274]

$$\alpha_{\text{eff}} = 1/2\pi f_1 \tau_1 , \tag{6.12}$$

which are illustrated in Fig. 6.10.

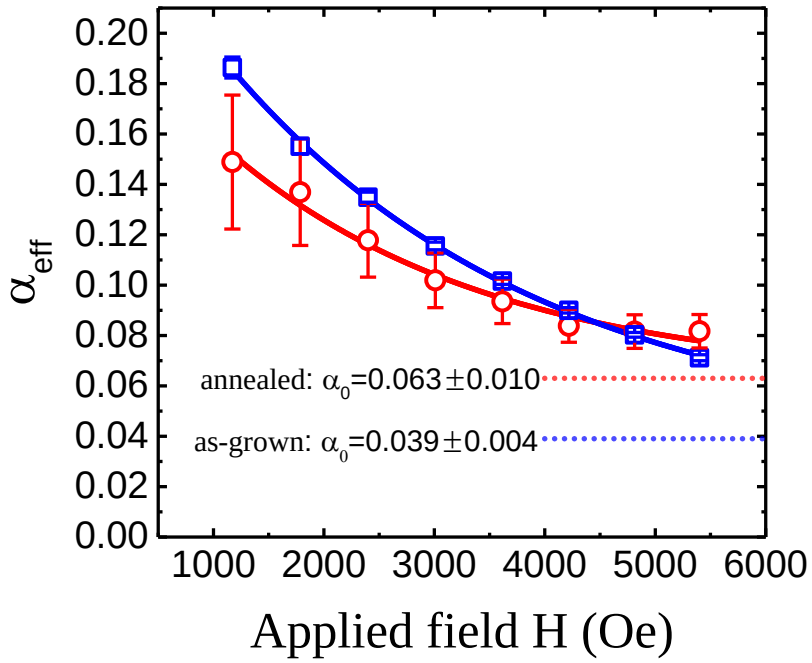

Figure 6.10: α_{eff} of as-grown (blue) and annealed (red) Fe_3O_4 films. From the single exponential decay fitting (solid lines), the intrinsic damping α_0 of both films are estimated.

The effective damping constant α_{eff} in both films decreases significantly with increasing applied field. This field dependence of the effective damping is commonly observed and explained. Normally, the effective damping constant consists of intrinsic and extrinsic components and the extrinsic damping mainly comes from magnetic inhomogeneity or two magnon scattering. In the low magnetic field region, the effective field is dominated by the spatially fluctuating anisotropy field which leads to increased damping, while in the high field region the effect of anisotropy field becomes weak since the external field dominates and hence the magnetic inhomogeneity reduces along with the damping constant [53, 58, 139]. In our measurement, the effective damping constant of annealed Fe_3O_4 film is smaller than that of the as-grown film under small applied field. This is consistent with the larger damping associated with lattice defects introduced by APBs or other defects present in the as-grown film. However, an intriguing finding is that when the applied field is strong enough, α_{eff} of as-grown film becomes smaller than α_{eff} of annealed film. Also, the difference of the field

dependence between both films is clear. Derived from the phenomenological fitting by a single exponential decay, the estimated high field limit of α_{eff} reaches the value $\alpha_0 = 0.039 \pm 0.004$ for the as-grown and $\alpha_0 = 0.063 \pm 0.010$ for the annealed film. The effective damping constant in the high field limit α_0 is increased by $\sim 62\%$ in the annealed Fe_3O_4 film compared to the as-grown film. The estimated damping value $\alpha_0 = 0.039 \pm 0.004$ for the as-grown is nearly same as the reported intrinsic value of a thin Fe_3O_4 film grown on MgO[246] and our measured damping values are consistent with the values measured in single-crystal Fe_3O_4/GaN thin films using a field pumped time-resolved MOKE[59]. To our best knowledge, the PSSW mode has not been observed in Fe_3O_4 films in other work, neither in the time-domain nor the frequency-domain measurements.

Now, the behaviour of the magnetic damping can be discussed in two respects. In the low field region, the effective damping in as-grown Fe_3O_4 film is larger than in the annealed film because of high density of defects. The structural defects contribute to magnetic inhomogeneities and two magnon scattering. This effect is consistent with the reported observations. On the other hand, in high field region, the contribution of magnetic inhomogeneities is reduced in high external field where the extrinsic term of magnetic damping is of less importance. Thus, the high field limit α_0 is always considered as, to some extent, the intrinsic damping constant. We now propose a phenomenological model, shown in Fig. 6.11, to explain the difference in magnetic damping of these two Fe_3O_4 films. In the as-grown film, only the uniform precession mode is observed in all the magnetic fields, so that the other spin wave effect can be ruled out. Thus, in the high field region, the extrinsic contribution to the effective damping becomes weak. In the annealed film, however, the observed PSSW mode may contributes to the magnetic damping making a larger effective damping. As a result, in the high field region the effective damping in annealed film is larger due to the existence of the additional perpendicular standing spin wave mode. A large enhancement of damping constant with less or no structural defects is demonstrated with a presence of an additional spin wave mode. Furthermore, this large α_0 in the annealed film may be associated with energy transfer from the Kittel mode to the PSSW mode because the

damping constant basically reflects the rate of energy dissipation. Intrinsic energy dissipation together with energy transfer to the PSSW mode leads to a larger magnetic damping in the annealed film even though it has less defects and two magnon scattering.

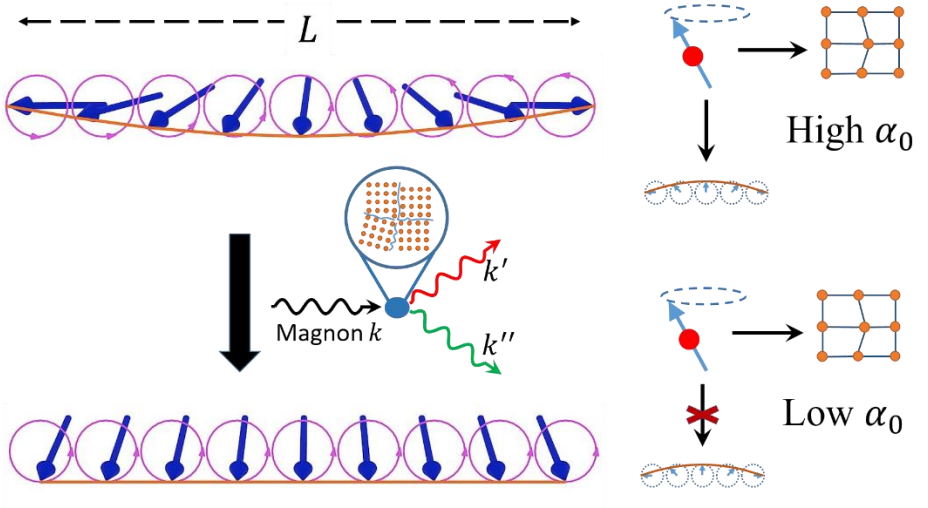

Figure 6.11: Without defect-induced magnon scattering, the PSSW is observed in annealed Fe_3O_4 film along with coherent Kittel magnetic precession. The intrinsic damping is increased in annealed Fe_3O_4 film compared to as-grown film due to the additional energy transfer channel from Kittel mode to PSSW mode.

6.7 Conclusion

In summary, the dynamic damping properties of the epitaxial grown Fe_3O_4 films with controlled atomic scale structures have been studied by all-optical TR-MOKE. The effect of the PSSW mode on the effective damping of the uniform process has been demonstrated. The intrinsic damping constant of the defect free film was found to be much larger than that of the film with defects. We propose that this enhancement may be attributed to the energy transfer from the Kittel mode to the PSSW mode in the defect free Fe_3O_4. This work shows clearly the effect of the defects on the magnetization precession and magnetic damping, which offers some insights into engineering the magnetic damping constant for spintronics applications including STT-MRAM and spin oscillators.

Chapter 7 Summary and outlook

7.1 Summary

This thesis presents a set of experimental studies on ultrafast laser-induced spin dynamics in multiple types of the magnetic materials, especially focused on the magnetic damping. Understanding and controlling magnetic damping is imperative as magnetic damping strongly affects operation energy and working frequency of a device. The all-optical pump-probe technique is a powerful tool to study the magnetisation precession and the magnetic damping, allowing direct observation of the magnetisation precession in time domain using femtosecond laser pulses. In order to further explore the physical nature of the magnetic damping, angular resolved photoemission spectroscopy (ARPES) and X-ray magnetic circular dichroism (XMCD) characterisation techniques have been applied in addition to time-resolved magneto-optic Kerr effect (TRMOKE).

The potential relation between the static uniaxial magnetic anisotropy (UMA) and the magnetic damping has been investigated in Fe/Cr/GaAs(100) heterostructures. The UMA of the 10 ML Fe layer decreases gradually as the thickness of the Cr interlayer increasing. On the other hand, the effective magnetic damping measured by TRMOKE shows a dramatic drop when a Cr interlayer is deposited, even with only 0.5 ML thickness. The reduced magnetic damping doesn't show an obvious dependence on the thickness of Cr interlayer. The orbit moments of Fe atoms obtained from XMCD measurements shows a similar dependence with respect to the thickness of Cr interlayer compared the UMA. Therefore, the UMA is attributed to the Fe-GaAs chemical bonding at the interface via increasing the orbit moments of Fe atoms and the Cr interlayer block this bonding gradually with increasing thickness. The magnetic damping is, however, not determined by the interface-induced orbit moments, although the Fe/GaAs interface unambiguously enhances the magnetic damping of Fe layer. It is suggested that the magnetic damping and the UMA does not share the same mechanism

in the Fe/GaAs(100) system.

The magnetic damping constant is theoretically predicted to be proportional to the density of state (DOS) at Fermi level $D(E_F)$. Here the correlation between the magnetic damping and $D(E_F)$ in a Heusler alloy Co_2FeAl is investigated using TRMOKE and ARPES, in the light of the fact that energy distribution curve (EDC) measured by ARPES can be treated to mimic the DOS. The high-quality Co_2FeAl samples are prepared at different temperatures using MBE. The smallest effective damping found in the sample grown at $300\ \mathrm{K}$ is attributed to the smallest value of $D(E_F)$. A "shoulder-like" peak is observed in the vicinity of Fermi level in the EDC of the samples grown at $500\ \mathrm{K}$ and $600\ \mathrm{K}$. With this peak, $D(E_F)$ would certainly be enhanced which attributes to the enhancement of magnetic damping in the samples grown at $500\ \mathrm{K}$ and $600\ \mathrm{K}$ compared to that grown at $300\ \mathrm{K}$. The difference of magnetic damping between the samples grown at $500\ \mathrm{K}$ and $600\ \mathrm{K}$ can be explained by the different peak intensity of the background-subtracted EDC of this "shoulder-like" peak, indicating a correlation between an extended flatband just above the Fermi level and an enhancement of both $D(E_F)$ and the magnetic damping. This work, for the first time, experimentally verified the proportional correlation between magnetic damping and $D(E_F)$ as theoretic studies predict and gives instructive indication on manipulation of magnetic damping.

In the last part of this thesis, effects of the structural defect in magnetite has been investigated. The magnetic damping has been investigated in defect-controlled epitaxial grown Fe_3O_4(111)/Yttria-stabilized Zirconia films by all-optical pump-probe measurements. A pair of defect-controlled epitaxial grown Fe_3O_4(111) is prepared by PLD; one is post-annealed at high temperature and the other is as-grown. TEM images show a single-crystalline structure in the post-annealed sample while defects are observed in the as-grown sample. In the TRMOKE measurements, the perpendicular standing spin wave (PSSW mode) is observed only in the annealed film without atomic defects. The numerical simulations confirm the presence of a standing wave in addition to the coherent magnetic precession (Kittel mode). The fact that only the uniform mode is observed in the as-grown film is attributed to magnon scattered by the structural

defects. The intrinsic damping constant $\alpha_0 = 0.063 \pm 0.010$ of the defect free Fe_3O_4 film was found to be strikingly larger than that of the as-grown film of $\alpha_0 = 0.039 \pm 0.004$. The results indicate that the PSSW mode leads to the enhancement of the magnetic damping associated with the emergence of an additional energy transfer channel from the uniform spin precession to the PSSW mode in the defect free Fe_3O_4.

7.2 Outlook

To gain more understanding of the origin of the magnetic damping, there are some further research works that could be implemented. Now that the magnetic damping of the 10 ML Fe is dramatically increased by the the Fe/GaAs interface demonstrated in chapter 4. To further investigate the effect of the interface, first principle calculation would be a useful method to simulate the electronic structure in the Fe/Cr/GaAs heterostructures. Moreover, high-resolution TEM images on the interfaces would be helpful to investigate the lattice structure and may offer better insight on the UMA and magnetic damping from an atomic perspective. Furthermore, as shown in chapter 5, the direct method to testify the correlation between the magnetic damping and the electronic structures is ARPES. Connecting the MBE growth chamber and the ARPES chamber, just as described in chapter 5, the set of Fe/Cr/GaAs samples can be *in-situ* characterised by the APRES. The anisotropic magnetic damping in ultrathin Fe/GaAs films can be investigated by measuring the EDC of the sample demagnetized along varying orientation. In fact, as it is demonstrated that the APRES is a powerful technique in studying the density of state at Fermi level, the underlying mechanisms of the magnetic damping in many materials can be studied using it. For example, the recent reported ultra-low magnetic damping observed in CoFe alloy, which is theoretically attributed to the low density of state at Fermi level, is an ideal object to study. Also, as a "should-like" peak in EDC in the vicinity of Fermi level observed in Co_2FeAl contributes to an enhancement of magnetic damping, an interesting question is brought out: is this effect exclusive in Co_2FeAl or extensively exists in many materials. To

answer this question, systematic studies in various materials are needed. For the magnetite, an interesting topic is to study the magnetic damping when the temperature crosses the Verwey transition. The Verwey transition is a low-temperature phase transition near 125 K: Fe_3O_4 is a metal when temperature is high than the Verwey temperature and become insulator when the temperature is below it. Across the Verwey temperature, the electronic properties of Fe_3O_4 changes because of structural changes. However, the behaviour of the magnetic damping with respect to the Verwey transition is unknown. It would be expected that the magnetic damping is higher in the low-temperature insulator phase than in the high-temperature metal phase because both electrical transport and magnetic damping is proportional to the density of state at Fermi level, in the case that other parameters are not changed. To verify this hypothesis, temperature-dependent measurements on the magnetic damping in Fe_3O_4 are required in the future work.

List of abbreviations

3TM	Three temperature
AD	Areal density
AGFM	Alternating gradient force magnetometer
AOS	All-optical switching
APB	Antiphase boundary
ARPES	Angle-resolved photoemission spectroscopy
BCC	Body-centered-cubic
BBO	Barium Borate
BEOL	Back-end of line
BLS	Brillouin light scattering
BS	Beam sampler
CAP	Coherent acoustic phonon
CCD	Charge-coupled device
CFA	Co_2FeAl
CMOS	Complementary metal-oxide-semiconductor
CW	Continuous wave
DE	Damon-Eschback
DOS	Density of state
EA	Easy axis
EDC	Energy distribution curve
FM	Ferromagnetic metal
FMR	Ferromagnetic resonance
FWHM	Full width at half maximum
GMR	Giant magnetoresistance
HA	Hard axis
HAADF	High angle annular dark field
HDD	Hard disk drive

HD-AOS	Helicity-dependent all-optical switching
HI-AOS	Helicity-independent all-optical switching
IPA	Iso-propyl alcohol
LA	Longitudinal accoustic
LCP	Left-handed circularly polarized
LL	Landau-Lifshitz
LLB	Landau-Lifshitz-Bloch
LLG	Landau-Lifshitz-Gilbert
MBE	Molecular beam expitaxy
MCD	Magnetic circular dichroism
MFM	Magnetic force microscopy
ML	Monolayer
MOKE	Magneto-optic Kerr effect
MR	Magnetoresistance
MRAM	Magnetoresistive random-access memory
MTJ	Magnetic tunnel junction
NM	Non-magnetic metal
PLD	Pulsed laser deposition
PM	Permanent magnet
PMR	Perpendicular magnetic recording
PSSW	Perpendicular standing spin wave
RCP	Right-handed circularly polarized
RHEED	Reflective high energy electron diffraction
RT	Room temperature
SAED	Selected area electron diffraction
SC	Semiconductor
SH	Sample holder
SOC	Spin-orbit coupling
SO-FMR	Spin-orbit ferromagnetic resonance
SQUID	Superconducting Quantum Interference Device

STEM	Scanning transmission electron microscope
STT	Spin transfer torque
TEM	Transmission electron microscopy
TEY	Total electron yield
TMR	Tunnelling magnetoresistance
TRMOKE	Time-resolved magneto-optic Kerr effect
UHV	Ultrahigh vacuum
UMA	Uniaxial magnetic anisotropy
VSM	Vibrating sample magnetometer
XAS	X-ray absorption spectra
XMCD	X-ray magnetic circular dichroism
YSZ	Yttria-stabilized Zirconia

List of symbols

α	magnetic damping constant
α_{eff}	effective magnetic damping constant
β	Faraday rotation
δ	skin depth
ε	permittivity tensor
h	Planck's constant
$\hbar$	reduced Planck's constant
ϕ	work function
θ_k	Kerr rotation
η_k	Kerr ellipticity
ν_{V}	Verdet constant
γ	gyromagnetic ratio
ρ	resistivity
μ_r	relative magnetic permeability
μ_0	permeability of free space
μ_B	Bohr magneton
ξ	spin-orbit interaction energy
λ	wavelength of light
ω	angular frequency of the magnetisation precession
τ	precession decay time
τ_E	electron scattering time
τ_M	ultrafast demagnetisation time
$\langle \boldsymbol{S} \rangle$	spin operator
$\mathcal{H}$	Hamiltonian
H_{Heis}	Heisenberg Hamiltonian
$\mathcal{J}_{ij}$	exchange integral
a_0	lattice constant

f	frequency of the magnetisation precession
g	Landé g factor
$\boldsymbol{k}$	wave vector
k_B	Boltzmann constant
m	magnetic moment
n	refractive index
s	total spin number
z	nearest-neighbour number
B	magnetic flux density
$D(E_F)$	density of states at Fermi level
F or G	free magnetic energy
G_{ij}	coupling constant between electrons, spins, and lattice
$\boldsymbol{H}$	magnetic field
$\boldsymbol{H}_{\mathbf{eff}}$	effective magnetic field
I	light intensity
J	exchange constant
J_c	threshold current density in MTJ
K_{u}	uniaxial anisotropy constant
K_1	first-order cubic anisotropy constant
M_s	saturation magnetisation
$\boldsymbol{M}$	magnetization
N	complex indices of refraction
N_{d}	demagnetisation factor
N_v	number of nearest-neighbour moments per unit volume
Q	complex magneto-optical constant
T_C	Curie temperature
T_{e}	electron temperature
T_{s}	spin temperature
T_{l}	lattice temperature
V_s	speed of longitudinal acoustic phonon

W	d-band width

References

[1] L. William, "Fundamentals of geophysics," *Cambridge,* 1997.

[2] B. D. Cullity and C. D. Graham, *Introduction to magnetic materials*. John Wiley & Sons, 2011.

[3] S. G. Brush, "History of the Lenz-Ising model," *Rev. Mod. Phys.,* vol. 39, no. 4, p. 883, 1967.

[4] P. A. Grünberg, "Nobel Lecture: From spin waves to giant magnetoresistance and beyond," *Rev. Mod. Phys.,* vol. 80, no. 4, p. 1531, 2008.

[5] M. N. Baibich, J. M. Broto, A. Fert, F. N. Van Dau, F. Petroff, P. Etienne, G. Creuzet, A. Friederich, and J. Chazelas, "Giant Magnetoresistance of (001)Fe/(001)Cr Magnetic Superlattices," *Phys. Rev. Lett.,* vol. 61, no. 21, pp. 2472-2475, 1988.

[6] G. Binasch, P. Grünberg, F. Saurenbach, and W. Zinn, "Enhanced magnetoresistance in layered magnetic structures with antiferromagnetic interlayer exchange," *Phys. Rev. B,* vol. 39, no. 7, pp. 4828-4830, 1989.

[7] E. Grochowski and R. D. Halem, "Technological impact of magnetic hard disk drives on storage systems," *IBM SYST J.,* vol. 42, no. 2, pp. 338-346, 2003.

[8] E. Chen, D. Apalkov, Z. Diao, A. Driskill-Smith, D. Druist, D. Lottis, V. Nikitin, X. Tang, S. Watts, S. Wang, S. A. Wolf, A. W. Ghosh, J. W. Lu, S. J. Poon, M. Stan, W. H. Butler, S. Gupta, C. K. A. Mewes, T. Mewes, and P. B. Visscher, "Advances and Future Prospects of Spin-Transfer Torque Random Access Memory," *IEEE Trans. Magn.,* vol. 46, no. 6, pp. 1873-1878, 2010.

[9] J. A. Katine, F. J. Albert, R. A. Buhrman, E. B. Myers, and D. C. Ralph, "Current-driven magnetization reversal and spin-wave excitations in Co/Cu/Co pillars," *Phys. Rev. Lett.,* vol. 84, no. 14, pp. 3149-3152, 2000.

[10] S. S. Parkin, C. Kaiser, A. Panchula, P. M. Rice, B. Hughes, M. Samant, and S. H. Yang, "Giant tunnelling magnetoresistance at room temperature with MgO (100) tunnel barriers," *Nat. Mater.,* vol. 3, no. 12, pp. 862-7, 2004.

[11] S. Ikeda, J. Hayakawa, Y. Ashizawa, Y. M. Lee, K. Miura, H. Hasegawa, M. Tsunoda, F. Matsukura, and H. Ohno, "Tunnel magnetoresistance of 604% at 300K by suppression of Ta diffusion in CoFeB/MgO/CoFeB pseudo-spin-valves annealed at high temperature," *Appl. Phys. Lett.,* vol. 93, no. 8, p. 082508, 2008.

[12] D. D. Djayaprawira, K. Tsunekawa, M. Nagai, H. Maehara, S. Yamagata, N. Watanabe, S. Yuasa, Y. Suzuki, and K. Ando, "230% room-temperature magnetoresistance in CoFeB/MgO/CoFeB magnetic tunnel junctions," *Appl. Phys. Lett.,* vol. 86, no. 9, p. 092502, 2005.

[13] J. J. Cha, J. C. Read, W. F. Egelhoff, P. Y. Huang, H. W. Tseng, Y. Li, R. A. Buhrman, and D. A. Muller, "Atomic-scale spectroscopic imaging of CoFeB/Mg–B–O/CoFeB magnetic tunnel junctions," *Appl. Phys. Lett.,* vol. 95, no. 3, p. 032506, 2009.

[14] K. Tsunekawa, D. D. Djayaprawira, M. Nagai, H. Maehara, S. Yamagata, N. Watanabe, S. Yuasa, Y. Suzuki, and K. Ando, "Giant tunneling magnetoresistance effect in low-resistance CoFeB/MgO(001)/CoFeB magnetic tunnel junctions for read-head applications," *Appl. Phys. Lett.,* vol. 87, no. 7, p. 072503, 2005.

[15] K. L. Wang, J. G. Alzate, and P. Khalili Amiri, "Low-power non-volatile spintronic memory: STT-RAM and beyond," *J. Phys. D: Appl. Phys.,* vol. 46, no. 7, p. 074003, 2013.

[16] K. Lee and S. H. Kang, "Development of embedded STT-MRAM for mobile system-on-chips," *IEEE Trans. Magn.,* vol. 47, no. 1, pp. 131-136, 2011.

[17] J. Z. Sun, "Spin-current interaction with a monodomain magnetic body: A model study," *Phys. Rev. B,* vol. 62, no. 1, pp. 570-578, 2000.

[18] M. Julliere, "Tunneling between ferromagnetic films," *Phys. Lett. A,* vol. 54, no. 3, pp. 225-226, 1975.

[19] M. Bowen, M. Bibes, A. Barthélémy, J. P. Contour, A. Anane, Y. Lemaître, and A. Fert, "Nearly total spin polarization in La2/3Sr1/3MnO3 from tunneling experiments," *Appl. Phys. Lett.,* vol. 82, no. 2, pp. 233-235, 2003.

[20] E. Beaurepaire, J. Merle, A. Daunois, and J. Bigot, "Ultrafast spin dynamics in

ferromagnetic nickel," *Phys. Rev. Lett.,* vol. 76, no. 22, pp. 4250-4253, 1996.

[21] M. Agranat, S. Ashitkov, A. Granovskii, and G. Rukman, "Interaction of picosecond laser pulses with the electron, spin, and phonon subsystems of nickel," *Zh. Eksp. Teor. Fiz,* vol. 86, no. 1376, p. 10, 1984.

[22] A. Vaterlaus, D. Guarisco, M. Lutz, M. Aeschlimann, M. Stampanoni, and F. Meier, "Different spin and lattice temperatures observed by spin-polarized photoemission with picosecond laser pulses," *J. Appl. Phys.,* vol. 67, no. 9, pp. 5661-5663, 1990.

[23] E. Carpene, E. Mancini, C. Dallera, M. Brenna, E. Puppin, and S. De Silvestri, "Dynamics of electron-magnon interaction and ultrafast demagnetization in thin iron films," *Phys. Rev. B,* vol. 78, no. 17, p. 174422, 2008.

[24] A. Vaterlaus, T. Beutler, and F. Meier, "Spin-lattice relaxation time of ferromagnetic gadolinium determined with time-resolved spin-polarized photoemission," *Phys. Rev. Lett.,* vol. 67, no. 23, pp. 3314-3317, 1991.

[25] A. Scholl, L. Baumgarten, R. Jacquemin, and W. Eberhardt, "Ultrafast spin dynamics of ferromagnetic thin films observed by fs spin-resolved two-photon photoemission," *Phys. Rev. Lett.,* vol. 79, no. 25, pp. 5146-5149, 1997.

[26] C. Stamm, T. Kachel, N. Pontius, R. Mitzner, T. Quast, K. Holldack, S. Khan, C. Lupulescu, E. F. Aziz, M. Wietstruk, H. A. Durr, and W. Eberhardt, "Femtosecond modification of electron localization and transfer of angular momentum in nickel," *Nat. Mater.,* vol. 6, no. 10, pp. 740-3, 2007.

[27] B. Koopmans, M. van Kampen, J. T. Kohlhepp, and W. J. de Jonge, "Ultrafast magneto-optics in nickel: magnetism or optics?," *Phys. Rev. Lett.,* vol. 85, no. 4, pp. 844-7, 2000.

[28] L. Guidoni, E. Beaurepaire, and J. Y. Bigot, "Magneto-optics in the ultrafast regime: thermalization of spin populations in ferromagnetic films," *Phys. Rev. Lett.,* vol. 89, no. 1, p. 017401, 2002.

[29] J. Y. Bigot, L. Guidoni, E. Beaurepaire, and P. N. Saeta, "Femtosecond Spectrotemporal Magneto-optics," *Phys. Rev. Lett.,* vol. 93, no. 7, p. 077401, 2004.

[30] R. Wilks, R. J. Hicken, M. Ali, B. J. Hickey, J. D. R. Buchanan, A. T. G. Pym, and B. K. Tanner, "Investigation of ultrafast demagnetization and cubic optical nonlinearity of Ni in the polar geometry," *J. Appl. Phys.,* vol. 95, no. 11, pp. 7441-7443, 2004.

[31] P. M. Oppeneer and A. Liebsch, "Ultrafast demagnetization in Ni: theory of magneto-optics for non-equilibrium electron distributions," *J. Phys.: Condens. Matter,* vol. 16, no. 30, pp. 5519-5530, 2004.

[32] G. P. Zhang, W. Hübner, G. Lefkidis, Y. Bai, and T. F. George, "Paradigm of the time-resolved magneto-optical Kerr effect for femtosecond magnetism," *Nat. Phys.,* vol. 5, no. 7, pp. 499-502, 2009.

[33] W. Hubner and G. P. Zhang, "Ultrafast spin dynamics in nickel," *Phys. Rev. B,* vol. 58, p. R5920, 1998.

[34] N. Del Fatti, C. Voisin, M. Achermann, S. Tzortzakis, D. Christofilos, and F. Vallee, "Nonequilibrium electron dynamics in noble metals," *Phys. Rev. B,* vol. 61, no. 24, pp. 16956-16966, 2000.

[35] J. Wang, Ł. Cywiński, C. Sun, J. Kono, H. Munekata, and L. J. Sham, "Femtosecond demagnetization and hot-hole relaxation in ferromagnetic Ga1−xMnxAs," *Phys. Rev. B,* vol. 77, no. 23, p. 235308, 2008.

[36] A. V. Kimel, R. V. Pisarev, J. Hohlfeld, and T. Rasing, "Ultrafast quenching of the antiferromagnetic order in FeBO3: direct optical probing of the phonon-magnon coupling," *Phys. Rev. Lett.,* vol. 89, no. 28 Pt 1, p. 287401, 2002.

[37] G. M. Muller, J. Walowski, M. Djordjevic, G. X. Miao, A. Gupta, A. V. Ramos, K. Gehrke, V. Moshnyaga, K. Samwer, J. Schmalhorst, A. Thomas, A. Hutten, G. Reiss, J. S. Moodera, and M. Munzenberg, "Spin polarization in half-metals probed by femtosecond spin excitation," *Nat. Mater.,* vol. 8, no. 1, pp. 56-61, 2009.

[38] A. Kirilyuk, A. V. Kimel, and T. Rasing, "Ultrafast optical manipulation of magnetic order," *Rev. Mod. Phys.,* vol. 82, no. 3, pp. 2731-2784, 2010.

[39] P. Wolf, "Free Oscillations of the Magnetization in Permalloy Films," *J. Appl. Phys.,* vol. 32, no. 3, pp. S95-S96, 1961.

[40] T. J. Silva, C. S. Lee, T. M. Crawford, and C. T. Rogers, "Inductive measurement of ultrafast magnetization dynamics in thin-film Permalloy," *J. Appl. Phys.,* vol. 85, no. 11, p. 7849, 1999.

[41] S. S. Kalarickal, P. Krivosik, M. Wu, C. E. Patton, M. L. Schneider, P. Kabos, T. J. Silva, and J. P. Nibarger, "Ferromagnetic resonance linewidth in metallic thin films: Comparison of measurement methods," *J. Appl. Phys.,* vol. 99, no. 9, p. 093909, 2006.

[42] G. Boero, S. Rusponi, P. Bencok, R. S. Popovic, H. Brune, and P. Gambardella, "X-ray ferromagnetic resonance spectroscopy," *Appl. Phys. Lett.,* vol. 87, no. 15, p. 152503, 2005.

[43] B. Van Waeyenberge, A. Puzic, H. Stoll, K. W. Chou, T. Tyliszczak, R. Hertel, M. Fahnle, H. Bruckl, K. Rott, G. Reiss, I. Neudecker, D. Weiss, C. H. Back, and G. Schutz, "Magnetic vortex core reversal by excitation with short bursts of an alternating field," *Nature,* vol. 444, no. 7118, pp. 461-4, 2006.

[44] A. B. Kos, T. J. Silva, and P. Kabos, "Pulsed inductive microwave magnetometer," *Rev. Sci. Instrum.,* vol. 73, no. 10, pp. 3563-3569, 2002.

[45] S. Azzawi, A. T. Hindmarch, and D. Atkinson, "Magnetic damping phenomena in ferromagnetic thin-films and multilayers," *J. Phys. D: Appl. Phys.,* vol. 50, no. 47, p. 473001, 2017.

[46] M. R. Freeman, R. R. Ruf, and R. J. Gambino, "Picosecond Pulsed Magnetic-Fields for Studies of Ultrafast Magnetic Phenomena," *IEEE Trans. Magn.,* vol. 27, no. 6, pp. 4840-4842, 1991.

[47] M. R. Freeman, M. J. Brady, and J. Smyth, "Extremely high frequency pulse magnetic resonance by picosecond magneto-optic sampling," *Appl. Phys. Lett.,* vol. 60, no. 20, pp. 2555-2557, 1992.

[48] W. K. Hiebert, A. Stankiewicz, and M. R. Freeman, "Direct observation of magnetic relaxation in a small permalloy disk by time-resolved scanning Kerr microscopy," *Phys. Rev. Lett.,* vol. 79, no. 6, pp. 1134-1137, 1997.

[49] R. J. Hicken and J. Wu, "Observation of ferromagnetic resonance in the time domain," *J. Appl. Phys.,* vol. 85, no. 8, pp. 4580-4582, 1999.

[50] D. Guarisco, R. Burgermeister, C. Stamm, and F. Meier, "Magnetization reversal in the picosecond range measured with time-resolved magneto-optical Kerr effect," *Appl. Phys. Lett.,* vol. 68, no. 12, pp. 1729-1731, 1996.

[51] G. P. Ju, A. V. Nurmikko, R. F. C. Farrow, R. F. Marks, M. J. Carey, and B. A. Gurney, "Ultrafast time resolved photoinduced magnetization rotation in a ferromagnetic/antiferromagnetic exchange coupled system," *Phys. Rev. Lett.,* vol. 82, no. 18, pp. 3705-3708, 1999.

[52] M. van Kampen, C. Jozsa, J. T. Kohlhepp, P. LeClair, L. Lagae, W. J. De Jonge, and B. Koopmans, "All-optical probe of coherent spin waves," *Phys. Rev. Lett.,* vol. 88, no. 22, p. 227201, 2002.

[53] B. Liu, X. Ruan, Z. Wu, H. Tu, J. Du, J. Wu, X. Lu, L. He, R. Zhang, and Y. Xu, "Transient enhancement of magnetization damping in CoFeB film via pulsed laser excitation," *Appl. Phys. Lett.,* vol. 109, no. 4, p. 042401, 2016.

[54] S. Mizukami, F. Wu, A. Sakuma, J. Walowski, D. Watanabe, T. Kubota, X. Zhang, H. Naganuma, M. Oogane, Y. Ando, and T. Miyazaki, "Long-lived ultrafast spin precession in manganese alloys films with a large perpendicular magnetic anisotropy," *Phys. Rev. Lett.,* vol. 106, no. 11, p. 117201, 2011.

[55] P. He, X. Ma, J. W. Zhang, H. B. Zhao, G. Lupke, Z. Shi, and S. M. Zhou, "Quadratic scaling of intrinsic Gilbert damping with spin-orbital coupling in L10 FePdPt films: experiments and Ab initio calculations," *Phys. Rev. Lett.,* vol. 110, no. 7, p. 077203, 2013.

[56] A. Barman, S. Wang, O. Hellwig, A. Berger, E. E. Fullerton, and H. Schmidt, "Ultrafast magnetization dynamics in high perpendicular anisotropy [Co/Pt]n multilayers," *J. Appl. Phys.,* vol. 101, no. 9, p. 09D102, 2007.

[57] S. Qiao, S. Nie, J. Zhao, Y. Huo, Y. Wu, and X. Zhang, "Magnetic and Gilbert damping properties of L21-Co2FeAl film grown by molecular beam epitaxy," *Appl. Phys. Lett.,* vol. 103, no. 15, p. 152402, 2013.

[58] Z. F. Chen, M. Yi, M. Chen, S. F. Li, S. M. Zhou, and T. S. Lai, "Spin waves and small intrinsic damping in an in-plane magnetized FePt film," *Appl. Phys. Lett.,* vol. 101, no. 22, p. 222402, 2012.

[59] X. Zou, J. Wu, P. K. J. Wong, Y. B. Xu, R. Zhang, Y. Zhai, C. Bunce, and R. W. Chantrell, "Damping in magnetization dynamics of single-crystal Fe3O4/GaN thin films," *J. Appl. Phys.,* vol. 109, no. 7, p. 07D341, Apr 1 2011.

[60] J. Walowski, M. D. Kaufmann, B. Lenk, C. Hamann, J. McCord, and M. Münzenberg, "Intrinsic and non-local Gilbert damping in polycrystalline nickel studied by Ti : sapphire laser fs spectroscopy," *J. Phys. D: Appl. Phys.,* vol. 41, no. 16, p. 164016, 2008.

[61] B. Koopmans, J. J. Ruigrok, F. D. Longa, and W. J. M. de Jonge, "Unifying ultrafast magnetization dynamics," *Phys. Rev. Lett.,* vol. 95, no. 26, p. 267207, 2005.

[62] T. L. Gilbert, "A phenomenological theory of damping in ferromagnetic materials," *IEEE Trans. Magn.,* vol. 40, no. 6, pp. 3443-3449, Nov 2004.

[63] S. V. e. Von Sovskii, *Ferromagnetic resonance: the phenomenon of resonant absorption of a high-frequency magnetic field in ferromagnetic substances*. Elsevier, 2016.

[64] V. Korenman and R. E. Prange, "Anomalous Damping of Spin Waves in Magnetic Metals," *Phys. Rev. B,* vol. 6, no. 7, pp. 2769-2777, 1972.

[65] V. Kamberský, "On ferromagnetic resonance damping in metals," *Czechoslov. J. Phys. B,* vol. 26, no. 12, pp. 1366-1383, 1976.

[66] K. Zakeri, J. Lindner, I. Barsukov, R. Meckenstock, M. Farle, U. von Hörsten, H. Wende, W. Keune, J. Rocker, S. S. Kalarickal, K. Lenz, W. Kuch, K. Baberschke, and Z. Frait, "Spin dynamics in ferromagnets: Gilbert damping and two-magnon scattering," *Phys. Rev. B,* vol. 76, no. 10, p. 104416, 2007.

[67] L. Berger, "Effect of interfaces on Gilbert damping and ferromagnetic resonance linewidth in magnetic multilayers," *J. Appl. Phys.,* vol. 90, no. 9, pp. 4632-4638, 2001.

[68] K. Lenz, H. Wende, W. Kuch, K. Baberschke, K. Nagy, and A. Jánossy, "Two-magnon scattering and viscous Gilbert damping in ultrathin ferromagnets," *Phys. Rev. B,* vol. 73, no. 14, p. 144424, 2006.

[69] J. Ho, F. Khanna, and B. Choi, "Radiation-spin interaction, Gilbert damping,

and spin torque," *Phys. Rev. Lett.,* vol. 92, no. 9, p. 097601, 2004.

[70] R. Urban, G. Woltersdorf, and B. Heinrich, "Gilbert damping in single and multilayer ultrathin films: role of interfaces in nonlocal spin dynamics," *Phys. Rev. Lett.,* vol. 87, no. 21, p. 217204, 2001.

[71] R. E. Prange and V. Korenman, "Line width of ferromagnetic resonance in metals," *J. Magn. Reson.,* vol. 6, no. 3, pp. 274-280, 1972.

[72] L. Berger, "Emission of spin waves by a magnetic multilayer traversed by a current," *Phys. Rev. B,* vol. 54, no. 13, pp. 9353-9358, 1996.

[73] E. Barati, M. Cinal, D. M. Edwards, and A. Umerski, "Gilbert damping in magnetic layered systems," *Phys. Rev. B,* vol. 90, no. 1, p. 014420, 2014.

[74] V. L. Safonov and H. N. Bertram, "Impurity relaxation mechanism for dynamic magnetization reversal in a single domain grain," *Phys. Rev. B,* vol. 61, no. 22, p. R14893, 2000.

[75] F. Hartmann-Boutron, "Effect of Rare-Earth Impurities on the Ferrimagnetic Resonance and Nuclear Relaxation in Yttrium Iron Garnet," *J. Appl. Phys.,* vol. 35, no. 3, pp. 889-891, 1964.

[76] H. Suhl, "Theory of the magnetic damping constant," *IEEE Trans. Magn.,* vol. 34, no. 4, pp. 1834-1838, Jul 1998.

[77] J. Van Vleck, "Ferrimagnetic Resonance of Rare-Earth-Doped Iron Garnets," *J. Appl. Phys.,* vol. 35, no. 3, pp. 882-888, 1964.

[78] M. Sparks, *Ferromagnetic-relaxation theory*. McGraw-Hill, 1964.

[79] R. D. McMichael and A. Kunz, "Calculation of damping rates in thin inhomogeneous ferromagnetic films due to coupling to lattice vibrations," *J. Appl. Phys.,* vol. 91, no. 10, pp. 8650-8652, 2002.

[80] R. D. McMichael and P. Krivosik, "Classical model of extrinsic ferromagnetic resonance linewidth in ultrathin films," *IEEE Trans. Magn.,* vol. 40, no. 1, pp. 2-11, 2004.

[81] R. Silberglitt, "Effect of spin waves on the phonon energy spectrum of a heisenberg ferromagnet," *Phys. Rev.,* vol. 188, no. 2, p. 786, 1969.

[82] M. A. W. Schoen, D. Thonig, M. L. Schneider, T. J. Silva, H. T. Nembach, O.

Eriksson, O. Karis, and J. M. Shaw, "Ultra-low magnetic damping of a metallic ferromagnet," *Nat. Phys.,* vol. 12, no. 9, pp. 839-842, Sep 2016.

[83] A. Barman and J. Sinha, "Magnetic Damping," in *Spin Dynamics and Damping in Ferromagnetic Thin Films and Nanostructures*: Springer, 2018, pp. 27-46.

[84] J. F. Cochran, B. Heinrich, and A. S. Arrott, "Ferromagnetic resonance in a system composed of a ferromagnetic substrate and an exchange-coupled thin ferromagnetic overlayer," *Phys. Rev. B,* vol. 34, no. 11, pp. 7788-7801, 1986.

[85] V. Kamberský, "On the Landau–Lifshitz relaxation in ferromagnetic metals," *Can. J. Phys.,* vol. 48, no. 24, pp. 2906-2911, 1970.

[86] J. Kuneš and V. Kamberský, "First-principles investigation of the damping of fast magnetization precession in ferromagnetic 3d metals," *Phys. Rev. B,* vol. 65, no. 21, p. 212411, 2002.

[87] H. Ebert, S. Mankovsky, D. Kodderitzsch, and P. J. Kelly, "Ab initio calculation of the Gilbert damping parameter via the linear response formalism," *Phys. Rev. Lett.,* vol. 107, no. 6, p. 066603, 2011.

[88] S. Lounis, M. dos Santos Dias, and B. Schweflinghaus, "Transverse dynamical magnetic susceptibilities from regular static density functional theory: Evaluation of damping andgshifts of spin excitations," *Phys. Rev. B,* vol. 91, no. 10, p. 104420, 2015.

[89] S. Mizukami, D. Watanabe, M. Oogane, Y. Ando, Y. Miura, M. Shirai, and T. Miyazaki, "Low damping constant for Co2FeAl Heusler alloy films and its correlation with density of states," *J. Appl. Phys.,* vol. 105, no. 7, p. 07D306, 2009.

[90] R. Arias and D. L. Mills, "Extrinsic contributions to the ferromagnetic resonance response of ultrathin films," *Phys. Rev. B,* vol. 60, no. 10, pp. 7395-7409, 1999.

[91] G. Woltersdorf, M. Buess, B. Heinrich, and C. H. Back, "Time resolved magnetization dynamics of ultrathin Fe(001) films: spin-pumping and two-magnon scattering," *Phys. Rev. Lett.,* vol. 95, no. 3, p. 037401, 2005.

[92] A. K. Zvezdin and V. A. Kotov, *Modern magnetooptics and magnetooptical*

materials. CRC Press, 1997.

[93] J. A. C. Bland, M. J. Padgett, R. J. Butcher, and N. Bett, "An Intensity-Stabilized He-Ne-Laser for Measuring Small Magneto-Optic Kerr Rotations From Thin Ferromagnetic-Films," *J. Phys. E: Sci. Instrum.,* vol. 22, no. 5, pp. 308-312, May 1989.

[94] Z. J. Yang and M. R. Scheinfein, "Combined three-axis surface magneto-optical Kerr effects in the study of surface and ultrathin-film magnetism," *J. Appl. Phys.,* vol. 74, no. 11, p. 6810, 1993.

[95] J. Hamrle, S. Blomeier, O. Gaier, B. Hillebrands, H. Schneider, G. Jakob, K. Postava, and C. Felser, "Huge quadratic magneto-optical Kerr effect and magnetization reversal in the Co2FeSi Heusler compound," *J. Phys. D: Appl. Phys.,* vol. 40, no. 6, pp. 1563-1569, 2007.

[96] P. Yeh and C. Gu, *Optics of liquid crystal displays*. John Wiley & Sons, 2010.

[97] B. Hillebrands and K. Ounadjela, *Spin dynamics in confined magnetic structures I*. Springer Science & Business Media, 2003.

[98] L. D. Landau and E. M. Lifshitz, "On the theory of the dispersion of magnetic permeability in ferromagnetic bodies," *Phys. Z. Sowjet.,* vol. 8, pp. 153-169, 1935.

[99] T. Gilbert, "A Lagrangian formulation of the gyromagnetic equation of the magnetization field," *Phys. Rev.,* vol. 100, p. 1243, 1955.

[100] M. D. Kaufmann, "Magnetization dynamics in all-optical pump-probe experiments: spin-wave modes and spin-current damping," University of Goettingen, 2006.

[101] A. Hubert and R. Schäfer, *Magnetic domains: the analysis of magnetic microstructures*. Springer Science & Business Media, 2008.

[102] R. C. O'handley, *Modern magnetic materials: principles and applications*. Wiley, 2000.

[103] S. Mizukami, Y. Ando, and T. Miyazaki, "The Study on Ferromagnetic Resonance Linewidth for NM/80NiFe/NM (NM=Cu, Ta, Pd and Pt) Films," *Jpn. J. Appl. Phys.,* vol. 40, no. Part 1, No. 2A, pp. 580-585, 2001.

[104] S. Mizukami, H. Abe, D. Watanabe, M. Oogane, Y. Ando, and T. Miyazaki, "Gilbert Damping for Various Ni80Fe20Thin Films Investigated Using All-Optical Pump–Probe Detection and Ferromagnetic Resonance," *Appl. Phys. Express,* vol. 1, p. 121301, 2008.

[105] M. Oogane, T. Wakitani, S. Yakata, R. Yilgin, Y. Ando, A. Sakuma, and T. Miyazaki, "Magnetic Damping in Ferromagnetic Thin Films," *Jpn. J. Appl. Phys.,* vol. 45, no. 5A, pp. 3889-3891, 2006.

[106] V. Kamberský, "Spin-orbital Gilbert damping in common magnetic metals," *Phys. Rev. B,* vol. 76, no. 13, p. 134416, 2007.

[107] S. Mankovsky, D. Ködderitzsch, G. Woltersdorf, and H. Ebert, "First-principles calculation of the Gilbert damping parameter via the linear response formalism with application to magnetic transition metals and alloys," *Phys. Rev. B,* vol. 87, no. 1, p. 014430, 2013.

[108] B. Heinrich, D. Meredith, and J. Cochran, "Wave number and temperature dependent Landau-Lifshitz damping in nickel," *J. Appl. Phys.,* vol. 50, no. B11, pp. 7726-7728, 1979.

[109] J. Cochran and B. Heinrich, "Microwave transmission through ferromagnetic metals," *IEEE Trans. Magn.,* vol. 16, no. 5, pp. 660-665, 1980.

[110] K. Gilmore, Y. Idzerda, and M. D. Stiles, "Identification of the dominant precession-damping mechanism in Fe, Co, and Ni by first-principles calculations," *Phys. Rev. Lett.,* vol. 99, no. 2, p. 027204, 2007.

[111] K. Gilmore, Y. U. Idzerda, and M. D. Stiles, "Spin-orbit precession damping in transition metal ferromagnets," *J. Appl. Phys.,* vol. 103, no. 7, p. 07D303, 2008.

[112] Y. Tserkovnyak, A. Brataas, and G. E. Bauer, "Enhanced gilbert damping in thin ferromagnetic films," *Phys. Rev. Lett.,* vol. 88, no. 11, p. 117601, 2002.

[113] S. Azzawi, A. Ganguly, M. Tokaç, R. M. Rowan-Robinson, J. Sinha, A. T. Hindmarch, A. Barman, and D. Atkinson, "Evolution of damping in ferromagnetic/nonmagnetic thin film bilayers as a function of nonmagnetic layer thickness," *Phys. Rev. B,* vol. 93, no. 5, p. 054402, 2016.

[114] R. D. McMichael, D. Twisselmann, and A. Kunz, "Localized ferromagnetic

resonance in inhomogeneous thin films," *Phys. Rev. Lett.,* vol. 90, no. 22, p. 227601, 2003.

[115] F. Bloch, "Nuclear induction," *Phys. Rev.,* vol. 70, no. 7-8, p. 460, 1946.

[116] N. Bloembergen, "On the ferromagnetic resonance in nickel and supermalloy," *Phys. Rev.,* vol. 78, no. 5, p. 572, 1950.

[117] H. Suhl, "Ferromagnetic resonance in nickel ferrite between one and two kilomegacycles," *Phys. Rev.,* vol. 97, no. 2, p. 555, 1955.

[118] Y. V. Goryunov, N. Garif'yanov, G. Khaliullin, I. Garifullin, L. Tagirov, F. Schreiber, T. Mühge, and H. Zabel, "Magnetic anisotropies of sputtered Fe films on MgO substrates," *Phys. Rev. B,* vol. 52, no. 18, p. 13450, 1995.

[119] M. Hurben, D. Franklin, and C. Patton, "Angle dependence of the ferromagnetic resonance linewidth in easy-axis and easy-plane single crystal hexagonal ferrite disks," *J. Appl. Phys.,* vol. 81, no. 11, pp. 7458-7467, 1997.

[120] C. Józsa, "Optical detection of the magnetization precession," Eindhoven University of Technology, 2006.

[121] R. Damon and J. Eshbach, "Magnetostatic modes of a ferromagnetic slab," *J. Appl. Phys.,* vol. 31, no. 5, pp. S104-S105, 1960.

[122] Y. B. Xu, D. J. Freeland, M. Tselepi, and J. A. C. Bland, "Uniaxial magnetic anisotropy of epitaxial Fe films on InAs(100)-4×2 and GaAs(100)-4×2," *J. Appl. Phys.,* vol. 87, no. 9, pp. 6110-6112, 2000.

[123] Y. B. Xu, E. T. M. Kernohan, D. J. Freeland, A. Ercole, M. Tselepi, and J. A. C. Bland, "Evolution of the ferromagnetic phase of ultrathin Fe films grown on GaAs(100)-4x6," *Phys. Rev. B,* vol. 58, no. 2, pp. 890-896, 1998.

[124] S. Foner, "Vibrating Sample Magnetometer," *Rev. Sci. Instrum.,* vol. 27, no. 7, pp. 548-548, 1956.

[125] S. Foner, "The vibrating sample magnetometer: Experiences of a volunteer (invited)," *J. Appl. Phys.,* vol. 79, no. 8, p. 4740, 1996.

[126] M. S. Lubell and A. S. Venturino, "Vibrating Sample Magnetometer," *Rev. Sci. Instrum.,* vol. 31, no. 2, pp. 207-208, 1960.

[127] C. Graham, "High-sensitivity magnetization measurements," *J. Mater. Sci.*

Technol., vol. 16, no. 2, pp. 97-101, 2000.

[128] J. Griffiths, "Anomalous high-frequency resistance of ferromagnetic metals," *Nature,* vol. 158, no. 4019, p. 670, 1946.

[129] C. E. Patton, "Linewidth and Relaxation Processes for the Main Resonance in the Spin-Wave Spectra of Ni–Fe Alloy Films," *J. Appl. Phys.,* vol. 39, no. 7, pp. 3060-3068, 1968.

[130] I. Neudecker, G. Woltersdorf, B. Heinrich, T. Okuno, G. Gubbiotti, and C. Back, "Comparison of frequency, field, and time domain ferromagnetic resonance methods," *J. Magn. Magn. Mater.,* vol. 307, no. 1, pp. 148-156, 2006.

[131] J. Moreland, M. Löhndorf, P. Kabos, and R. D. McMichael, "Ferromagnetic resonance spectroscopy with a micromechanical calorimeter sensor," *Rev. Sci. Instrum.,* vol. 71, no. 8, pp. 3099-3103, 2000.

[132] W. Barry, "A broad-band, automated, stripline technique for the simultaneous measurement of complex permittivity and permeability," *IEEE Trans. Microw. Theory Tech.,* vol. 34, no. 1, pp. 80-84, 1986.

[133] J. Kieffer, *Brillouin Light Scattering* (Modern Glass Characterization). 2015.

[134] T. Kampfrath, R. G. Ulbrich, F. Leuenberger, M. Münzenberg, B. Sass, and W. Felsch, "Ultrafast magneto-optical response of iron thin films," *Phys. Rev. B,* vol. 65, no. 10, p. 104429, 2002.

[135] D. Strickland and G. Mourou, "Compression of amplified chirped optical pulses," *Opt. Commun.,* vol. 55, no. 6, pp. 447-449, 1985.

[136] G. Li, "Ultrafast laser-induced spin/electron dynamic in advanced material," MSc by research thesis, University of York, 2017.

[137] S. Mizukami, E. P. Sajitha, D. Watanabe, F. Wu, T. Miyazaki, H. Naganuma, M. Oogane, and Y. Ando, "Gilbert damping in perpendicularly magnetized Pt/Co/Pt films investigated by all-optical pump-probe technique," *Appl. Phys. Lett.,* vol. 96, no. 15, p. 152502, 2010.

[138] M. A. Schoen, J. M. Shaw, H. T. Nembach, M. Weiler, and T. J. Silva, "Radiative damping in waveguide-based ferromagnetic resonance measured via analysis of perpendicular standing spin waves in sputtered permalloy films," *Phys. Rev. B,*

vol. 92, no. 18, p. 184417, 2015.

[139] S. Mizukami, S. Iihama, N. Inami, T. Hiratsuka, G. Kim, H. Naganuma, M. Oogane, and Y. Ando, "Fast magnetization precession observed in L10-FePt epitaxial thin film," *Appl. Phys. Lett.,* vol. 98, no. 5, p. 052501, 2011.

[140] H. Hertz, "Ueber einen Einfluss des ultravioletten Lichtes auf die electrische Entladung," *Ann. Phys. (Berl.),* vol. 267, no. 8, pp. 983-1000, 1887.

[141] A. Einstein, "Einstein, A., 1905, Ann. Phys.(Leipzig) 31, 132," *Ann. Phys.(Leipzig),* vol. 31, p. 132, 1905.

[142] A. Damascelli, Z. Hussain, and Z.-X. Shen, "Angle-resolved photoemission studies of the cuprate superconductors," *Rev. Mod. Phys.,* vol. 75, no. 2, p. 473, 2003.

[143] W. Zhang, *Photoemission Spectroscopy on High Temperature Superconductor: A Study of Bi2Sr2CaCu2O8 by Laser-Based Angle-Resolved Photoemission*. Springer Science & Business Media, 2012.

[144] Y. Yan, "Interface Magnetic Properties in Ferromagnetic Metal/Semiconductor and Related Heterostructures," University of York, 2018.

[145] K. Matsuzaki, H. Hosono, and T. Susaki, "Magnetotransport Properties across Verwey Transition in Fe3O4(111) Epitaxial Thin Films," *Appl. Phys. Express,* vol. 6, no. 7, p. 073009, 2013.

[146] K. Matsuzaki, V. K. Lazarov, L. Lari, H. Hosono, and T. Susaki, "Fe3O4(1 1 1) thin films with bulk-like properties: growth and atomic characterization," *J. Phys. D: Appl. Phys.,* vol. 46, no. 2, p. 022001, 2013.

[147] (02/02/2018). *Pulsed Laser Deposition (PLD)*. Available: http://groups.ist.utl.pt/rschwarz/rschwarzgroup_files/PLD_files/PLD.htm

[148] L. Chen, S. Mankovsky, S. Wimmer, M. A. W. Schoen, H. S. Korner, M. Kronseder, D. Schuh, D. Bougeard, H. Ebert, D. Weiss, and C. H. Back, "Emergence of anisotropic Gilbert damping in ultrathin Fe layers on GaAs(001)," *Nat. Phys.,* vol. 14, no. 5, p. 490, 2018.

[149] S. Datta and B. Das, "Electronic analog of the electro-optic modulator," *Appl. Phys. Lett.,* vol. 56, no. 7, pp. 665-667, 1990.

[150] Y. B. Xu, D. J. Freeland, E. T. M. Kernohan, W. Y. Lee, M. Tselepi, C. M. Guertler, C. A. F. Vaz, J. A. C. Bland, S. N. Holmes, N. K. Patel, and D. A. Ritchie, "Ferromagnetic metal/semiconductor hybrid structures for magnetoelectronics," *J. Appl. Phys.,* vol. 85, no. 8, pp. 5369-5371, 1999.

[151] S. A. Wolf, D. D. Awschalom, R. A. Buhrman, J. M. Daughton, S. von Molnar, M. L. Roukes, A. Y. Chtchelkanova, and D. M. Treger, "Spintronics: a spin-based electronics vision for the future," *Science,* vol. 294, no. 5546, pp. 1488-95, 2001.

[152] M. Marangolo, F. Gustavsson, M. Eddrief, P. Sainctavit, V. H. Etgens, V. Cros, F. Petroff, J. M. George, P. Bencok, and N. B. Brookes, "Magnetism of the Fe/ZnSe(001) interface," *Phys. Rev. Lett.,* vol. 88, no. 21, p. 217202, 2002.

[153] B. T. Jonker, "Progress toward electrical injection of spin-polarized electrons into semiconductors," *Proceedings of the IEEE,* vol. 91, no. 5, pp. 727-740, 2003.

[154] D. J. Keavney, D. Wu, J. W. Freeland, E. Johnston-Halperin, D. D. Awschalom, and J. Shi, "Element resolved spin configuration in ferromagnetic manganese-doped gallium arsenide," *Phys. Rev. Lett.,* vol. 91, no. 18, p. 187203, 2003.

[155] M. Zolfl, M. Brockmann, M. Kohler, S. Kreuzer, T. Schweinbock, S. Miethaner, F. Bensch, and G. Bayreuther, "Magnetic films epitaxially grown on semiconductors," *J. Magn. Magn. Mater.,* vol. 175, no. 1-2, pp. 16-22, Nov 1997.

[156] F. Bensch, G. Garreau, R. Moosbühler, G. Bayreuther, and E. Beaurepaire, "Onset of ferromagnetism in Fe epitaxially grown on GaAs(001) (4×2) and (2×6)," *J. Appl. Phys.,* vol. 89, no. 11, pp. 7133-7135, 2001.

[157] Y. Yan, C. Lu, H. Tu, X. Lu, W. Liu, J. Wang, L. Ye, I. Will, B. Kuerbanjiang, V. K. Lazarov, J. Wu, J. Wong, B. You, J. Du, R. Zhang, and Y. Xu, "Element specific spin and orbital moments of nanoscale CoFeB amorphous thin films on GaAs(100)," *AIP Advances,* vol. 6, no. 9, 2016.

[158] J. W. Freeland, I. Coulthard, W. J. Antel, and A. P. J. Stampfl, "Interface bonding for Fe thin films on GaAs surfaces of differing morphology," *Phys. Rev. B,* vol. 63, no. 19, p. 193301, 2001.

[159] E. M. Kneedler, B. T. Jonker, P. M. Thibado, R. J. Wagner, B. V. Shanabrook, and L. J. Whitman, "Influence of substrate surface reconstruction on the growth and magnetic properties of Fe on GaAs(001)," *Phys. Rev. B,* vol. 56, no. 13, pp. 8163-8168, 1997.

[160] J. J. Krebs, B. T. Jonker, and G. A. Prinz, "Properties of Fe single-crystal films grown on (100)GaAs by molecular-beam epitaxy," *J. Appl. Phys.,* vol. 61, no. 7, p. 2596, 1987.

[161] J. Florczak and E. Dahlberg, "Magnetization reversal in (100) Fe thin films," *Phys. Rev. B,* vol. 44, no. 17, pp. 9338-9347, 1991.

[162] M. Gester, C. Daboo, R. J. Hicken, S. J. Gray, A. Ercole, and J. A. C. Bland, "Continuous evolution of the in-plane magnetic anisotropies with thickness in epitaxial Fe films," *J. Appl. Phys.,* vol. 80, no. 1, pp. 347-355, 1996.

[163] O. Thomas, Q. Shen, P. Schieffer, N. Tournerie, and B. Lepine, "Interplay between anisotropic strain relaxation and uniaxial interface magnetic anisotropy in epitaxial Fe films on (001) GaAs," *Phys. Rev. Lett.,* vol. 90, no. 1, p. 017205, 2003.

[164] R. Moosbühler, F. Bensch, M. Dumm, and G. Bayreuther, "Epitaxial Fe films on GaAs(001): Does the substrate surface reconstruction affect the uniaxial magnetic anisotropy?," *J. Appl. Phys.,* vol. 91, no. 10, p. 8757, 2002.

[165] V. L. Safonov, "Tensor form of magnetization damping," *J. Appl. Phys.,* vol. 91, no. 10, p. 8653, 2002.

[166] D. Steiauf and M. Fähnle, "Damping of spin dynamics in nanostructures: Anab initiostudy," *Phys. Rev. B,* vol. 72, no. 6, p. 064450, 2005.

[167] J. Seib, D. Steiauf, and M. Fähnle, "Linewidth of ferromagnetic resonance for systems with anisotropic damping," *Phys. Rev. B,* vol. 79, no. 9, p. 092418, 2009.

[168] K. Gilmore, M. D. Stiles, J. Seib, D. Steiauf, and M. Fähnle, "Anisotropic damping of the magnetization dynamics in Ni, Co, and Fe," *Phys. Rev. B,* vol. 81, no. 17, p. 174414, 2010.

[169] R. Meckenstock, D. Spoddig, Z. Frait, V. Kambersky, and J. Pelzl, "Anisotropic Gilbert damping in epitaxial Fe films on InAs(001)," *J. Magn. Magn. Mater.,*

vol. 272-276, pp. 1203-1204, 2004.

[170] Y. Zhai, C. Ni, Y. Xu, Y. B. Xu, J. Wu, H. X. Lu, and H. R. Zhai, "A study on ferromagnetic resonance linewidth of single crystalline ultrathin Fe film grown on GaAs substrate," *J. Appl. Phys.,* vol. 101, no. 9, 2007.

[171] R. Yilgin, Y. Sakuraba, M. Oogane, S. Mizukami, Y. Ando, and T. Miyazaki, "Anisotropic Intrinsic Damping Constant of Epitaxial Co2MnSi Heusler Alloy Films," *Jpn. J. Appl. Phys.,* vol. 46, no. No. 9, pp. L205-L208, 2007.

[172] L. Chen, M. Decker, M. Kronseder, R. Islinger, M. Gmitra, D. Schuh, D. Bougeard, J. Fabian, D. Weiss, and C. H. Back, "Robust spin-orbit torque and spin-galvanic effect at the Fe/GaAs (001) interface at room temperature," *Nat. Commun.,* vol. 7, p. 13802, 2016.

[173] D. Fang, H. Kurebayashi, J. Wunderlich, K. Vyborny, L. P. Zarbo, R. P. Campion, A. Casiraghi, B. L. Gallagher, T. Jungwirth, and A. J. Ferguson, "Spin-orbit-driven ferromagnetic resonance," *Nat. Nanotechnol.,* vol. 6, no. 7, pp. 413-7, 2011.

[174] Y. X. Lu, J. S. Claydon, Y. B. Xu, S. M. Thompson, K. Wilson, and G. van der Laan, "Epitaxial growth and magnetic properties of half-metallic Fe3O4 on GaAs(100)," *Phys. Rev. B,* vol. 70, no. 23, p. 233304, 2004.

[175] G. A. Prinz, "Magnetic properties of single-crystal {110} iron films grown on GaAs by molecular beam epitaxy (invited)," *J. Appl. Phys.,* vol. 53, no. 3, p. 2087, 1982.

[176] G. Chen, J. X. Li, J. Zhu, J. H. Liang, and Y. Z. Wu, "In-plane magnetic anisotropy in Fe/MgO/GaAs(001) system," *J. Appl. Phys.,* vol. 109, no. 7, p. 07c108, 2011.

[177] A. Ionescu, M. Tselepi, D. M. Gillingham, G. Wastlbauer, S. J. Steinmüller, H. E. Beere, D. A. Ritchie, and J. A. C. Bland, "Submonolayer growth of Fe on a GaAs(100)−2×6reconstructed surface," *Phys. Rev. B,* vol. 72, no. 12, p. 125404, 2005.

[178] H. Danan, A. Herr, and A. J. P. Meyer, "New Determinations of the Saturation Magnetization of Nickel and Iron," *J. Appl. Phys.,* vol. 39, no. 2, pp. 669-670,

1968.

[179] K. Suzuki, N. Kataoka, A. Inoue, A. Makino, and T. Masumoto, "High Saturation Magnetization and Soft Magnetic-Properties of Bcc Fe-Zr-B Alloys with Ultrafine Grain-Structure," *Mater. Trans.,* vol. 31, no. 8, pp. 743-746, 1990.

[180] C. Carbone and S. F. Alvarado, "Antiparallel coupling between Fe layers separated by a Cr interlayer: Dependence of the magnetization on the film thickness," *Phys. Rev. B,* vol. 36, no. 4, pp. 2433-2435, 1987.

[181] Z. P. Shi, P. M. Levy, and J. L. Fry, "Spin polarization of epitaxial Cr on Fe(001) and interlayer magnetic coupling in Fe/Cr multilayered structures," *Phys. Rev. Lett.,* vol. 69, no. 25, pp. 3678-3681, 1992.

[182] Y. B. Xu, Q. Y. Jin, Y. Zhai, M. Lu, Y. Z. Miao, Q. S. Bie, and H. R. Zhai, "Complex magneto-optical Kerr rotation of Fe,FeCo/Cu multilayer films," *J. Appl. Phys.,* vol. 74, no. 5, pp. 3470-3474, 1993.

[183] S. Lepadatu, J. Wu, C. Bunce, X. Zou, D. Niu, Y. B. Xu, R. Chantrell, and G. P. Ju, "Ultrafast optically induced spin dynamics in patterned single crystal Fe dot arrays," *J. Appl. Phys.,* vol. 101, no. 9, 2007.

[184] Y. B. Xu, M. Tselepi, C. M. Guertler, C. A. F. Vaz, G. Wastlbauer, J. A. C. Bland, E. Dudzik, and G. van der Laan, "Giant enhancement of orbital moments and perpendicular anisotropy in epitaxial Fe/GaAs(100)," *J. Appl. Phys.,* vol. 89, no. 11, pp. 7156-7158, 2001.

[185] S. Mizukami, D. Watanabe, T. Kubota, X. Zhang, H. Naganuma, M. Oogane, Y. Ando, and T. Miyazaki, "Laser-Induced Fast Magnetization Precession and Gilbert Damping for CoCrPt Alloy Thin Films with Perpendicular Magnetic Anisotropy," *Appl. Phys. Express,* vol. 3, no. 12, p. 123001, 2010.

[186] S. Mizukami, Y. Ando, and T. Miyazaki, "Effect of spin diffusion on Gilbert damping for a very thin permalloy layer in Cu/permalloy/Cu/Pt films," *Phys. Rev. B,* vol. 66, no. 10, p. 104413, 2002.

[187] M. Tokac, S. A. Bunyaev, G. N. Kakazei, D. S. Schmool, D. Atkinson, and A. T. Hindmarch, "Interfacial Structure Dependent Spin Mixing Conductance in Cobalt Thin Films," *Phys. Rev. Lett.,* vol. 115, no. 5, p. 056601, 2015.

[188] Y. Sun, H. Chang, M. Kabatek, Y. Y. Song, Z. Wang, M. Jantz, W. Schneider, M. Wu, E. Montoya, B. Kardasz, B. Heinrich, S. G. te Velthuis, H. Schultheiss, and A. Hoffmann, "Damping in yttrium iron garnet nanoscale films capped by platinum," *Phys. Rev. Lett.,* vol. 111, no. 10, p. 106601, 2013.

[189] C. T. Chen, Y. U. Idzerda, H. Lin, N. V. Smith, G. Meigs, E. Chaban, G. H. Ho, E. Pellegrin, and F. Sette, "Experimental confirmation of the X-ray magnetic circular dichroism sum rules for iron and cobalt," *Phys. Rev. Lett.,* vol. 75, no. 1, pp. 152-155, 1995.

[190] C. T. Chen, Y. U. Idzerda, H. J. Lin, G. Meigs, A. Chaiken, G. A. Prinz, and G. H. Ho, "Element-specific magnetic hysteresis as a means for studying heteromagnetic multilayers," *Phys. Rev. B,* vol. 48, no. 1, pp. 642-645, 1993.

[191] J. S. Claydon, Y. B. Xu, M. Tselepi, J. A. Bland, and G. van der Laan, "Direct observation of a bulklike spin moment at the Fe/GaAs(100)-4x6 interface," *Phys. Rev. Lett.,* vol. 93, no. 3, p. 037206, 2004.

[192] S. Mangin, D. Ravelosona, J. A. Katine, M. J. Carey, B. D. Terris, and E. E. Fullerton, "Current-induced magnetization reversal in nanopillars with perpendicular anisotropy," *Nat. Mater.,* vol. 5, no. 3, pp. 210-215, 2006.

[193] M. C. Hickey and J. S. Moodera, "Origin of intrinsic Gilbert damping," *Phys. Rev. Lett.,* vol. 102, no. 13, p. 137601, 2009.

[194] G. P. Zhang, T. Jenkins, M. Bennett, and Y. H. Bai, "Manifestation of intra-atomic 5d6s-4f exchange coupling in photoexcited gadolinium," *J. Phys.: Condens. Matter,* vol. 29, no. 49, p. 495807, 2017.

[195] H. Lee, Y. H. A. Wang, C. K. A. Mewes, W. H. Butler, T. Mewes, S. Maat, B. York, M. J. Carey, and J. R. Childress, "Magnetization relaxation and structure of CoFeGe alloys," *Appl. Phys. Lett.,* vol. 95, no. 8, 2009.

[196] C. Liu, C. K. A. Mewes, M. Chshiev, T. Mewes, and W. H. Butler, "Origin of low Gilbert damping in half metals," *Appl. Phys. Lett.,* vol. 95, no. 2, p. 022509, 2009.

[197] R. A. de Groot, F. M. Mueller, P. G. v. Engen, and K. H. J. Buschow, "New Class of Materials: Half-Metallic Ferromagnets," *Phys. Rev. Lett.,* vol. 50, no. 25, pp.

2024-2027, 1983.

[198] I. Galanakis, P. H. Dederichs, and N. Papanikolaou, "Slater-Pauling behavior and origin of the half-metallicity of the full-Heusler alloys," *Phys. Rev. B,* vol. 66, no. 17, 2002.

[199] S. Ishida, S. Fujii, S. Kashiwagi, and S. Asano, "Search for Half-Metallic Compounds in Co2MnZ (Z=IIIb, IVb, Vb Element)," *J. Phys. Soc. Jpn.,* vol. 64, no. 6, pp. 2152-2157, 1995/06/15 1995.

[200] S. Fujii, S. Sugimura, Ishida, and S. Asano, "Hyperfine fields and electronic structures of the Heusler alloys Co2MnX (X=Al, Ga, Si, Ge, Sn)," *J. Phys.: Condens. Matter,* vol. 2, no. 43, pp. 8583-8589, 1990.

[201] J. Kübler, A. R. William, and C. B. Sommers, "Formation and coupling of magnetic moments in Heusler alloys," *Phys. Rev. B,* vol. 28, no. 4, pp. 1745-1755, 1983.

[202] T. Ambrose, J. J. Krebs, and G. A. Prinz, "Magnetic properties of single crystal Co2MnGe Heusler alloy films," *J. Appl. Phys.,* vol. 87, no. 9, pp. 5463-5465, 2000.

[203] M. P. Raphael, B. Ravel, M. A. Willard, S. F. Cheng, B. N. Das, R. M. Stroud, K. M. Bussmann, J. H. Claassen, and V. G. Harris, "Magnetic, structural, and transport properties of thin film and single crystal Co2MnSi," *Appl. Phys. Lett.,* vol. 79, no. 26, pp. 4396-4398, 2001.

[204] B. Ravel, M. P. Raphael, V. G. Harris, and Q. Huang, "EXAFS and neutron diffraction study of the Heusler alloyCo2MnSi," *Phys. Rev. B,* vol. 65, no. 18, p. 184431, 2002.

[205] U. Geiersbach, A. Bergmann, and K. Westerholt, "Structural, magnetic and magnetotransport properties of thin films of the Heusler alloys Cu2MnAl, Co2MnSi, Co2MnGe and Co2MnSn," *J. Magn. Magn. Mater.,* vol. 240, no. 1-3, pp. 546-549, 2002.

[206] R. Yilgin, M. Oogane, S. Yakata, Y. Ando, and T. Miyazaki, "Intrinsic Gilbert damping constant in Co/sub 2/MnAl Heusler alloy films," *IEEE Trans. Magn.,* vol. 41, no. 10, pp. 2799-2801, 2005.

[207] Y. Liu, L. R. Shelford, V. V. Kruglyak, R. J. Hicken, Y. Sakuraba, M. Oogane, Y. Ando, and T. Miyazaki, "Ultrafast optical modification of magnetic anisotropy and stimulated precession in an epitaxial Co2MnAl thin film," *J. Appl. Phys.,* vol. 101, no. 9, p. 09c106, 2007.

[208] R. Yilgin, M. Oogane, Y. Ando, and T. Miyazaki, "Gilbert damping constant in polycrystalline CO2MnSi Heusler alloy films," *J. Magn. Magn. Mater.,* vol. 310, no. 2, pp. 2322-2323, 2007.

[209] Y. Liu, L. R. Shelford, V. V. Kruglyak, R. J. Hicken, Y. Sakuraba, M. Oogane, and Y. Ando, "Optically induced magnetization dynamics and variation of damping parameter in epitaxial Co2MnS iHeusler alloy films," *Phys. Rev. B,* vol. 81, no. 9, p. 094402, 2010.

[210] M. Oogane, T. Kubota, Y. Kota, S. Mizukami, H. Naganuma, A. Sakuma, and Y. Ando, "Gilbert magnetic damping constant of epitaxially grown Co-based Heusler alloy thin films," *Appl. Phys. Lett.,* vol. 96, no. 25, p. 252501, 2010.

[211] T. Kubota, S. Tsunegi, M. Oogane, S. Mizukami, T. Miyazaki, H. Naganuma, and Y. Ando, "Half-metallicity and Gilbert damping constant in Co[sub 2]Fe[sub x]Mn[sub 1−x]Si Heusler alloys depending on the film composition," *Appl. Phys. Lett.,* vol. 94, no. 12, p. 122504, 2009.

[212] W. He, T. Zhu, X. Q. Zhang, H. T. Yang, and Z. H. Cheng, "Ultrafast demagnetization enhancement in CoFeB/MgO/CoFeB magnetic tunneling junction driven by spin tunneling current," *Sci. Rep.,* vol. 3, p. 2883, 2013.

[213] B. S. D. C. S. Varaprasad, A. Srinivasan, Y. K. Takahashi, M. Hayashi, A. Rajanikanth, and K. Hono, "Spin polarization and Gilbert damping of Co2Fe(GaxGe1−x) Heusler alloys," *Acta Mater.,* vol. 60, no. 18, pp. 6257-6265, 2012.

[214] M. Belmeguenai, H. Tuzcuoglu, M. S. Gabor, T. Petrisor, C. Tiusan, D. Berling, F. Zighem, T. Chauveau, S. M. Chérif, and P. Moch, "Co2FeAl thin films grown on MgO substrates: Correlation between static, dynamic, and structural properties," *Phys. Rev. B,* vol. 87, no. 18, p. 184431, 2013.

[215] M. Belmeguenai, H. Tuzcuoglu, M. S. Gabor, T. Petrisor, C. Tiusan, F. Zighem,

S. M. Chérif, and P. Moch, "Co2FeAl Heusler thin films grown on Si and MgO substrates: Annealing temperature effect," *J. Appl. Phys.,* vol. 115, no. 4, p. 043918, 2014.

[216] Y. Cui, J. Lu, S. Schäfer, B. Khodadadi, T. Mewes, M. Osofsky, and S. A. Wolf, "Magnetic damping and spin polarization of highly ordered B2 Co2FeAl thin films," *J. Appl. Phys.,* vol. 116, no. 7, p. 073902, 2014.

[217] S. Qiao, S. Nie, J. Zhao, and X. Zhang, "The thickness-dependent dynamic magnetic property of Co2FeAl films grown by molecular beam epitaxy," *Appl. Phys. Lett.,* vol. 105, no. 17, p. 172406, 2014.

[218] H. C. Yuan, S. H. Nie, T. P. Ma, Z. Zhang, Z. Zheng, Z. H. Chen, Y. Z. Wu, J. H. Zhao, H. B. Zhao, and L. Y. Chen, "Different temperature scaling of strain-induced magneto-crystalline anisotropy and Gilbert damping in Co2FeAl film epitaxied on GaAs," *Appl. Phys. Lett.,* vol. 105, no. 7, p. 072413, 2014.

[219] S. Husain, S. Akansel, A. Kumar, P. Svedlindh, and S. Chaudhary, "Growth of Co2FeAl Heusler alloy thin films on Si(100) having very small Gilbert damping by Ion beam sputtering," *Sci. Rep.,* vol. 6, p. 28692, 2016.

[220] S. Akansel, A. Kumar, N. Behera, S. Husain, R. Brucas, S. Chaudhary, and P. Svedlindh, "Thickness-dependent enhancement of damping in Co2FeAl/β-Ta thin films," *Phys. Rev. B,* vol. 97, no. 13, p. 134421, 2018.

[221] Z. Chen, W. Kong, K. Mi, G. Chen, P. Zhang, X. Fan, C. Gao, and D. Xue, "The anisotropic effective damping of thickness-dependent epitaxial Co2FeAl films studied by spin rectification," *Appl. Phys. Lett.,* vol. 112, no. 12, 2018.

[222] L. M. Loong, J. H. Kwon, P. Deorani, C. N. Tung Yu, A. Hirohata, and H. Yang, "Investigation of the temperature-dependence of ferromagnetic resonance and spin waves in Co2FeAl0.5Si0.5," *Appl. Phys. Lett.,* vol. 104, no. 23, 2014.

[223] H. B. Yang, S. C. Wang, A. K. Sekharan, H. Matsui, S. Souma, T. Sato, T. Takahashi, T. Takeuchi, J. C. Campuzano, R. Jin, B. C. Sales, D. Mandrus, Z. Wang, and H. Ding, "ARPES on Na0.6CoO2: Fermi surface and unusual band dispersion," *Phys. Rev. Lett.,* vol. 92, no. 24, p. 246403, 2004.

[224] I. Galanakis, P. Mavropoulos, and P. H. Dederichs, "Electronic structure and

Slater–Pauling behaviour in half-metallic Heusler alloys calculated from first principles," *J. Phys. D: Appl. Phys.,* vol. 39, no. 5, pp. 765-775, 2006.

[225] X. Zhang, H. Xu, B. Lai, Q. Lu, X. Lu, Y. Chen, W. Niu, C. Gu, W. Liu, X. Wang, C. Liu, Y. Nie, L. He, and Y. Xu, "Direct observation of high spin polarization in Co2FeAl thin films," *Sci. Rep.,* vol. 8, no. 1, p. 8074, 2018.

[226] S. Qiao, S. Nie, J. Zhao, and X. Zhang, "Temperature dependent magnetic anisotropy of epitaxial Co2FeAl films grown on GaAs," *J. Appl. Phys.,* vol. 117, no. 9, p. 093904, 2015.

[227] M. S. Gabor, T. Petrisor, C. Tiusan, M. Hehn, and T. Petrisor, "Magnetic and structural anisotropies of Co2FeAl Heusler alloy epitaxial thin films," *Phys. Rev. B,* vol. 84, no. 13, p. 134413, 2011.

[228] M. S. Gabor, T. Petrisor, C. Tiusan, and T. Petrisor, "Perpendicular magnetic anisotropy in Ta/Co2FeAl/MgO multilayers," *J. Appl. Phys.,* vol. 114, no. 6, p. 063905, 2013.

[229] H. Schneider, G. Jakob, M. Kallmayer, H. J. Elmers, M. Cinchetti, B. Balke, S. Wurmehl, C. Felser, M. Aeschlimann, and H. Adrian, "Epitaxial film growth and magnetic properties of Co2FeSi," *Phys. Rev. B,* vol. 74, no. 17, p. 174426, 2006.

[230] C. Bunce, J. Wu, Y. X. Lu, Y. B. Xu, and R. W. Chantrell, "Picosecond Magnetization Dynamics of Single-Crystal Fe3O4 Thin Films," *IEEE Trans. Magn.,* vol. 44, no. 11, pp. 2970-2973, Nov 2008.

[231] S. Iihama, A. Sakuma, H. Naganuma, M. Oogane, S. Mizukami, and Y. Ando, "Influence of L10 order parameter on Gilbert damping constants for FePd thin films investigated by means of time-resolved magneto-optical Kerr effect," *Phys. Rev. B,* vol. 94, no. 17, p. 174425, 2016.

[232] L. J. Atkinson, T. A. Ostler, O. Hovorka, K. K. Wang, B. Lu, G. P. Ju, J. Hohlfeld, B. Bergman, B. Koopmans, and R. W. Chantrell, "Effects of interactions on the relaxation processes in magnetic nanostructures," *Phys. Rev. B,* vol. 94, no. 13, p. 134431, 2016.

[233] G. Malinowski, K. C. Kuiper, R. Lavrijsen, H. J. M. Swagten, and B. Koopmans,

"Magnetization dynamics and Gilbert damping in ultrathin Co[sub 48]Fe[sub 32]B[sub 20] films with out-of-plane anisotropy," *Appl. Phys. Lett.,* vol. 94, no. 10, p. 102501, 2009.

[234] B. S. Chun, K.-H. Kim, N. Leibing, S. Serrano-Guisan, H.-W. Schumacher, M. Abid, I. C. Chu, O. N. Mryasov, D. K. Kim, H.-C. Wu, C. Hwang, and Y. K. Kim, "Structural and magnetic properties of epitaxial Co2FeAl films grown on MgO substrates for different growth temperatures," *Acta Mater.,* vol. 60, no. 19, pp. 6714-6719, 2012.

[235] G. Ortiz, M. S. Gabor, J. T. Petrisor, F. Boust, F. Issac, C. Tiusan, M. Hehn, and J. F. Bobo, "Static and dynamic magnetic properties of epitaxial Co2FeAl Heusler alloy thin films," *J. Appl. Phys.,* vol. 109, no. 7, p. 07d324, 2011.

[236] W. Wang, M. Przybylski, W. Kuch, L. Chelaru, J. Wang, Y. Lu, J. Barthel, H. Meyerheim, and J. Kirschner, "Magnetic properties and spin polarization of Co2MnSi Heusler alloy thin films epitaxially grown on GaAs(001)," *Phys. Rev. B,* vol. 71, no. 14, p. 144416, 2005.

[237] S. Wurmehl, G. H. Fecher, K. Kroth, F. Kronast, H. A. Dürr, Y. Takeda, Y. Saitoh, K. Kobayashi, H.-J. Lin, G. Schönhense, and C. Felser, "Electronic structure and spectroscopy of the quaternary Heusler alloy Co2Cr1−xFexAl," *J. Phys. D: Appl. Phys.,* vol. 39, no. 5, pp. 803-815, 2006.

[238] A. P. Marscher, S. G. Jorstad, J. L. Gomez, M. F. Aller, H. Terasranta, M. L. Lister, and A. M. Stirling, "Observational evidence for the accretion-disk origin for a radio jet in an active galaxy," *Nature,* vol. 417, no. 6889, pp. 625-7, 2002.

[239] S. Andrieu, A. Neggache, T. Hauet, T. Devolder, A. Hallal, M. Chshiev, A. M. Bataille, P. Le Fèvre, and F. Bertran, "Direct evidence for minority spin gap in the Co2MnSiHeusler compound," *Phys. Rev. B,* vol. 93, no. 9, 2016.

[240] I. Razdolski, A. Alekhin, N. Ilin, J. P. Meyburg, V. Roddatis, D. Diesing, U. Bovensiepen, and A. Melnikov, "Nanoscale interface confinement of ultrafast spin transfer torque driving non-uniform spin dynamics," *Nat. Commun.,* vol. 8, p. 15007, 2017.

[241] M. Jäckl, V. I. Belotelov, I. A. Akimov, I. V. Savochkin, D. R. Yakovlev, A. K.

Zvezdin, and M. Bayer, "Magnon Accumulation by Clocked Laser Excitation as Source of Long-Range Spin Waves in Transparent Magnetic Films," *Phys. Rev. X,* vol. 7, no. 2, p. 021009, 2017.

[242] B. Lenk, G. Eilers, J. Hamrle, and M. Munzenberg, "Spin-wave population in nickel after femtosecond laser pulse excitation," *Phys. Rev. B,* vol. 82, no. 13, p. 134443, 2010.

[243] Y. Hashimoto, S. Kobayashi, and H. Munekata, "Photoinduced precession of magnetization in ferromagnetic (Ga,Mn)As," *Phys. Rev. Lett.,* vol. 100, no. 6, p. 067202, 2008.

[244] J. Wang, X. Zhang, X. Lu, J. Zhang, Y. Yan, H. Ling, J. Wu, Y. Zhou, and Y. Xu, "Magnetic domain wall engineering in a nanoscale permalloy junction," *Appl. Phys. Lett.,* vol. 111, no. 7, p. 072401, 2017.

[245] A. Azevedo, A. B. Oliveira, F. M. de Aguiar, and S. M. Rezende, "Extrinsic contributions to spin-wave damping and renormalization in thin Ni50Fe50 films," *Phys. Rev. B,* vol. 62, no. 9, pp. 5331-5333, 2000.

[246] S. Serrano-Guisan, H.-C. Wu, C. Boothman, M. Abid, B. S. Chun, I. V. Shvets, and H. W. Schumacher, "Thickness dependence of the effective damping in epitaxial Fe3O4/MgO thin films," *J. Appl. Phys.,* vol. 109, no. 1, p. 013907, 2011.

[247] C. M. Fang, G. A. de Wijs, and R. A. de Groot, "Spin-polarization in half-metals (invited)," *J. Appl. Phys,* vol. 91, no. 10, p. 8340, 2002.

[248] I. Leonov, A. N. Yaresko, V. N. Antonov, and V. I. Anisimov, "Electronic structure of charge-ordered Fe3O4 from calculated optical, magneto-optical Kerr effect, and O K-edge x-ray absorption spectra," *Phys. Rev. B,* vol. 74, no. 16, p. 165117, 2006.

[249] Z. Zhang and S. Satpathy, "Electron states, magnetism, and the Verwey transition in magnetite," *Phys. Rev. B,* vol. 44, no. 24, pp. 13319-13331, 1991.

[250] Y. S. Dedkov, U. Rüdiger, and G. Güntherodt, "Evidence for the half-metallic ferromagnetic state of Fe3O4 by spin-resolved photoelectron spectroscopy," *Phys. Rev. B,* vol. 65, no. 6, p. 064417, 2002.

[251] S. C. Weng, Y. R. Lee, C. G. Chen, C. H. Chu, Y. L. Soo, and S. L. Chang, "Direct observation of charge ordering in magnetite using resonant multiwave x-ray diffraction," *Phys. Rev. Lett.,* vol. 108, no. 14, p. 146404, 2012.

[252] M. Imada, A. Fujimori, and Y. Tokura, "Metal-insulator transitions," *Rev. Mod. Phys.,* vol. 70, no. 4, pp. 1039-1263, 1998.

[253] Z. Popović and S. Satpathy, "Origin of Charge-Orbital Order in the Half-Doped Manganites," *Phys. Rev. Lett.,* vol. 88, no. 19, p. 197201, 2002.

[254] G. Subias, J. Garcia, J. Blasco, M. Grazia Proietti, H. Renevier, and M. Concepcion Sanchez, "Magnetite, a model system for mixed-valence oxides, does not show charge ordering," *Phys. Rev. Lett.,* vol. 93, no. 15, p. 156408, 2004.

[255] E. Liu, Z. Huang, J.-G. Zheng, J. Yue, L. Chen, X. Wu, Y. Sui, Y. Zhai, S. Tang, J. Du, and H. Zhai, "Texture induced magnetic anisotropy in Fe3O4 films," *Appl. Phys. Lett.,* vol. 107, no. 17, p. 172403, 2015.

[256] D. T. Margulies, F. T. Parker, M. L. Rudee, F. E. Spada, J. N. Chapman, P. R. Aitchison, and A. E. Berkowitz, "Origin of the anomalous magnetic behaviour in single crystal Fe3O4 films," *Phys. Rev. Lett.,* vol. 79, no. 25, pp. 5162-5165, 1997.

[257] D. Gilks, L. Lari, J. Naughton, O. Cespedes, Z. Cai, A. Gerber, S. M. Thompson, K. Ziemer, and V. K. Lazarov, "Origin of anomalous magnetite properties in crystallographic matched heterostructures: Fe3O4(111)/MgAl2O4(111)," *J. Phys.: Condens. Matter,* vol. 25, no. 48, p. 485004, 2013.

[258] K. P. McKenna, F. Hofer, D. Gilks, V. K. Lazarov, C. Chen, Z. Wang, and Y. Ikuhara, "Atomic-scale structure and properties of highly stable antiphase boundary defects in Fe3O4," *Nat. Commun.,* vol. 5, p. 5740, 2014.

[259] D. Gilks, Z. Nedelkoski, L. Lari, B. Kuerbanjiang, K. Matsuzaki, T. Susaki, D. Kepaptsoglou, Q. Ramasse, R. Evans, K. McKenna, and V. K. Lazarov, "Atomic and electronic structure of twin growth defects in magnetite," *Sci. Rep.,* vol. 6, p. 20943, 2016.

[260] D. Gilks, L. Lari, K. Matsuzaki, H. Hosono, T. Susaki, and V. K. Lazarov,

"Structural study of Fe3O4(111) thin films with bulk like magnetic and magnetotransport behaviour," *J. Appl. Phys.,* vol. 115, no. 17, p. 17C107, 2014.

[261] L. Lari, S. Lea, C. Feeser, B. W. Wessels, and V. K. Lazarov, "Ferromagnetic InMnSb multi-phase films study by aberration-corrected (scanning) transmission electron microscopy," *J. Appl. Phys.,* vol. 111, no. 7, p. 07C311, 2012.

[262] N. Guskos, E. A. Anagnostakis, V. Likodimos, T. Bodziony, J. Typek, M. Maryniak, U. Narkiewicz, I. Kucharewicz, and S. Waplak, "Ferromagnetic resonance and ac conductivity of a polymer composite of Fe3O4 and Fe3C nanoparticles dispersed in a graphite matrix," *J. Appl. Phys.,* vol. 97, no. 2, p. 024304, 2005.

[263] L. R. Bickford, "Ferromagnetic Resonance Absorption in Magnetite Single Crystals," *Phys. Rev.,* vol. 78, no. 4, pp. 449-457, 1950.

[264] H. Shul, "Ferromagnetic resonance in nickel ferrite between one and two kilomegacycle," *Phys. Rev.,* vol. 97, pp. 555-557, 1955.

[265] L. A. Kalev and L. Niesen, "Nuclear resonance scattering study on the spin orientation in an epitaxial layer of Fe3O4 on MgO(100)," *Phys. Rev. B,* vol. 67, no. 22, p. 224403, 2003.

[266] J. K. Miller, J. Qi, Y. Xu, Y. J. Cho, X. Liu, J. K. Furdyna, I. Perakis, T. V. Shahbazyan, and N. Tolk, "Near-bandgap wavelength dependence of long-lived traveling coherent longitudinal acoustic phonons in GaSb-GaAs heterostructures," *Phys. Rev. B,* vol. 74, no. 11, p. 113313, 2006.

[267] V. V. Anisimov, I. S. Elfimov, N. Hamada, and K. Terakura, "Charge-ordered insulating state of Fe3O4 from first-principles electronic structure calculations," *Phys. Rev. B,* vol. 54, no. 7, pp. 4387-4390, 1996.

[268] I. Chistyi, I. Fabelinskii, V. Kitaeva, V. Osiko, Y. Pisarevskii, I. Sil'Vestrova, and N. Sobolev, "Experimental study of the properties of ZrO2- Y2O3 and HfO2-Y2O3 solid solutions," *J. Raman Spectrosc.,* vol. 6, no. 4, pp. 183-192, 1977.

[269] H. J. Reichmann and S. D. Jacobsen, "High-pressure elasticity of a natural magnetite crystal," *Am. Mineral.,* vol. 89, no. 7, pp. 1061-1066, 2004.

[270] R. F. L. Evans, D. Hinzke, U. Atxitia, U. Nowak, R. W. Chantrell, and O. Chubykalo-Fesenko, "Stochastic form of the Landau-Lifshitz-Bloch equation," *Phys. Rev. B,* vol. 85, no. 1, p. 014433, 2012.

[271] O. Chubykalo-Fesenko, U. Nowak, R. W. Chantrell, and D. Garanin, "Dynamic approach for micromagnetics close to the Curie temperature," *Phys. Rev. B,* vol. 74, no. 9, p. 094436, 2006.

[272] R. Yanes, O. Chubykalo-Fesenko, H. Kachkachi, D. A. Garanin, R. Evans, and R. W. Chantrell, "Effective anisotropies and energy barriers of magnetic nanoparticles with Néel surface anisotropy," *Phys. Rev. B,* vol. 76, no. 6, p. 064416, 2007.

[273] D. Garanin and O. Chubykalo-Fesenko, "Thermal fluctuations and longitudinal relaxation of single-domain magnetic particles at elevated temperatures," *Phys. Rev. B,* vol. 70, no. 21, p. 212409, 2004.

[274] M. Djordjevic, G. Eilers, A. Parge, M. Munzenberg, and J. S. Moodera, "Intrinsic and nonlocal Gilbert damping parameter in all optical pump-probe experiments," *J. Appl. Phys.,* vol. 99, no. 8, p. 08F308, 2006.